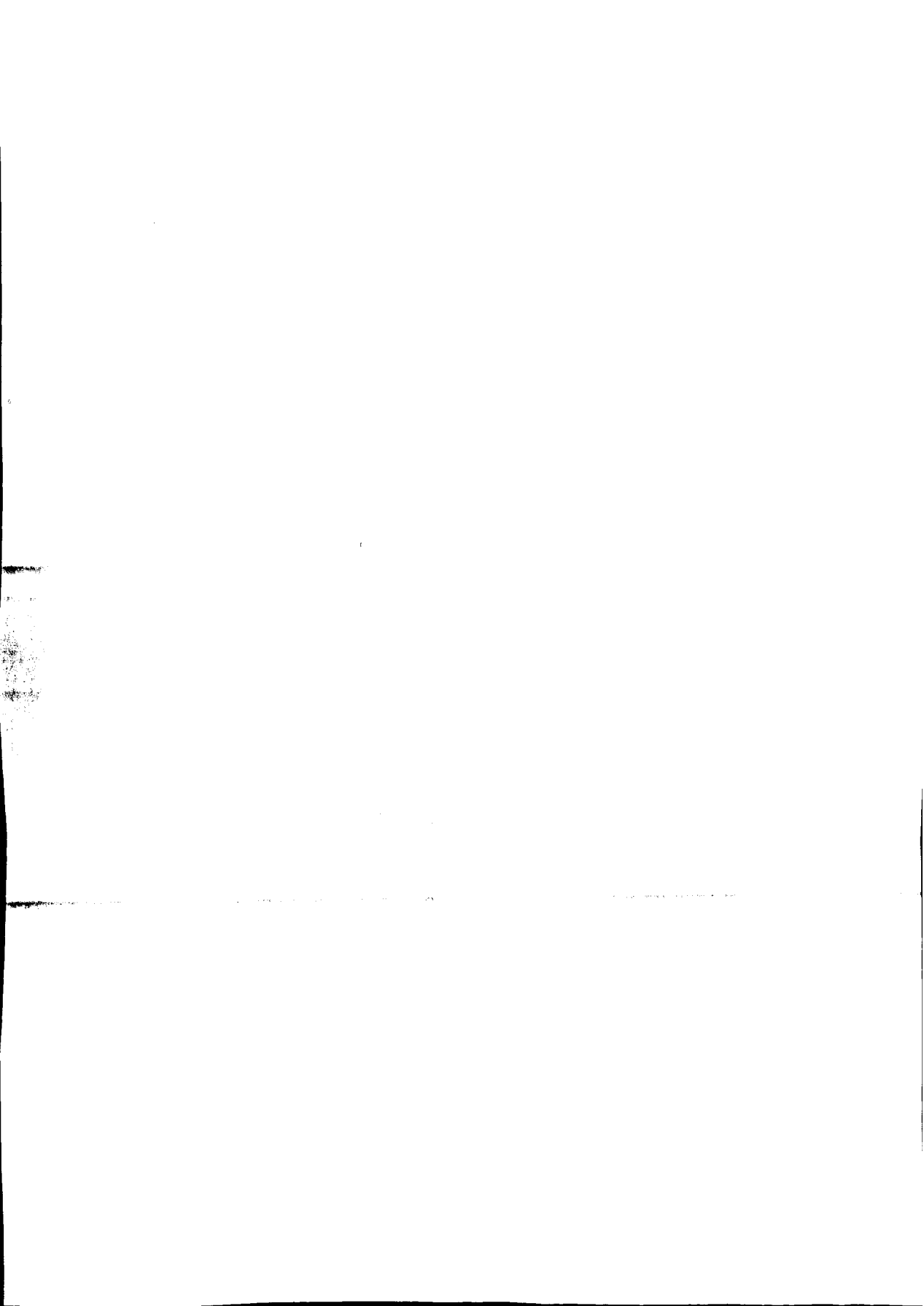


**Numerical modelling of estuarine
flow over steep topography**

Marco Bijvelds



STELLINGEN

behorende bij het proefschrift

Numerical modelling of estuarine flow over steep topography

van

Marco Bijvelds

Delft, 12 maart 2001

1. De voordelen van het gebruik van een *boundary fitted* σ -coördinatenrooster ten opzichte van een Cartesisch z -coördinatenrooster zijn slechts evident in geval van zuivere grenslaagstroming. In het algemeen geldt dat dat model de voorkeur verdient waarvan de oriëntatie van de roosterlijnen van het verticale rekenrooster zoveel mogelijk samenvallen met de optredende stromingsrichting en dichtheidsgradiënten.

Dit proefschrift.

2. Bij de simulatie van gestratificeerde stroming in gebieden met een sterk variërende bodemligging bepaalt de numerieke benadering van de advectietermen de kwaliteit van de verkregen oplossing in belangrijke mate.

Dit proefschrift.

3. Het standaard k - ε turbulentiemodel is niet geschikt voor het modelleren van quasi-tweedimensionale ondiepwaterturbulentie.

Dit proefschrift.

4. De horizontale impulsoverdracht in ondiepwatremenglagen door horizontale Reynoldsschuifspanningen kan met het behulp van het tweelengteschalenturbulentiemodel, zoals beschreven in dit proefschrift, goed worden voorspeld.

Dit proefschrift.

5. De uitspraak van Slørdal dat de methode van Stelling & Van Kester voor de berekening van de horizontale barocliene drukgradiënt tot een systematische onderschatting van deze drukgradiënt leidt, is slechts relevant voor academische testgevallen en is van ondergeschikt belang voor praktijktoepassingen.

Slørdal, L.H., 1997. The pressure gradient force in sigma-co-ordinate ocean models. *Int. J. for Num. Meth. in Fluids*, 24, 987-1017

6. Lokale afwijkingen van de hydrostatische druk kunnen aanzienlijke gevolgen hebben voor het globale stromingspatroon in ondiepwatermodellen.
7. Bij het onderzoek naar de positieve invloed van de consumptie van wijn op de reductie van hart- en vaatziekten dient de stressverlagende werking van alcohol te worden verdisconteerd.
8. Het algemeen beleid van Grote Technologische Instituten moet niet gestoeld zijn op het marktmechanisme dat iedere vraag een aanbod creëert, maar dient te worden gebaseerd op het ontwikkelingsmarketingprincipe waarbij het aanbod in een latente behoefte voorziet.
9. De aan een model ten grondslag liggende numerieke methoden zijn vaker gebaseerd op historische gronden dan op huidige inzichten.
10. Bij het ontwikkelen van programmatuur onder het Windows besturingssysteem wordt de uitdrukking *uitstel van executie* een heel nieuw leven ingeblazen.
11. Het schrijven van een dissertatie op jonge leeftijd moet eerder als een jeugdzonde dan als een levenswerk worden beschouwd.

3667

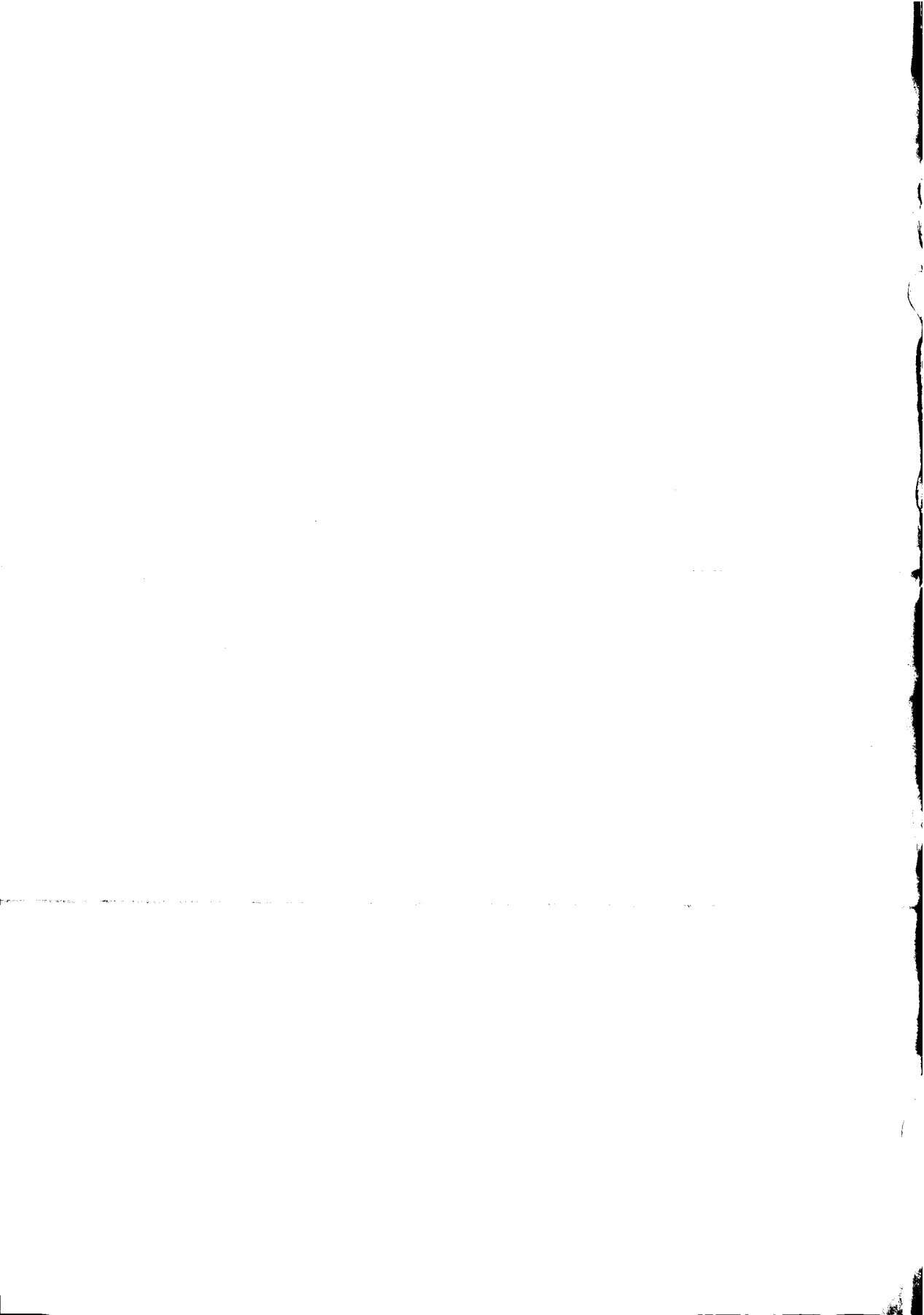
752504

3006285

TR 3661

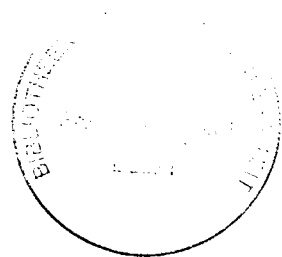
Numerical modelling of estuarine flow over steep topography

Numerieke modellering van estuariene stroming over steile topografie



Numerical modelling of estuarine flow
over steep topography

Proefschrift



ter verkrijging van de graad van doctor
aan de Technische Universiteit Delft,
op gezag van de Rector Magnificus prof. ir K.F. Wakker,
voorzitter van het College voor Promoties,
in het openbaar te verdedigen op maandag 12 maart 2001 om 13.30 uur
door Marco Diederik Jodocus Petrus BIJVELDS
civiel ingenieur
geboren te Eindhoven.

Dit proefschrift is goedgekeurd door de promotor:

Prof. dr ir G.S. Stelling

Samenstelling promotiecommissie:

Rector Magnificus,	voorzitter
Prof. dr ir G.S. Stelling,	Technische Universiteit Delft, promotor
Prof. dr ir J.A. Battjes,	Technische Universiteit Delft
Prof. dr ir A.W. Heemink,	Technische Universiteit Delft
Prof. dr ir P. Wesseling,	Technische Universiteit Delft
Prof. dr ir E. Deleersnijder,	Université Catholique de Louvain, België
Dr A.F. Blumberg,	HydroQual Inc., U.S.A.

Copyright © 2001 by Marco Bijvelds
Typeset by AMS-~~L~~T_EX
Printed by PrintPartners Ipskamp B.V.

ISBN 90-9014606-7

This thesis is also published in the series 'Communications on Hydraulic and Geotechnical Engineering' of the Faculty of Civil Engineering as Report No. 01-2, ISSN 0169-6548.

Abstract

Numerical computational models are important tools in the understanding and the forecasting of hydrodynamics, water quality and morphodynamics in estuaries and coastal regions. These models are used increasingly in the decision-making process regarding long-term issues and real-time model predictions. This tendency is enhanced by the increased computer resources of the last decade making the use of three-dimensional models feasible.

The non-linearity of the physics necessitates the use of such three-dimensional models in regions with stratification and large bathymetric variations. However, the horizontal resolution of the computational grid is often inadequate to assure sufficient accuracy of the numerical models with respect to the small-scale phenomena. The accuracy of the solutions can therefore be strongly dependent upon the choice of the computational grid. This is particularly applicable to the vertical grid in regions with strongly varying bathymetry. Often it remains unclear to what extent the results are influenced by the choice of the coordinate system. In this thesis the effects of the vertical coordinate system on the computational results in regions with limited horizontal resolution of the computational grid and large bathymetric variations are identified by means of a consistent comparison of two numerical models with different vertical coordinate systems.

In order to allow for a consistent comparison, two numerical semi-implicit three-dimensional shallow-water models have been developed. Both models employ identical spatial discretisation and time integration and differ in the choice of the vertical coordinate system only. The two most widely used coordinate systems (the geopotential Cartesian coordinate system (z -model) and the boundary fitted σ -coordinate system (σ -model)) are adopted in these models.

The σ -coordinate model used in this thesis is based upon the σ -coordinate model of the Delft3D system of Delft Hydraulics. Some simplifications have been implemented for reasons of computational efficiency. The related decrease of the accuracy of the model was considered to be irrelevant for the comparison of the σ -model and z -model. The Cartesian z -model has been newly developed as a part of this thesis. Although this model is very similar to the σ -model, small differences exist near the boundaries. The numerical treatment of the flow near the free surface and the bottom boundary requires special attention in the z -model in order to obtain satisfactory results. The errors in the σ -model related to the approximation of the horizontal pressure gradient and the horizontal diffusion have been minimised by application of the method of Stelling and Van Kester.

Comparison of the model results to laboratory measurements and field measurements shows that large discrepancies between the z -model and σ -model occur in regions with strongly varying bathymetry, especially in the case of stratified flow. Models with a relatively coarse horizontal computational grid (compared to a typical length scale of the geometry) give rise to these discrepancies. In regions with relatively smooth topography the departures between the results of both models are insignificant.

As a general conclusion it may be stated that for the modelling of estuarine flow with

relatively coarse horizontal grids, a vertical grid should be chosen in which the orientation of the grid lines coincides with the anticipated flow field and density gradients as much as possible. Furthermore, the accuracy of the transport schemes is of great importance in order to reduce numerical cross-wind diffusion which may greatly hamper the quality of the model results. In some cases it may prove necessary to use computational grids with a high horizontal resolution (with a grid spacing of the order of the water depth) in order to resolve the vertical structure of the flow satisfactorily.

Besides the inaccuracies due to the numerical treatment of the differential equations, uncertainties concerning the physics give rise to departures between the computational results and observations. This applies in particular to the description of turbulent exchange of momentum and dissolved matter.

The k - ε model is used frequently for the turbulence modelling of free surface flows. The effect of the turbulent eddies on the mean flow is modelled by means of an eddy viscosity, which is computed by the k - ε -model. In this model the turbulence is assumed to be isotropic. However, in shallow-water flow bottom friction induced three-dimensional turbulence and large turbulent structures may coexist. The length scales of the large turbulent structures are typically several times the water depth. These quasi-two-dimensional structures give rise to large differences in turbulent transport in the horizontal and the vertical direction. The standard k - ε turbulence model is not capable of modelling this type of turbulence.

In this thesis a new two-length-scale turbulence model is described that takes anisotropy of shallow-water turbulence into account. This model yields an anisotropic eddy viscosity that is related to the small-scale turbulence as well as the large-scale quasi-two-dimensional turbulence. The small-scale three-dimensional turbulence is modelled by a three-dimensional k - ε model in which the production of turbulent kinetic energy is determined solely by vertical velocity gradients. The larger scale quasi-two-dimensional turbulence is modelled with a depth-averaged k - ε turbulence model in which the turbulent kinetic energy is produced by horizontal velocity gradients only. The direct interaction of the two separate turbulent length scales is neglected, although interaction via the mean flow exists.

In order to validate the new turbulence model laboratory measurements were carried out. These measurements reveal that the large turbulent structures give rise to large horizontal Reynolds shear stresses. Despite the limitations and assumptions of the two-length-scale turbulence model, the computed horizontal Reynolds shear stresses are in good agreement with the measurements. The standard k - ε turbulence model, on the other hand, yields a significant underestimation of these turbulent stresses. In the case of three-dimensional applications, the new turbulence model only gives rise to a slight increase of the computational effort.

Samenvatting

Numerieke rekenmodellen vormen een belangrijk gereedschap bij het begrijpen en voorspellen van de waterbeweging, waterkwaliteit en morfodynamica in estuaria en kustgebieden. Bij zowel de besluitvorming over lange termijn beheersaspecten als operationele voorspellingen worden deze modellen in toenemende mate ingezet. Deze tendens wordt versterkt door de toegenomen rekencapaciteit in de afgelopen decennia wat het gebruik van driedimensionale modellen mogelijk heeft gemaakt.

De niet-lineariteit van de fysica maakt het gebruik van deze driedimensionale modellen noodzakelijk in gebieden die gekenmerkt worden door stratificatie en grote variaties in de bodemligging. Echter, in grootschalige toepassingen is de horizontale resolutie van het rekenrooster vaak nog ontoereikend om voldoende nauwkeurigheid van de numerieke modellen te kunnen garanderen met betrekking tot kleinschalige fenomenen. De nauwkeurigheid van de verkregen oplossingen kan hierdoor sterk afhankelijk zijn van de keuze van het rekenrooster. Dit geldt met name voor de keuze van het verticale rekenrooster in gebieden met een sterk variërende bodemligging. Vaak is onduidelijk in welke mate de resultaten door deze keuze van het coördinatenstelsel worden beïnvloed. Door middel van een consistent vergelijk van twee numerieke modellen met verschillende verticale coördinatenstelsels worden in dit proefschrift de effecten van het verticale coördinatenstelsel op de rekenresultaten bepaald in gebieden met beperkte horizontale resolutie van het rekenrooster en grote variaties in de bodemligging.

Om een consistent vergelijk mogelijk te maken zijn twee semi-impliciete driedimensionale numerieke ondiepwatermodellen ontwikkeld die gebruik maken van dezelfde ruimtelijke discretisatie en tijdsintegratie en alleen verschillen in de keuze van het verticale coördinatenstelsel. De twee meest gebruikte verticale coördinatenstelsels (het geopotentiale Cartesische coördinatenstelsel (z -model) en het "boundary fitted" σ -coördinatenstelsel (σ -model)) zijn in deze modellen toegepast.

Het σ -coördinatenmodel dat gebruikt wordt in dit proefschrift, is gebaseerd op het σ -coördinatenmodel van het Delft3D systeem van het Waterloopkundig Laboratorium. Enkele vereenvoudigingen zijn geïmplementeerd omwille van de efficiëntie van het numerieke model. De bijbehorende afname van de nauwkeurigheid van het model wordt geacht van ondergeschikt belang te zijn voor het onderlinge vergelijk van het σ -model en z -model. Het Cartesische z -model is nieuw ontwikkeld. Hoewel dit model sterke gelijkenissen vertoont met het σ -model zijn er kleine verschillen tussen de modellen nabij de modelranden. Om bevredigende resultaten te verkrijgen vereist de numerieke afhandeling van de stroming bij het vrije wateroppervlak en de bodem extra aandacht in het z -model. De problemen met betrekking tot de berekening van de horizontale drukgradiënt en horizontale diffusie in het σ -model zijn zoveel mogelijk beperkt door deze te berekenen met de methode zoals ontwikkeld door Stelling en Van Kester.

Vergelijking van modelresultaten met laboratoriummetingen en veldmetingen laat zien dat grote discrepanties tussen het z -model en het σ -model voorkomen in gebieden met

sterk variërende bodemligging, met name daar waar stratificatie optreedt. Modellen met een relatief grof horizontaal rekenrooster (in verhouding tot de typische lengteschaal van de geometrie) geven aanleiding tot deze discrepanties. In gebieden met relatief kleine variaties in de bodemligging zijn de afwijkingen tussen beide modellen gering.

Als algemene conclusie kan worden gesteld dat voor de modellering van de waterbeweging in estuaria een verticaal rekenrooster gekozen dient te worden waarvan de oriëntatie van de roosterlijnen zoveel mogelijk samenvalt met het te verwachten stromingsveld en dichtheidsgradiënten. Daarnaast is de nauwkeurigheid van de gebruikte transportschema's van groot belang om artificiële menging te reduceren. Deze menging kan de nauwkeurigheid van de verkregen resultaten sterk negatief beïnvloeden. In sommige gevallen kan het gebruik van rekenroosters met een hoge horizontale resolutie (met een maaswijdte van de orde van grootte van de waterdiepte) nodig blijken te zijn om verticale structuren van de stroming goed te kunnen weergeven.

Naast de onnauwkeurigheden in de numerieke afhandeling van de differentiaalvergelijkingen geven de onzekerheden in de beschrijving van de fysica aanleiding tot afwijkingen tussen de rekenresultaten en observaties. Dit geldt in het bijzonder voor de beschrijving van de turbulente menging van impulsen en opgeloste stof.

Voor de modellering van deze turbulentie in vrije oppervlaktestromingen wordt veelvuldig gebruik gemaakt van het zogenaamde $k-\epsilon$ turbulentiemodel. Dit model beoogt de effecten van turbulente wervels op de gemiddelde waterbeweging weer te geven middels een door het model berekende turbulente viscositeit. Isotropie van turbulentie is hierbij een van de uitgangspunten. Echter, in ondiepwaterstroming kunnen naast de door bodemwrijving opgewekte driedimensionale turbulentie grootschalige turbulente wervels voorkomen met afmetingen die aanzienlijk groter zijn dan de waterdiepte. Deze wervels zijn quasi-tweedimensionaal van structuur en geven aanleiding tot grote verschillen in turbulent transport in horizontale en verticale richting. Deze turbulentie kan met het standaard $k-\epsilon$ -model niet goed worden gemodelleerd.

Dit proefschrift beschrijft een tweelengteschalen $k-\epsilon$ turbulentiemodel dat rekening houdt met deze anisotropie van de turbulentie. De met het model verkregen anisotrope turbulente viscositeit is gerelateerd aan zowel de kleinschalige turbulentie als de grootschalige quasi-tweedimensionale turbulentie. De kleinschalige driedimensionale turbulentie wordt in dit model gemodelleerd met een driedimensionaal $k-\epsilon$ model waarin de productie van turbulente kinetische energie alleen afhankelijk is van snelheidsgradiënten in verticale richting in de stroming. De grootschalige quasi-tweedimensionale turbulentie wordt gemodelleerd met een dieptegemiddeld $k-\epsilon$ turbulentiemodel waarin de turbulente kinetische energie slechts door horizontale snelheidsgradiënten wordt geproduceerd. Hoewel interactie via de gemiddelde stromingsvergelijkingen aanwezig is wordt directe interactie tussen de twee turbulente lengteschalen verwaarloosd.

Laboratoriummetingen zijn uitgevoerd ter validatie van het nieuwe turbulentiemodel. Deze metingen laten zien dat de aanwezigheid van de grote turbulente structuren aanleiding geeft tot hoge waarden voor de horizontale Reynoldsschuifspanning. Ondanks de

beperkingen en aannamen van het tweelengteschalenmodel komen de berekende waarden voor deze horizontale Reynoldsschuifspanningen goed overeen met metingen. Het standaard k - ε turbulentiemodel geeft hier een duidelijke onderschatting van deze turbulente spanningen. Voor driedimensionale toepassingen geeft het nieuwe turbulentiemodel slechts aanleiding tot een marginale verhoging van de rekentijd.

Contents

Abstract	v
Samenvatting	vii
1 Introduction	1
1.1 Background	1
1.2 Vertical coordinate systems	2
1.3 Turbulence modelling	6
1.4 Aim of the research	8
1.5 Outline of the thesis	9
2 Numerical model definition	11
2.1 Governing equations in Cartesian coordinates	12
2.2 Transformed equations in σ -coordinates	15
2.3 Turbulence closure	17
2.3.1 Eddy viscosity concept	17
2.3.2 Single-length-scale turbulence models	18
2.3.3 Single-length-scale k - ε model	21
2.4 Boundary and initial conditions	23
2.5 Time integration and spatial discretisation	24
2.5.1 Definition of the vertical coordinate systems	25
2.5.2 Flooding and drying	26
2.5.3 Horizontal gradients in σ -coordinates	27
2.5.4 Discretisation momentum equation	31
2.5.5 Discretisation continuity equation	38
2.5.6 Discretisation transport equation	38
2.5.7 Discretisation standard k - ε turbulence model	42
3 Two-length-scale k-ε model	45
3.1 Introduction	45
3.2 Anisotropic eddy viscosity	46

3.3	Two-length-scale k - ϵ model	48
3.3.1	Model equations	48
3.3.2	Model assumptions and limitations	49
3.3.3	Boundary and initial conditions	51
3.3.4	Discretisation two-length-scale turbulence model	51
4	Application of the two-length-scale k-ϵ model	55
4.1	Laboratory measurements yacht harbour "t Steel"	55
4.1.1	Introduction	55
4.1.2	Experimental set-up	56
4.1.3	Experimental results	57
4.2	Driven cavity flow in a square model harbour	60
4.2.1	Model description	60
4.2.2	Computational results	61
4.3	Modelling yacht harbour "t Steel"	68
4.3.1	Computational results	69
4.4	Discussion	74
5	Comparison of the σ- and z-coordinate model	77
5.1	Model assessment using two-dimensional test cases	78
5.1.1	Steady channel flow	78
5.1.2	Standing wave	80
5.1.3	Exchange flow	80
5.1.4	Buoyant plume on a sloping bottom	83
5.1.5	Summary of the model assessment results	88
5.2	Haringvliet estuary	88
5.2.1	Model input	90
5.2.2	Computational results	93
5.3	Lake Veere	95
5.3.1	Model input	97
5.3.2	Computational results	99
5.3.3	Two-dimensional schematisation Lake Veere	104
5.4	Discussion	109
6	Conclusions and recommendations	111
6.1	Vertical coordinate system: σ vs. z	111
6.2	Shallow-water turbulence modelling	114
6.3	Summary	116
	References	119

<i>Contents</i>	xiii
A Laboratory measurements yacht harbour " 't Steel"	127
B Expressions for the horizontal pressure gradient in σ-coordinates	131
List of Symbols	133
Dankbetuiging	137
Curriculum Vitae	138

Chapter 1

Introduction

1.1 Background

The word estuary is derived from the Latin word *aestus* which means tide and can be defined as a semi-enclosed coastal body of water which has a free connection with the open sea, extending into a river as far as the limit of tidal influence, and within which sea water is measurably diluted with fresh water derived from land drainage (Cameron & Pritchard, 1963; Dyer, 1997).

Easy access to the sea and safe anchorage have made many estuaries the location of early settlements. Initially the natural waterways provided sufficient navigable depth to accommodate small vessels. However, as a result of increasing populations and the development of industry, the estuarine basins needed modification to better suit their changing roles. This initiated the dredging of navigation channels and the building of ports and has led to the discharge of industrial and household waste water. Over the years this has had a great influence on estuarine hydrodynamics and water quality.

In order to understand and assess the response of the natural systems to these changes, numerical models of circulation and transport have become important tools in water management. These models are generally based on the so-called shallow-water equations. These equations are derived from the Reynolds-averaged Navier-Stokes equations assuming that the pressure variation is hydrostatic. The differential equations are solved for the time variation of the surface elevation of the water and the flow velocity. This is done by approximating the continuous equations on a discrete grid with a finite number of grid points. For the discrete approximation of the continuous equations many numerical methods have been proposed in the past, see Haidvogel & Beckmann (1999) and Cheng & Smith (1990) for a review. When coupled with appropriate equations for solute transport it is possible to model the fate of pollutants, assess water quality and predict sediment movements.

The use of these tools in decision-making demands mathematical models that are both versatile and accurate. Because estuaries are characterised by the presence of stratification

and large bathymetric variations and due to the non-linearity of the physics, this accuracy requirement necessitates the use of three-dimensional models. However, discrepancies between the results of these models and field measurements are observed in modelling estuarine hydrodynamics. The inaccuracies may to a large extent be ascribed to the use of relatively coarse grids in the prevailing flow direction for large-scale applications. Although three-dimensional modelling has become feasible due to the increasing computing resources of the last decade, relatively small grid spacing (of the order of meters and smaller) is still not feasible for modelling the unsteady hydrodynamics in estuaries in order to limit the computational time. In the vertical direction (i.e. the direction in which the gravity acts), on the other hand, the grid spacing is much smaller due to the limited water depth. The structure of the shallow-water flow is assumed to allow anisotropy of the computational grid, i.e. large aspect ratio's of the horizontal and vertical grid spacing $\Delta x/\Delta z$. Yet, numerical problems may arise due to the anisotropy of the grid. Depending on the local flow direction with respect to the computational grid, inaccuracies in the computational results can be anticipated, especially in the case of stratified flow in combination with **strong variation of the bottom profile. In the following the potential problems related to this are discussed.** Furthermore, attention is paid to the estimation of the horizontal eddy viscosity in large-scale as well as small-scale applications. In the latter the horizontal eddy viscosity is related to the turbulent motion of the flow while the horizontal eddy viscosity in large-scale applications is mainly determined by the horizontal grid spacing.

1.2 Vertical coordinate systems

The discharge of fresh river water into the sea induces stratification in coastal regions. Locally large gradients of salinity and temperature may be encountered. In the Rotterdam Waterway for example, the vertical density distribution almost becomes a step function under certain conditions (De Kok, 1994). In contrast with the large density gradients in the vertical direction, the variation of scalar quantities in the local flow direction - which is predominantly near-horizontal in shallow-water flow - are usually much more gradual. **An exception are the density gradients near the front of gravity currents, such as the salt wedge in the Rotterdam Waterway.**

The correct representation of density interfaces is important since their presence affects the movement of water and thereby the dispersion of dissolved matter such as pollutants. Resolving these density interfaces and maintaining the stratification is one of the key problems met in numerical modelling of estuaries. Sufficient resolution of the computational grid near the density interface is a prerequisite for resolving the interfaces. Due to the limited water depth in estuaries, the vertical grid spacing is often sufficiently small to resolve the large gradients. In general, the anisotropy of the computational grid is therefore assumed not to impose severe problems regarding the accuracy of the numerical solution. However, this assumption is only valid when the anisotropy of the grid structure coincides

with the anisotropy of the flow- and density structure, see Figure 1.1. This is often not the case.

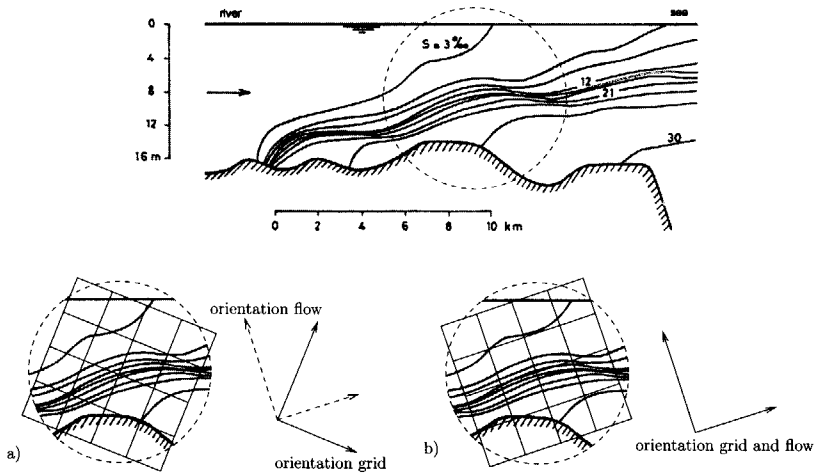


Figure 1.1: Typical distribution of scalar quantities in an estuary. Large gradients are encountered in the (near) vertical direction while the variation of salinity and temperature is much smaller in the flow direction (except near the front of the gravity current). Depending on the respective orientation of the anisotropic grid and these scalar variables, artificial mixing may either affect the computational results significantly (a) or may be negligible (b).

In order to minimise the effects of this artificial diffusion, high resolution of the computational grid is therefore required in both the horizontal and the vertical direction. This is, however, not feasible at present. This implies that in many applications the results do not represent accurate solutions and therefore strongly depend on the grid definition. The accurate representation of the vertical exchange processes is thus to a large extent determined by the vertical grid system employed. Furthermore, the use of accurate numerical schemes is preferred for the approximation of advective transport, again in order to minimise numerical diffusion. A wide range of advection schemes is available from the literature and an overview of these is given by Hirsch (1990), Koren & Vreugdenhil (1993) and Zijlema (1996), for example.

To minimise the errors related to the vertical grid system, many models have been developed in the past that are based on different coordinate systems, see Haidvogel & Beckmann (1999) for a review. Ideally, the vertical grid should resolve the boundary layer near the bottom to allow for an accurate evaluation of the bed stress, be fine around pycnoclines and avoid large truncation errors in the approximation of strict horizontal gradients. In order to fulfil these conditions grid adaptation is necessary. However, generalised vertical

grids may locally become very unsmooth introducing new truncation errors. Besides, the Jacobian of these grids is dependent on the vertical coordinate and therefore needs to be evaluated locally every time step which decreases the efficiency of the numerical model. Alternatively, the isopycnal coordinate system may be adopted. This coordinate system is widely used for oceanographic applications but may be less appropriate for estuarine modelling. This is due to the fact that layers tend to converge and regularly intersect the surface and bottom, causing severe numerical difficulties. The widely used terrain-following σ -coordinate and the geopotential z -coordinate (or a combination of both) appear most suitable for modelling the flow in coastal regions. Therefore, two numerical models are presented in this thesis that are based on the σ -coordinate and the Cartesian z -coordinate. A schematic of both grid definitions is depicted in Figure 1.2. Neither of these coordinate systems meet all of the above mentioned requirements and therefore introduce errors under certain conditions.

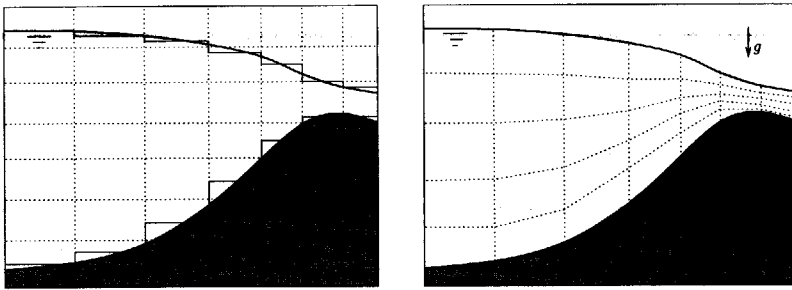


Figure 1.2: Schematic of the Cartesian z -coordinate system (left) and the boundary fitted σ -coordinate system (right).

The σ -coordinate models provide an accurate representation of the bathymetry and **are therefore well-suited for simulating bottom boundary layer processes**. The models permit simple treatment of the boundary conditions at the bottom and free surface and make efficient use of computer resources. Although the preceding advantages of the terrain-following coordinate system are evident, the method also has some drawbacks. The relative thickness of the computational grid cells does not depend on the horizontal coordinates x and y which gives rise to unnecessarily high grid resolution in shallow areas and possibly insufficient grid resolution in deeper parts of the computational domain. Furthermore, in very shallow drying areas, the mapping may become singular. In regions with varying bathymetry the numerical scheme may even become non-convergent due to hydrostatic inconsistency (Haney, 1991).

Further numerical problems may arise near steep bottom slopes combined with vertical

stratification of the density. The approximation of strictly horizontal gradients in areas with steep bottoms causes errors in σ -models. (Janjić, 1977; Mesinger, 1982; Haney, 1991). This is caused by the fact that the horizontal derivatives in Cartesian coordinates are split into two terms in σ -coordinates. Sometimes horizontal derivatives that are almost zero result from two large derivatives that should cancel. In that case, truncation errors in the approximation of both terms may result in a relatively large error. In particular the error in approximating the pressure gradient error has been addressed often in the literature, see Gary (1973), Janjić (1977), Mesinger (1982), Haney (1991), Deleersnijder & Beckers (1992), Mellor *et al.* (1994), Stelling & Van Kester (1994), Burchard & Petersen (1997), Slørdal (1997) and Kliem & Pietrzak (1999), for example. For stratified flows over steep slopes, the currents induced by discretisation errors may be as large as the typical physical velocities (Walters & Foreman, 1992). Various methods have been proposed to reduce these errors, *e.g.* by subtracting a reference state density field before computing the pressure gradient terms (Gary, 1973), or by using higher-order finite difference approximation in the horizontal (McCalpin, 1994). While these methods work well in idealised process studies with relatively smooth topography, the improvement is less significant in coarser-resolution applications (Haidvogel & Beckmann, 1999). An interesting method to reduce the pressure gradient error is proposed by Stelling & Van Kester (1994). Their method is based on the evaluation of horizontal gradients along strictly horizontal planes. Stelling & Van Kester (1994) present a finite volume method in which horizontal derivatives are determined in Cartesian coordinates by rotating finite volumes to become rectangular. By doing so, the hydrostatic consistency condition does not have to be satisfied. Moreover, the authors show that for diffusion their method is both monotonic and positive due to the non-linear interpolation of variables.

Another problem related to the σ -transformation is due to the non-conformality of the mapping. The transformation is not angle preserving which leads to additional terms that are proportional to horizontal gradients of the total water depth. For the diffusion terms this leads to cross-derivative terms. Assuming mild slopes, these terms are often neglected in order to simplify implementation and to anticipate problems concerning accuracy, stability and monotonicity. In the presence of steep topography this may lead to significant errors, Paul (1994) and Podber & Bedford (1994).

The Cartesian z -coordinate model does not employ boundary fitted coordinates in the vertical direction and therefore the number of grid cells in the vertical direction varies in space and time. Because of this, the Cartesian grid remains aligned with the contouring lines of the stratification in regions with strong bathymetric variations. This is important in order to reduce vertical mixing of scalar properties such as salinity and temperature. The representation of the bottom and free surface imposes most of the problems in Cartesian z -coordinate models. The representation of the bottom leads to inaccuracies in the approximation of the bed stress and the horizontal advection near the bed, Fortunato & Baptista (1994). Hence, the z -coordinate model is less appropriate for simulating bottom boundary processes than boundary fitted models. High resolution is needed to model

boundary layer flow properly (Burchard & Petersen, 1997).

Although quite some attention has been paid to the problems related to the above models, very few consistent comparisons of both approaches is available in the literature. Therefore it often remains unclear whether differences between results from numerical simulations and observations can be attributed to the errors related to the vertical coordinate system or whether they are due to discretisation of the equations, the schematisation of the geometry or the turbulence model that is used. Only recently Mellor *et al.* (1999) compared a conventional z -level coordinate system, a conventional σ -coordinate system and a generalised σ -scheme for the case of a simplified, wind driven, northern hemisphere basin. To the author's knowledge this is the only work published showing a consistent comparison of different coordinate systems. In this paper the inherent disadvantages of the different coordinate systems are not addressed and no measures were taken to remedy possible errors due to these drawbacks. Moreover, results are only presented for one specific test case.

In the present work a consistent comparison between the z -coordinate model (z -model) and the σ -coordinate model (σ -model) is made by employing similar discretisations for the time and space derivatives in both models. This prevents differences stemming from the method of integration of the partial differential equations. Such a comparison allows conclusions about the difference between the two coordinate systems, without interference of other uncertainties. The intercomparison of the models focuses mainly on regions where both bathymetric variations and stratification occur.

1.3 Turbulence modelling

The Reynolds-averaging of the Navier-Stokes equations process introduces unknown correlations between fluctuating velocities and between scalar fluctuations. Physically these correlations represent transport of momentum and heat or mass due to the fluctuating turbulent motion. The velocity correlations appear to act as stresses on the fluid (Reynolds stresses) while the velocity-scalar correlations represent turbulent heat or mass fluxes.

In order to close the system of equations, these turbulent stresses and fluxes need to be modelled. In correspondence with the numerical inaccuracies mentioned in the previous section, the various assumptions involved in the modelling of the turbulent transport give rise to departures between model results and observations.

This gap is usually bridged by using the eddy viscosity concept or Boussinesq hypothesis. This concept forms the basis of many turbulence models that have been proposed in the literature. Most of these assume that the state of the turbulence can be characterised by one typical velocity and length scale and that the individual Reynolds stresses can be related to these scales. These models vary from zero-equation models to two-equations models consisting of transport equations of turbulent quantities. For an extensive review of the different turbulence models the reader is referred to Rodi (1980), IAHR (1988),

Wilcox (1993).

Usually the turbulence is assumed to be isotropic and therefore the eddy viscosity has no directional dependence, hence the eddy viscosity is a scalar. The order of magnitude of this scalar eddy viscosity ν_t can be estimated by $\nu_t \approx 0.1u_*H \approx 0.01\bar{u}H$, where u_* is the friction velocity, H is the total water depth and \bar{u} is the depth-averaged velocity. This estimate is related to the three-dimensional turbulence which is mainly produced by vertical shear due to bottom friction. In numerical models the viscous terms are only noticeable in the case of cell-Reynolds or Péclet numbers $u\Delta x/\nu_t$ of the order 1 or smaller. Realising that the horizontal grid spacing is typically $\Delta x \sim 10H - 100H$, it can easily be verified that the Péclet number is much larger than one. Hence, viscous effects are negligible in the horizontal plane due to the anisotropy of the computational grid.

The non-linear terms in the momentum equation, *i.e.* the advection terms, give rise to the development of higher harmonics in the numerical model. The related energy transfer from small wave numbers to large wave numbers leads to the accumulation of energy at the smallest length scale resolved, *i.e.* $2\Delta x$. In order to obtain physically realistic solutions, the energy at these small scales needs to be dissipated by some mechanism. This may be achieved by increasing the value of the viscosity that is used for the horizontal viscous term in the momentum equation. Due to this splitting of the eddy viscosity into a vertical and a horizontal component an anisotropic eddy viscosity is obtained. Generally, the value of the horizontal component is much larger than the vertical eddy viscosity. While the latter is related to the transfer of momentum due to the turbulent stresses, the horizontal eddy viscosity is mainly determined by the horizontal grid spacing and its value has no direct physical meaning. The latter is usually computed by means of the Smagorinsky model (Smagorinsky, 1963). Alternatively, the computations can be stabilised by employing upwind-biased schemes for the numerical approximation of the advection terms. Using this approach, the energy dissipation is due to the numerical dissipation related to the upwind-biased schemes, *e.g.* (Hirsch, 1990).

The approximation of the horizontal viscosity terms in the numerical models has gained increasing attention recently in modelling small-scale processes in estuaries. For example the water movement in the vicinity of sluices and groynes and the transport of matter in harbours are to a large extent determined by horizontal turbulent transfer processes. In order to model these physical phenomena properly, a sound estimate of the horizontal Reynolds stresses is imperative. This has led to the demand for turbulence models that are capable of predicting the value of the horizontal eddy viscosity and eddy diffusivity more accurately.

Induced by the limited water depth, the turbulent transport in the horizontal direction may differ significantly from the turbulent transport in the vertical direction in shallow-water flow. Detailed experiments on large turbulent structures in jets and wakes (Dracos *et al.*, 1992; Jirka, 1998) and mixing layers (Uijttewaai & Tukker, 1998; Uijttewaai & Booij, 2000) under shallow-water conditions reveal that under certain conditions large coherent turbulent structures may be present in the shallow flow with a characteristic length scale

(significantly) larger than the water depth. The above studies differ essentially from early research on two-dimensional turbulence (*e.g.* (Kraichnan, 1967; Batchelor, 1969)) due to the fact that effects of bottom friction are included in the former studies.

From energy density spectra of the turbulence fluctuations and from the phase relation between the two velocity components in the horizontal plane, Uijttewaal & Booij (2000) conclude that these large turbulent structures contribute most to the exchange of momentum and thus to the Reynolds stresses in mixing layers.

The presence of the large turbulent structures is governed by the ratio of horizontal velocity gradients - which feed the turbulent eddies - and the stabilising effect of the bottom friction on the large structures. By pairing of turbulent eddies - which have dominant vertical vorticity component caused by the kinematic constraints under shallow-water conditions - the typical length scale of the eddies may grow to several times the water depth. The large scale structures thus created are hardly affected by the small-scale three-dimensional turbulence. Moreover, since vortex stretching of the large scale structures is impeded and the large structures are well organised with respect to each other, these large-scale structures have a long lifetime. This type of turbulence is usually indicated by quasi-two-dimensional turbulence.

Besides the quasi-two-dimensional turbulence, small-scale three-dimensional turbulence is present in the flow with a typical length scale of the water depth. This type of turbulence is mainly generated by vertical shear due to bottom friction. This leads to a disparity of turbulent length scales. Obviously, the use of a scalar eddy viscosity, which only accounts for one dominant turbulent length scale, then becomes inappropriate. Under these circumstances the single-length-scale turbulence models are therefore likely to fail. The disparity of turbulent time scales and length scales should be accounted for separately, instead of uniting them in one eddy viscosity term.

In the present work a new two-length-scale turbulence model is presented which accounts for the presence of both the small-scale three-dimensional turbulence and the large scale quasi-two-dimensional turbulence. This is achieved by using the above mentioned splitting of the eddy viscosity into a horizontal and a vertical part. The small-scale bottom generated turbulence, which is essentially three-dimensional, is modelled by a three-dimensional k - ϵ model in which the production of turbulent kinetic energy is determined solely by vertical velocity gradients. The larger scale quasi-two-dimensional turbulence is modelled with a depth-averaged k - ϵ turbulence model in which the turbulent kinetic energy is produced by horizontal velocity gradients only. In three-dimensional applications the new turbulence model is hardly more expensive than the standard k - ϵ turbulence model.

1.4 Aim of the research

This thesis deals with the three-dimensional numerical modelling of estuarine flow processes. Attention is focused on two aspects of this modelling. The first aim is to identify

the effects of the vertical coordinate system on the computational results in regions with limited horizontal resolution and large bathymetric variations. Secondly we concentrate on the modelling of shallow-water turbulence. Related to this, the second aim is the development of a turbulence model that takes anisotropy of shallow-water turbulence into account. This model should therefore yield an anisotropic eddy viscosity that is related to the small-scale turbulence as well as the large-scale quasi-two-dimensional turbulence.

1.5 Outline of the thesis

First, in Chapter 2, the governing equations for the z - and σ -coordinate model are given including the equations of the three-dimensional k - ε turbulence model. The spatial discretisation and the time integration of the partial differential equations are described. The numerical techniques employed in both model approaches are identical to allow for a consistent comparison. Furthermore, the advantages and disadvantages of the σ -coordinate model and the z -coordinate model are discussed, as are some remedies to minimise the inherent disadvantages of both coordinate systems.

In Chapter 3 emphasis is laid on the modelling of shallow-water turbulence. A new two-length-scale turbulence model is presented that takes disparity of turbulent length and time scales into account. The model equations and their numerical treatment are given in this chapter. The model assumptions and restrictions are also addressed in this chapter.

In Chapter 4 the performance of the two-length-scale turbulence model is assessed. Mean flow characteristics of the flow in a square harbour at laboratory scale are compared to measurements reported in the literature. Additional laboratory experiments (LDA) were carried out in a more complex harbour geometry in order to compare measured and computed Reynolds stresses.

In Chapter 5 the comparison of the σ -coordinate shallow-water model and the z -coordinate shallow-water model is made. Several test cases, ranging from stratified flow on laboratory scale to prototype flows in estuaries are presented and the results are discussed.

The conclusions of the present work and recommendations for future research are stated in Chapter 6.

Chapter 2

Numerical model definition

In this chapter two three-dimensional shallow-water models are described that employ the widely used geopotential z -coordinate and the boundary-fitted σ -coordinate. The aim of the development of these models is to identify the effects of the vertical coordinate system on the computational results in regions with varying bathymetry. In order to allow for a consistent comparison, both models employ identical time integration and spatial discretisation.

The σ -coordinate model is based upon the σ -coordinate model of the Delft3D system of Delft Hydraulics (Delft Hydraulics, 1999). Some simplifications were implemented for reasons of computational efficiency. Obviously, the accuracy of the model has thereby formally decreased but this is believed to be of minor importance since our primary interest is in the intercomparison of the two models. The Cartesian z -model has been newly developed.

The following contains the time integration and spatial discretisation of the present models. While most of these are standard and well documented in the literature, some adjustment of the standard techniques appeared to be necessary to ensure the optimal performance of the models. Therefore particular attention is paid to the following features:

- treatment of the free surface movement in the z -model
- conservative scalar transport in the z -model
- bottom shear stress in the z -model
- implementation of the advective terms
- vertical and horizontal gradients of scalar quantities in the σ -model

Before discussing the numerics, the underlying equations are first given in the next section. These equations are derived from the Reynolds-averaged Navier-Stokes equations. In coastal regions these equations may be simplified by adopting the hydrostatic pressure

assumption and the Boussinesq hypothesis. The resulting shallow-water equations still contain unknown correlations - the Reynolds stresses - that need to be modelled in order to close the system of equations. This gap is bridged by applying a k - ε turbulence model which is based on the eddy viscosity concept. The turbulence model accounts for the three-dimensional turbulence that is generated by shear, in particular near the bottom. In addition, the transformed momentum equation and transport equation are given in σ -coordinates.

2.1 Governing equations in Cartesian coordinates

The three-dimensional (3D) numerical models described in this chapter are based on the shallow-water equations. These equations are derived starting from the mass conservation equation:

$$\frac{\partial \rho}{\partial t} + \frac{\partial u_i \rho}{\partial x_i} = \frac{D\rho}{Dt} + \rho \frac{\partial u_i}{\partial x_i} = 0, \quad (2.1)$$

with

$$\frac{D}{Dt} = \frac{\partial}{\partial t} + u_i \frac{\partial}{\partial x_i}. \quad (2.2)$$

In eq. (2.1) ρ is the density of the fluid, t is the time, u_i is the velocity and x_i is the Cartesian coordinate¹. For an incompressible fluid, the rate of change of ρ following the motion is zero, hence $D\rho/Dt = 0$, and eq. (2.1) then reduces to

$$\frac{\partial u_i}{\partial x_i} = 0. \quad (2.3)$$

The conservation of momentum is given by the Reynolds-averaged Navier-Stokes equations². In Cartesian coordinates the resulting equation reads

$$\frac{\partial \rho u_i}{\partial t} + \frac{\partial \rho u_i u_j}{\partial x_j} + \frac{\partial \overline{\rho u'_i u'_j}}{\partial x_j} + \frac{\partial p}{\partial x_i} - \frac{\partial \sigma_{ij}}{\partial x_j} + \rho \varepsilon_{ijk} 2\Omega_j u_k = \rho F_i, \quad (2.4)$$

where $\overline{u'_i u'_j}$ is the Reynolds stress per unit mass which arises after averaging of the Navier-Stokes equation (see section 2.3), p is the pressure, σ_{ij} is the mean deviatoric stress tensor, ε_{ijk} is the permutation symbol, $2\Omega_j$ is the planetary vorticity³ and F_i is the volume force per unit mass. In turbulent flows, the Reynolds stresses are much larger than the viscous

¹Using tensor notation the Cartesian coordinate x_i and velocity u_i are equal to x, y, z and u, v, w for $i=1,2,3$, respectively

²The continuity equation eq. (2.3) remains unaltered after applying Reynolds averaging

³ $\Omega = (\Omega_1, \Omega_2, \Omega_3) = (0, \Omega \cos \phi, \Omega \sin \phi)$ where ϕ is the geographic latitude.

stresses and the latter are therefore neglected. The last term of the left-hand-side is due to the rotation of the earth and is known as the Coriolis force.

For small density differences ($\Delta\rho/\rho_0 \ll 1$, where ρ_0 is a reference density), the Boussinesq approximation may be applied which means that the variation of the density may be neglected in all terms except the buoyancy term. Using eq. (2.1) and taking $F_i = g\delta_{i3}$, where g is the gravitational acceleration and δ_{ij} is the Kronecker delta, we then arrive at

$$\frac{\partial u_i}{\partial t} + u_i \frac{\partial u_j}{\partial x_i} + \frac{1}{\rho_0} \frac{\partial p}{\partial x_i} - \frac{1}{\rho_0} \frac{\partial \tau_{ij}}{\partial x_j} + \varepsilon_{ijk} 2\Omega_j u_k = \frac{\rho}{\rho_0} g \delta_{i3}, \quad (2.5)$$

where $\tau_{ij} = -\rho \overline{u'_i u'_j}$.

In the applications that are considered here, the characteristic length scale of the flow in the vertical direction is much smaller than a characteristic length scale in the horizontal direction. Under these conditions, the three dimensional Reynolds-averaged Navier-Stokes equations may be reduced to the boundary layer form. The momentum equation in x_3 direction then reduces to the hydrostatic pressure assumption ⁴:

$$\frac{\partial p}{\partial x_3} = -\rho g. \quad (2.6)$$

The assumption of shallow fluid implies $w \ll u, v$ and therewith

$$\varepsilon_{ijk} 2\Omega_j u_k = (-fu, fv, 0), \quad (2.7)$$

in which $f = 2\Omega \sin\phi$ is the Coriolis parameter. For not-too-large meridional scales (< 1000 km) f may be assumed to be constant. This results in the following momentum equations:

$$\frac{Du}{Dt} = -\frac{1}{\rho_0} \frac{\partial}{\partial x} \int_{z'=z}^{z'=\zeta} \rho g dz' + \frac{1}{\rho_0} \left(\frac{\partial \tau_{xx}}{\partial x} + \frac{\partial \tau_{xy}}{\partial y} + \frac{\partial \tau_{xz}}{\partial z} \right) - fv, \quad (2.8a)$$

$$\frac{Dv}{Dt} = -\frac{1}{\rho_0} \frac{\partial}{\partial y} \int_{z'=z}^{z'=\zeta} \rho g dz' + \frac{1}{\rho_0} \left(\frac{\partial \tau_{yx}}{\partial x} + \frac{\partial \tau_{yy}}{\partial y} + \frac{\partial \tau_{yz}}{\partial z} \right) + fu, \quad (2.8b)$$

where ζ is the free surface elevation. These equations are known as the shallow-water equations. The shallow-water equations in general coordinates can be found in Dunsbergen (1994).

The transport equation for scalar quantities is given by

$$\frac{Dc}{Dt} = \frac{\partial}{\partial x} \left(D_t \frac{\partial c}{\partial x} \right) + \frac{\partial}{\partial x} \left(D_t \frac{\partial c}{\partial y} \right) + \frac{\partial}{\partial z} \left(D_t \frac{\partial c}{\partial z} \right) + s, \quad (2.9)$$

⁴The vertical velocity w is determined by continuity only

where c is a scalar quantity (heat or salinity), $D_t = \nu_t/\sigma_t$ is the eddy diffusivity with σ_t being the Prandtl/Schmidt number and s is a source or sink term. In the transport equation for dissolved salt the latter terms represent a incoming or outgoing flux of salt due to the discharge or withdrawal of water. The source and sink terms of the heat equation are more complex. In the present model these terms are computed by a so-called absolute temperature model, (Delft Hydraulics, 1999). In this model the net heat flux through the free surface is determined by the incoming solar radiation Q_s , the back radiation Q_b , convection of heat Q_c and evaporation Q_v :

$$Q_{\text{tot}} = Q_s - Q_b - Q_c - Q_v. \quad (2.10)$$

Usually the incoming radiation (in W/m^2) is based on measured solar radiation and includes the short wave radiation due to the sun as well as the long wave radiation due to the atmosphere and clouds. The loss terms in eq. (2.10) are computed on the basis of wind speed, air temperature, cloudiness and saturation of the air. For details on the temperature module the reader is referred to Delft Hydraulics (1999).

The density ρ follows from an equation of state given by $\rho = \rho(S, T)$ where S is the salinity and T is the temperature of the water. In the present model the expression proposed by Eckart (1958) is adopted.

In shallow-water models, horizontal variation of the density gives rise to pressure gradients. Using Leibniz' rule the pressure gradient can be written as

$$\frac{1}{\rho_0} \frac{\partial p}{\partial x_i} = \frac{\rho g}{\rho_0} \frac{\partial \zeta}{\partial x_i} + \frac{g}{\rho_0} \int_z^{\zeta} \frac{\partial \rho}{\partial x_i} dz', \quad i = 1, 2, \quad (2.11)$$

where the first term on the right-hand-side is the barotropic pressure gradient due to the variation of the free surface elevation and the second term is the baroclinic pressure gradient due to the variation of the density.

In order to compute the barotropic pressure gradient in the numerical model we use the continuity equation eq. (2.3). Integration of this equation with respect to the depth, applying Leibnitz' rule yields

$$\begin{aligned} \frac{\partial}{\partial x} \int_{z=-d}^{\zeta} u dz - u|_{z=\zeta} \frac{\partial \zeta}{\partial x} - u|_{z=-d} \frac{\partial d}{\partial x} + \\ \frac{\partial}{\partial y} \int_{z=-d}^{\zeta} v dz - v|_{z=\zeta} \frac{\partial \zeta}{\partial y} - v|_{z=-d} \frac{\partial d}{\partial y} + w|_{z=-d} - w|_{z=-d} = 0, \end{aligned} \quad (2.12)$$

where d is the depth with respect to a reference level. By inserting the kinematic boundary conditions at the free surface and the bottom

$$w|_{z=\zeta} = \frac{\partial \zeta}{\partial t} + u|_{z=\zeta} \frac{\partial \zeta}{\partial x} + v|_{z=\zeta} \frac{\partial \zeta}{\partial y}, \quad (2.13a)$$

$$w|_{z=-d} = -u|_{z=-d} \frac{\partial d}{\partial x} - v|_{z=-d} \frac{\partial d}{\partial y}, \quad (2.13b)$$

into eq. (2.12), the depth averaged continuity equation is obtained from which the surface elevation is computed in the numerical model:

$$\frac{\partial \zeta}{\partial t} + \frac{\partial}{\partial x} \int_{z=-d}^{\zeta} u dz + \frac{\partial}{\partial x} \int_{z=-d}^{\zeta} v dz = 0. \quad (2.14)$$

2.2 Transformed equations in σ -coordinates

The σ -coordinate used in this thesis is defined as:

$$x^* = x, \quad y^* = y, \quad \sigma = \frac{z - \zeta}{H}, \quad t^* = t. \quad (2.15)$$

Using this definition and applying the chain rule, the time and spatial derivatives in the Cartesian coordinate system are expressed in σ -coordinates as

$$\begin{aligned} \frac{\partial}{\partial t} &= \frac{\partial}{\partial t^*} + \frac{\partial \sigma}{\partial t} \frac{\partial}{\partial \sigma} \\ \frac{\partial}{\partial x_i} &= \frac{\partial}{\partial x_i^*} + \frac{\partial \sigma}{\partial x_i} \frac{\partial}{\partial \sigma}, \quad i = 1, 2 \\ \frac{\partial}{\partial z} &= \frac{\partial \sigma}{\partial z} \frac{\partial}{\partial \sigma} = \frac{1}{H} \frac{\partial}{\partial \sigma}. \end{aligned} \quad (2.16)$$

The superscript * indicates variables that are defined along σ -planes. The hydrostatic pressure relation eq. (2.6) reads in σ -coordinates:

$$\frac{\partial p}{\partial \sigma} = -\rho g H. \quad (2.17)$$

The horizontal velocities u and v remain strictly horizontal after transformation. Hence

$$u = u^*, \quad v = v^*. \quad (2.18)$$

The Cartesian vertical velocity w is defined as $w = Dz/Dt = dz/dt$. Similarly the vertical transformed velocity ω can be obtained by

$$\begin{aligned} \omega = H \frac{D\sigma}{Dt} &= \frac{1}{H} \left(H \frac{Dz}{Dt} - z \frac{DH}{Dt} - H \frac{D\zeta}{Dt} + \zeta \frac{DH}{Dt} \right) \\ &= w - \left(\frac{\partial \zeta}{\partial t} + u \frac{\partial \zeta}{\partial x} + v \frac{\partial \zeta}{\partial y} \right) - \sigma \left(\frac{\partial H}{\partial t} + u \frac{\partial H}{\partial x} + v \frac{\partial H}{\partial y} \right), \end{aligned} \quad (2.19)$$

Using the above expressions the transformed continuity equation and momentum equation read respectively:

$$\frac{\partial \zeta}{\partial t^*} + \frac{\partial H u^*}{\partial x^*} + \frac{\partial H v^*}{\partial y^*} = 0, \quad (2.20)$$

and:

$$\frac{\partial u_i^*}{\partial t^*} + u^* \frac{\partial u_i^*}{\partial x^*} + v^* \frac{\partial u_i^*}{\partial y^*} + \frac{1}{\rho_0} \left(\frac{\partial p^*}{\partial x^*} + \frac{\partial \sigma}{\partial x_i} \frac{\partial p^*}{\partial \sigma} \right) = \frac{1}{\rho_0} \frac{\partial \tau_{ij}^*}{\partial x_j^*} + F_i^*, \quad (2.21)$$

where F_i^* is the Coriolis term. The transformed viscous terms are given by

$$\begin{aligned} \frac{\partial \tau_{xx}^*}{\partial x^*} &= \left(\frac{\partial}{\partial x^*} + \frac{\partial \sigma}{\partial x} \frac{\partial}{\partial \sigma} \right) 2\nu_t^h \left(\frac{\partial u^*}{\partial x^*} + \frac{\partial \sigma}{\partial x} \frac{\partial u^*}{\partial \sigma} \right), \\ \frac{\partial \tau_{xy}^*}{\partial y^*} &= \left(\frac{\partial}{\partial y^*} + \frac{\partial \sigma}{\partial y} \frac{\partial}{\partial \sigma} \right) \nu_t^h \left(\frac{\partial u^*}{\partial y^*} + \frac{\partial \sigma}{\partial y} \frac{\partial u^*}{\partial \sigma} + \frac{\partial v^*}{\partial x^*} + \frac{\partial \sigma}{\partial x} \frac{\partial v^*}{\partial \sigma} \right), \\ \frac{\partial \tau_{xz}^*}{\partial z^*} &= \frac{1}{H^2} \frac{\partial}{\partial \sigma} \nu_t^v \frac{\partial u^*}{\partial \sigma}, \end{aligned} \quad (2.22)$$

where ν_t^v is the vertical eddy viscosity and ν_t^h is the horizontal eddy viscosity. Near sloping bottoms the horizontal eddy viscosity/diffusivity is larger than the vertical eddy viscosity/diffusivity, Mellor & Blumberg (1985). Eq. (2.22) then may lead to a net flux component normal to the bottom that is unphysically large. Following Mellor & Blumberg (1985), the transformation terms of the horizontal viscous terms are neglected in the vertical direction and derivatives are taken along σ -planes. This means that the horizontal viscosity term in the σ -model is equal to the expression in the z -model. As explained in Chapter 1, accurate discretisation of the horizontal viscosity term is of minor importance in shallow-water models. The variation of the eddy viscosity is therefore not taken into account in the discretisation of the horizontal viscosity term. Using the incompressibility property of the fluid, the resulting horizontal viscosity term in the Cartesian- and σ -model is given by:

$$\frac{\partial \tau_{xx}^*}{\partial x^*} + \frac{\partial \tau_{xy}^*}{\partial x^*} = \nu_t^h \left(\frac{\partial^2 u^*}{\partial x^{*2}} + \frac{\partial^2 u^*}{\partial y^{*2}} \right). \quad (2.23)$$

Sometimes a more accurate estimate of the horizontal stress terms may be required. In these situations a more extensive expression for the Reynolds stress tensor is applied together with an alternative turbulence model. This is addressed in the next chapter.

The transformed transport equation is very similar to the Cartesian expression and is given by

$$\begin{aligned} \frac{\partial Hc^*}{\partial t^*} + \frac{\partial Hu^*c^*}{\partial x^*} + \frac{\partial Hv^*c^*}{\partial y^*} + \frac{\partial \omega c^*}{\partial \sigma} = \\ \frac{\partial}{\partial x^*} \left(HD_t^h \frac{\partial c^*}{\partial x^*} \right) + \frac{\partial}{\partial y^*} \left(HD_t^h \frac{\partial c^*}{\partial y^*} \right) + \frac{\partial}{\partial \sigma} \left(D_t^v \frac{\partial c^*}{\partial \sigma} \right) + s. \end{aligned} \quad (2.24)$$

2.3 Turbulence closure

2.3.1 Eddy viscosity concept

Free surface flows occurring in civil engineering practice take place at high Reynolds numbers, often exceeding 10^7 , and as a consequence they are turbulent. The size of the largest eddies, which are associated with the lowest frequencies, are of the order of the flow domain while the smallest eddies, the Kolmogorov microscale η , are several orders of magnitude smaller for Reynolds numbers typical for free surface flows. Since the ratio of the macro scale of the flow \mathcal{L} to the micro scale of the flow η scales as $\eta/\mathcal{L} \sim Re^{-3/4}$, where $Re = \mathcal{L}\mathcal{U}/\nu$ with \mathcal{U} being a characteristic turbulent velocity, it is presently impossible to use Direct Numerical Simulations or even Large Eddy Simulations for the computation of the flow in coastal regions. Therefore it is necessary to model the effects of the turbulence on the mean flow by a turbulence model instead of resolving the dynamics of the turbulent eddies themselves. Moreover, for large-scale applications it is usually sufficient to consider time-averaged effects. This recognition means that the flow predictions are based on time-averaged properties of the turbulence. Since these vary much more gradually in space than the instantaneous turbulence properties, no excessively fine grid is needed.

To model the effects of turbulence, variables are decomposed into a mean value and a fluctuating part as proposed by Osborne Reynolds (Reynolds, 1895):

$$U_i = u_i + u'_i, \quad (2.25)$$

where u_i is an averaged velocity and u'_i is the fluctuating part of the velocity component U_i . The equations of motion are averaged over a time interval large compared to the turbulence time scale but small compared to the typical time scale of the large-scale flow, such as the tidal period, for example. Owing to the non-linearity of the Navier-Stokes equation and the transport equation, the Reynolds averaging process has introduced unknown correlations between fluctuating velocity components and between scalar fluctuations. Physically these correlations, when multiplied by the density ρ , represent transfer of momentum and heat or mass due to the fluctuating turbulent motion. The velocity correlations appear to act as stresses on the fluid and are therefore known as Reynolds stresses while the velocity-scalar correlations represent turbulent heat or mass fluxes. Except for the viscous sublayer near the wall which is not resolved in numerical models for free surface flow, the turbulent stresses/fluxes are much larger than the viscous stresses/fluxes and the latter are therefore usually neglected.

With these Reynolds stresses, $\tau_{ij} = -\rho \overline{u'_i u'_j}$, the well-known closure problem arises which can be solved, in analogy with the viscous stresses in laminar flow, by using the eddy viscosity concept or Boussinesq hypothesis (Boussinesq, 1877). By doing so, the eddy viscosity is proportional to the ratio of the Reynolds stresses and the mean velocity gradients, hence the eddy viscosity is determined by a turbulence quantity and a mean-flow

quantity:

$$\tau_{ij} = -2\rho\nu_t S_{ij} - \frac{2}{3}k\delta_{ij}, \quad (2.26)$$

where

$$S_{ij} = \frac{1}{2} \left(\frac{\partial u_i}{\partial x_j} + \frac{\partial u_j}{\partial x_i} \right), \quad (2.27)$$

is the deformation tensor of the mean flow field, ν_t is the eddy viscosity and k is the turbulent kinetic energy per unit mass (TKE) defined as $k = \frac{1}{2}\overline{u_i^2}$. The second term in eq. (2.26) is needed to obtain the proper trace of τ_{ij} but is generally neglected in large-scale numerical models. On dimensional grounds, the eddy viscosity is proportional to a turbulent velocity scale U and a turbulent length scale of the energy containing eddies \mathcal{L} , i.e. the eddies that contribute most to the turbulent stresses:

$$\nu_t \sim U\mathcal{L}. \quad (2.28)$$

By using the eddy viscosity concept the closure problem has shifted from specifying the Reynolds stresses to specifying the eddy viscosity. However, the characteristic length scale and velocity scale are easier to estimate than the Reynolds stress itself. The eddy viscosity as defined by eq. (2.26) is related to a single length scale and therefore the turbulence models that use such an eddy viscosity are indicated by single-length-scale turbulence models.

In order for the Boussinesq hypothesis to be physically valid, the length scale of the turbulent eddies must be small compared to the geometric length scale. The fact that the largest eddies are of the order of the water depth explains the occasional criticism against the use of this eddy viscosity concept. Moreover, counter-gradient transport of turbulence may take place which is in contrast with the gradient transport assumption (Rodi, 1987). Since it is expected that large Reynolds stresses are generally associated with large velocity gradients, the ratio of a given Reynolds stress to the mean rate of strain, the eddy viscosity, ~~is likely to vary more slowly or more simply than the Reynolds stress itself.~~ Therefore empirical correlations of eddy viscosity are likely to be more accurate than direct empirical correlations of Reynolds stresses, which is the justification for using the eddy viscosity.

2.3.2 Single-length-scale turbulence models

Various turbulence models, based on the eddy viscosity assumption, have been proposed in the literature. Most of these models are based on the assumption that the turbulence is isotropic and therefore the eddy viscosity has no directional dependence, hence the eddy viscosity is a scalar ⁵. The turbulence models based on the scalar eddy viscosity concept

⁵Note that the use of an isotropic eddy viscosity does not necessarily imply isotropy of Reynolds stresses

assume that the state of the turbulence can be characterised by one velocity scale and that the individual Reynolds stresses can be related to this scale. These models vary from algebraic zero-equation models to two-equations models consisting of transport equations for the turbulent quantities. A wide range of turbulence models exists. For an extensive review of the different turbulence models the reader is referred to Rodi (1980), IAHR (1988) and Wilcox (1993).

The linear stress-strain relationship can be inadequate sometimes and the use of an eddy viscosity then becomes debatable. Many attempts have been reported to overcome the shortcomings of this linear eddy viscosity relationship. However, these models are either designed for specific flow conditions and thus lack universality, have been tested too little or are too expensive to apply to free surface flows. Moreover, in regions where the length-scale determining equation is responsible for the poor performance, these more sophisticated models are not likely to be superior. Attention is therefore restricted to turbulence models that are based on the linear eddy viscosity concept. The latter models have been used many times in calculating free surface flows and have proven to work reasonably well under various conditions. One of the simplest models to specify the value of the eddy viscosity ν_t at various regions of the flow is the mixing length model starting from the kinetic theory of gases, as proposed by Prandtl (1925). This model assumes that turbulent kinetic energy is dissipated by viscous action at the point where it is generated by shear. This means that there is no transport of turbulence (no history effects) and hence the turbulence is in local equilibrium. Considering only shear layers with one significant velocity gradient, Prandtl postulated the eddy viscosity $\nu_t = l_m^2 du/dz$ with l_m being the mixing length, which is a characteristic length involved in momentum and scalar exchange. The mixing length has to be prescribed in some way.

In the case of stable stratification, buoyancy forces can have a strong damping effect on the vertical turbulent transport of momentum, heat and mass. Due to the density difference the turbulence is suppressed and to account for this effect, the mixing length has to be corrected. This is usually done by introducing damping functions that use a Richardson number correction ($Ri = -g/\rho\partial\rho/\partial z/(\partial u/\partial z)^2$, e.g. (Simonin *et al.*, 1989). Another possibility is to adjust the eddy viscosity/diffusivity itself, as suggested in Munk & Andersen (1948) and Officer (1976), for example. It is noted that the use of damping functions may give rise to instabilities, as pointed out by Kranenburg (1982).

The mixing-length model has mainly been applied to two-dimensional shear layer flows with only one dominant velocity gradient. In more general flows, the viscosity should be related to the velocity gradients in all directions Rodi (1980), but it is then (almost) impossible to specify the mixing length distribution in space. Besides this, calculations have shown that the mixing-length is problem dependent and thus lacks universality. Other problems arise because the eddy viscosity and diffusivity vanish when the mean velocity gradient is zero.

To overcome the limitations of the mixing-length hypothesis, turbulence models have been developed which account for the transport or history effects of turbulence quantities.

These models generally consist of an equation describing the transport of k . An exact transport equation for the turbulent kinetic energy can be derived from the Navier-Stokes equation, see Tennekes & Lumley (1972), for example. This equation, however, contains higher order correlations which have to be modelled. More specifically, the production term, the diffusion term and the dissipation term need to be modelled. The Boussinesq approximation is used for the production term and gradient transport is assumed for the diffusion term. The turbulent transport terms are usually small enough, compared to the source terms, which means that the possible inaccuracy of using the gradient diffusion assumption in the modelled k -equation is not of major importance. The eddy viscosity is deduced from k by

$$\nu_i^v \sim \mathcal{U}\mathcal{L} \sim \sqrt{k}\mathcal{L}, \quad \nu_i^v = c'_\mu \sqrt{k}\mathcal{L}, \quad (2.29)$$

where c'_μ is an empirical coefficient. Eq. (2.29) is known as the Kolmogorov-Prandtl expression. In the turbulence models that are used most frequently for free surface flows, *i.e.* the k - ε turbulence model (Launder & Spalding, 1972) and the Mellor and Yamada level $2\frac{1}{2}$ model (Mellor & Yamada, 1982), the length scale is computed by solving an extra transport equation. In the case of the k - ε model, this equation does not have a length scale as a dependent variable but represents the rate of dissipation of turbulent kinetic energy, ε . The eddy viscosity that follows from the standard k - ε model, is valid only for high Reynolds numbers. At high Reynolds numbers local isotropy prevails and the rate of dissipation is equal to the kinematic viscosity times the fluctuating vorticity Tennekes & Lumley (1972). An exact equation for the fluctuating vorticity, and therefore for the rate of dissipation, can be derived. This equation is much more complicated than the k -equation and little data is available to substantiate the modelling of the higher order correlations that are used in the standard k - ε model. Wilcox (1993) therefore states that the "drastic surgery approach" for modelling the complex terms in the ε -equation, is not more rigorous than using dimensional-analysis arguments. Adjustments to the standard k - ε model have been proposed to make it suitable for low Reynolds numbers, *e.g.* (Jones & Launder, 1972), although these models are not of any relevance for large-scale free surface flows.

Mellor and Yamada (1982) criticise the use of the ε -equation since it is a quantity describing the small-scale turbulence and not the large-scale turbulence on which the k -equation is based. However, by assuming a spectral equilibrium, ε is the rate of transfer of energy passed down from the larger scales to the small-scale dissipative motion. Hence, even though dissipation takes place at the smallest eddies, ε is governed by the large-scale motion characterised by k and \mathcal{L} . Instead of the rate of dissipation they prefer $k\mathcal{L}$ as a variable as the second equation. It is noted that the ε - and $k\mathcal{L}$ - equations are based on dimensional grounds and therefore other variables can be used for the second length-scale determining equation.

2.3.3 Single-length-scale k - ε model

The single-length-scale 3D k - ε turbulence model used in the numerical model, determines the eddy viscosity ν_t^v related to the small-scale, mostly bottom friction induced turbulence. The characteristic turbulent length scale is determined from

$$\mathcal{L} \sim \frac{k^{3/2}}{\varepsilon}, \quad \mathcal{L} = c_D \frac{k^{3/2}}{\varepsilon}. \quad (2.30)$$

Using eq. (2.29) this yields

$$\nu_t^v = c'_\mu c_D \frac{k^2}{\varepsilon} = c_\mu \frac{k^2}{\varepsilon}, \quad (2.31)$$

where c_D and c_μ are model coefficients.

The k - and ε equations differ somewhat from the standard k - ε model (Launder & Spalding, 1972) and are given by:

$$\frac{Dk}{Dt} = \frac{\partial}{\partial z} \left(\nu_t^v \frac{\partial k}{\sigma_k \partial z} \right) + P_k + B_k - \varepsilon, \quad (2.32a)$$

$$\frac{D\varepsilon}{Dt} = \frac{\partial}{\partial z} \left(\frac{\nu_t^v}{\sigma_\varepsilon} \frac{\partial \varepsilon}{\partial z} \right) + P_\varepsilon + B_\varepsilon - c_{2\varepsilon} \frac{\varepsilon^2}{k}, \quad (2.32b)$$

where c_ε , c_k and $c_{2\varepsilon}$ are model coefficients, $P_{k/\varepsilon}$ is the production term, $B_{k/\varepsilon}$ is the buoyancy term and the last term in eq. (2.32a) and (2.32b) is the dissipation term. In contrast with the standard k - ε model in which the production term is proportional to S_{ij}^2 , in the present model the production term contains vertical velocity gradients only

$$P_k = \nu_t^v \left[\left(\frac{\partial u}{\partial z} \right)^2 + \left(\frac{\partial v}{\partial z} \right)^2 \right], \quad (2.33a)$$

$$P_\varepsilon = c_{1\varepsilon} \frac{\varepsilon}{k} P_k, \quad (2.33b)$$

where $c_{1\varepsilon}$ is a model coefficient.

In chapter 4 the single-length-scale k - ε turbulence model is applied for two situations in which horizontal velocity gradients contribute significantly to the total TKE budget. For these applications the horizontal velocity gradients are included in the production term:

$$P_k = \nu_t^v \left[\left(\frac{\partial u}{\partial z} \right)^2 + \left(\frac{\partial v}{\partial z} \right)^2 + \left(\frac{\partial u}{\partial y} + \frac{\partial v}{\partial x} \right)^2 + 2 \left(\frac{\partial u}{\partial x} \right)^2 + 2 \left(\frac{\partial v}{\partial y} \right)^2 \right]. \quad (2.34)$$

This expression is used for comparison with the two-length-scale k - ε turbulence model, to be presented in section 3.3, only. In the remainder of the applications eq. 2.33a is used.

Note that the terms that contain the vertical velocity w are omitted in agreement with the hydrostatic pressure assumption.

Further simplifications of the standard k - ε turbulence model concern the neglect of the horizontal diffusion terms. In the problems encountered in shallow-water flows, the horizontal length scales are generally much larger than the vertical length scales. Therefore it is important to discretise accurately in the vertical direction, and horizontal gradients in the production term can be neglected (Van Kester, 1994). Although this reasoning does not hold for applications with sufficient resolution in the horizontal direction, the diffusion terms are not included for the simulation of the small-scale flows presented in chapter 4. It is assumed that the horizontal diffusion term is of minor importance compared to the production and advection terms.

For the small-scale turbulence, the production terms, the buoyancy terms and the dissipation terms are the dominating terms in the k - and ε -equations, hence conservation properties are not of great importance for the small-scale turbulence. As a consequence, non-conservative first order upwind discretisation can be applied for the advective terms which guarantees positive solutions. Due to the related numerical diffusion, horizontal diffusion can be neglected.

The buoyancy term is given by

$$B_k = \frac{\nu_t^v g \partial \rho}{\sigma_t \rho \partial z}, \quad (2.35a)$$

$$B_\varepsilon = c_{1\varepsilon} \frac{\varepsilon}{k} (1 - c_{3\varepsilon}) B_k, \quad (2.35b)$$

where $-g/\rho \partial \rho/\partial z = N^2$ is the Brunt-Väisälä frequency and $c_{3\varepsilon}$ is a model coefficient. The model coefficients are taken constant as proposed by Launder and Spalding (1974)

$$\begin{aligned} c_\mu = 0.09, \quad c_k = 1.0, \quad c_\varepsilon = 1.3, \quad c_{1\varepsilon} = 1.44, \quad c_{2\varepsilon} = 1.92, \\ c_{3\varepsilon} = 0 \text{ (unstably stratified)}, \quad c_{3\varepsilon} = 1 \text{ (stably stratified)}. \end{aligned} \quad (2.36)$$

The model coefficients appearing in the k - ε model are derived from experiments on grid turbulence and local equilibrium shear layers (Launder & Spalding, 1972). In decaying grid turbulence, the diffusion and production terms are zero and $c_{2\varepsilon}$ can therefore be directly determined from measurements. The constant c_μ is determined from local equilibrium shear layers where the production equals the dissipation. This leads to $c_\mu = (\overline{u'w'}/k)^2$ which ratio was found to be equal to 0.09. Near solid walls a logarithmic velocity profile prevails and the production is approximately equal to the dissipation and advection can be neglected. Assuming c_ε and c_k to be close to unity (which values were found from model optimisation), the coefficient $c_{1\varepsilon}$ can be found to be equal to $c_{1\varepsilon} = c_{2\varepsilon} - \kappa^2/(\sigma_\varepsilon \sqrt{c_\mu})$. Here, κ is the Von Kármán constant. The values of these constants are well established and seem to work well in many different flow situations. However, the values of $c_{3\varepsilon}$, c_μ and

the Prandtl-Schmidt number $\sigma_{k/\varepsilon}$ are taken to be a function of the stratification in some models reported in the literature. Under stratified and local equilibrium conditions c_μ is dependent upon a Richardson number (Rodi, 1985). Several values have been proposed for the coefficient $c_{3\varepsilon}$ as well. In Rodi (1985), values of $c_{3\varepsilon}$ are proposed that range from 0 for unstable stratification and 0.8-1.0 for stable stratification. In Uittenbogaard *et al.* (1992) it is argued that the effect of density difference is not felt at small scales where the TKE is damped by viscous stresses, *i.e.* they do not restrict ε , leading to a value of $c_{3\varepsilon}$ of 1 and 0 for stable and unstable flow, respectively.

2.4 Boundary and initial conditions

In order to get a well-posed problem, boundary conditions for the momentum equation and the transport equations (for dissolved matter and turbulent quantities) have to be specified. For the momentum equations we impose perfect slip conditions and zero flow through a closed boundary:

$$\frac{\partial u_{\parallel}}{\partial n} = 0, \quad (2.37a)$$

$$u_n = 0, \quad (2.37b)$$

where $\partial/\partial n$ denotes the derivative normal to the boundary and u_{\parallel} is the velocity parallel to the closed boundary. At the open boundaries, generally Dirichlet conditions for velocity and free surface elevation are imposed:

$$u = u(t), \quad (2.38a)$$

$$\zeta = \zeta(t). \quad (2.38b)$$

An extensive description of open boundary conditions for the shallow-water equations, including weakly reflective boundary conditions, can be found in Stelling (1983), for example.

For the transport of dissolved matter Dirichlet boundary conditions are imposed at open boundaries and zero fluxes at closed boundaries.

$$c = c(t), \quad (2.39a)$$

$$\frac{\partial c}{\partial n} = 0. \quad (2.39b)$$

In the 3D turbulence model, values for k and ε at the open boundaries are obtained from solving a reduced k - ε model. Horizontal transport terms of eq. (2.32) are neglected to obtain a one-dimensional turbulence model:

$$\frac{\partial k}{\partial t} = \frac{\partial}{\partial z} \left(D_v \frac{\partial k}{\partial z} \right) + \nu_t^v \left(\frac{\partial u}{\partial z} \right)^2 + \frac{\nu_t^v g}{\sigma_t \rho} \frac{\partial \rho}{\partial z} - \varepsilon, \quad (2.40a)$$

$$\frac{\partial \varepsilon}{\partial t} = \frac{\partial}{\partial z} \left(D_v \frac{\partial \varepsilon}{\partial z} \right) + c_{1\varepsilon} \frac{\varepsilon}{k} \left[\nu_t^v \left(\frac{\partial u}{\partial z} \right)^2 + (1 - c_{3\varepsilon}) \frac{\nu_t^v g \partial \rho}{\sigma_t \rho \partial z} \right] - c_{2\varepsilon} \frac{\varepsilon^2}{k}, \quad (2.40b)$$

where D_v is the vertical eddy viscosity.

At closed boundaries, the so-called law of the wall is used for the 3D model. In this region advection, pressure gradient and molecular diffusion can be neglected, yielding a constant Reynolds shear stress. In this log-layer, where production of TKE equals the dissipation of TKE, k and ε read

$$k = \frac{u_*^2}{\sqrt{c_\mu}}, \quad (2.41a)$$

$$\varepsilon = \frac{u_*^3}{\kappa y}, \quad (2.41b)$$

where y is a coordinate normal to the wall.

The initial conditions in the k - ε model were chosen such that realistic values for the turbulent kinetic energy and eddy viscosity are obtained for the problems considered. The values for the turbulent quantities therefore depend on the approximate mean flow velocities and are constant throughout the computational domain.

2.5 Time integration and spatial discretisation

The numerical models described in the following are based on the Delft3D-flow model of Delft Hydraulics (Delft Hydraulics, 1999), which makes use of the σ -transformation. Our primary interest is the intercomparison of the σ -model and the z -model, which employ identical numerical techniques. The formal accuracy of the numerical methods is therefore believed to be of minor importance. To inhibit excessively large turn-around times for the test cases presented later in this thesis, simplifications are made with respect to the time integration technique and the spatial discretisations of the standard Delft3D-flow model. This has led to a speed up of the model by approximately a factor four.

For the time integration and spatial discretisation standard numerical techniques are used that can be found in many text books, *e.g.* (Vreugdenhil, 1994). However, some details of the implementation of the equations need special attention to ensure optimal performance of the models. These aspects are related to the inherent disadvantages of the z -coordinate system and the σ -coordinate system mentioned and are mentioned in the first chapter of this thesis. In the application of the models it will be shown that these aforementioned features may have a large impact on the results obtained. Reducing the errors related to these is therefore a prerequisite to make a sound comparison between the two models possible for different situations.

2.5.1 Definition of the vertical coordinate systems

The vertical transformed σ -coordinate, first introduced by Philips (1957), is defined in this thesis as (Delft Hydraulics, 1999)

$$\sigma = \frac{z - \zeta}{H}, \quad (2.42)$$

where $H = \zeta + d$. Due to the σ -transformation, the number of nodes in the vertical is constant over the entire computational domain which permits an efficient use of computer resources. The relative thickness does not depend on the horizontal coordinates x and y which gives rise to unnecessarily high grid resolution in shallow areas and possibly insufficient grid resolution in deeper parts of the computational domain. The vertical grid spacing Δz is a function of the water depth H

$$\Delta z_{i,j,k}^n = H_{i,j}^n (\sigma_{k-1/2} - \sigma_{k+1/2}). \quad (2.43)$$

Here i, j, k represent the discrete coordinates in x -, y - and z -direction on the staggered Arakawa C-grid (see Figure 2.1), respectively, and the superscript n denotes the time level.

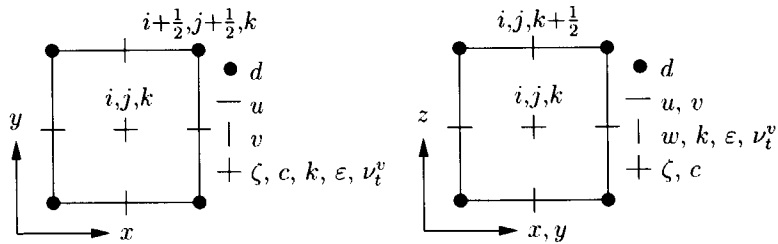


Figure 2.1: Definition of the staggered C-grid

The z -coordinate grid is not boundary fitted in vertical direction and therefore the number of grid cells in vertical direction varies in space and time, see Figure 2.2. Hence, the values of $kmin$ and $kmax$ are not constant. The vertical grid spacing is dependent on the local water depth $d_{i,j}$, the free surface elevation $\zeta_{i,j}$ and the position of the fixed layers z_k :

$$\Delta z_{i,j,k}^n = \min(\zeta_{i,j}^n, z_k) - \max(-d_{i,j}, z_{k-1}), \quad (2.44)$$

where z_k are fixed layers defined by the user. Note that the free surface is not restricted to the uppermost grid cell and variable grid spacing near the bed is taken into account. With

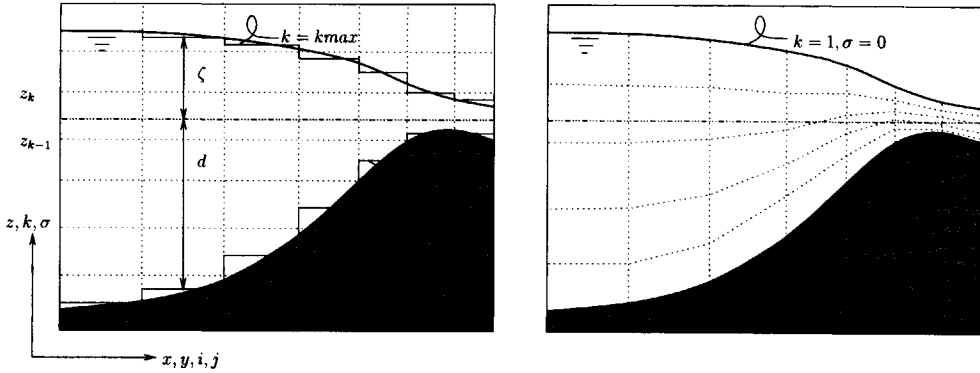


Figure 2.2: Grid definition using the z -coordinate and σ -coordinate, respectively. Variables are placed on a staggered C-grid, see Figure 2.1. Note that the index of the vertical direction k runs in the opposite direction in the z -model and the σ -model.

the exception of the lowest grid cell with index $kmin$, a computational cell is activated whenever $\Delta z_{i,j,k}^n > 0$.

Due to definition (2.44), the free surface and the bottom are discretised as a staircase of alternating horizontal and vertical surfaces. This does not hold for the lowest grid cell near the bottom (see below). Because of the grid structure, the models based on the z -coordinate are more cumbersome to implement than σ -coordinate models. Moreover, in practical situations this vertical discretisation may lead to a number of inactive grid cells which increases the computer memory requirements.

2.5.2 Flooding and drying

Shallow parts of estuaries are subject to drying and flooding during subsequent stages of a tidal cycle. By ensuring positive water depths numerical problems related to the drying and flooding can be avoided (Stelling *et al.*, 1998). This positivity is obtained by using an upwind procedure for the water depth in a velocity point (u or v). The water depth in a velocity point is obtained from:

$$H_{i+1/2,j} = \zeta^+ + d^+, \quad (2.45)$$

where

$$\zeta^+ = \begin{cases} \zeta_{i,j}^n & \text{if } \bar{u}_{i+1/2,j} \geq 0 \\ \zeta_{i+1,j}^n & \text{if } \bar{u}_{i+1/2,j} < 0, \end{cases} \quad (2.46)$$

and

$$d^+ = \frac{d_{i+1/2,j+1/2} + d_{i+1/2,j-1/2}}{2}, \quad (2.47)$$

where \bar{u} is the depth-averaged velocity. The depth in a v -point is computed by replacing the subscript i by j and u by v in the above formulae. The drying of a vertical water column in shallow areas is controlled by a threshold parameter δ . If the water depth $H_{i+1/2,j} < \delta$, all grid cells in a column at position i, j are excluded from the computation. To inhibit repeated changes of state in small time intervals a cell is only included in the computation whenever $H_{i+1/2,j} > 2\delta$. A recent review on different numerical methods for wetting and drying is given in Balzano (1998).

2.5.3 Horizontal gradients in σ -coordinates

The approximation of horizontal gradients in σ -coordinates may give rise to inaccuracies. Due to this transformation horizontal gradients are expressed as the sum of two terms which may be relatively large near steep topography and may be opposite of sign. Small truncation errors in the approximation of both terms may result in a large error in the total horizontal derivative. This error is only due to the horizontal pressure gradient and the horizontal diffusive fluxes. The approximation of the advective fluxes does not introduce large truncation errors since horizontal velocities remain strictly horizontal. Furthermore, the simplification of the horizontal viscous terms (see section 2.2) leads to an expression that consists of one term only.

Assuming a horizontally homogeneous scalar field, $c=c(z)$, Mellor *et al.* (1994) derived an expression for the error E in determining the horizontal gradient of a scalar quantity

$$E\left(\frac{\partial c}{\partial x}\right) = \frac{H}{4} \frac{\partial H}{\partial x^*} \left[(\Delta\sigma)^2 - \sigma^2 \left(\frac{\Delta H}{H}\right)^2 \right] \cdot \left[\left(\frac{\partial^2 c}{\partial z^2}\right) + \frac{\sigma H}{3} \left(\frac{\partial c}{\partial z^3}\right) + \dots \right]. \quad (2.48)$$

Expression (2.48) is the local truncation of the horizontal scalar gradient at a certain grid point. In the case of the horizontal pressure gradient the total error at this point is a summation of the local errors from the surface to this point. The above error can be reduced by subtracting a reference state scalar field before computing the horizontal gradients (Gary, 1973). However, this may be of little help in large areas where the value of the scalar can deviate significantly from the reference state.

Kliem & Pietrzak (1999) note that the error (2.48) vanishes if the condition $(\Delta\sigma)^2 = \sigma^2(\Delta H/H)^2$, which is the limiting value of the hydrostatic consistency condition. This relationship is given by (Janjić, 1977; Mesinger, 1982; Haney, 1991)

$$\left| \frac{\sigma}{H} \frac{\partial H}{\partial x} \right| \Delta x < \Delta\sigma. \quad (2.49)$$

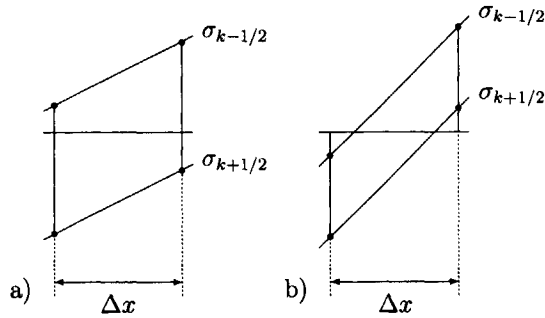


Figure 2.3: Hydrostatic consistent a) and inconsistent b) evaluation of horizontal gradients in the case of a staggered grid.

This condition guarantees that the σ -surface immediately below (above) a given σ -surface remains below (above) the given σ -surface within a horizontal distance of one grid cell, as shown in Figure 2.3. If this condition is not satisfied, the numerical scheme may be non-convergent.

A remedy to minimise the errors in computing horizontal gradients is presented in Stelling & Van Kester (1994). In their paper a finite volume method is presented in which the horizontal diffusive fluxes in the transport equation and baroclinic pressure gradients in the momentum equation are determined in Cartesian coordinates by rotating finite volumes to become rectangular, see Figure 2.4. By doing so, the hydrostatic consistency condition does not have to be satisfied. This is a positive property of this method, especially when areas with rapidly varying bathymetry are considered.

Since the rectangular boxes are not nicely connected to their neighbours, a vertical interpolation of scalars is needed to compute strictly horizontal derivatives. The values obtained from this linear interpolation are indicated by c_1 and c_2 in Figure 2.4. Using the auxiliary variables c_1 and c_2 , two strictly horizontal gradients can be computed

$$\nabla_1 = \frac{c_2 - c_1}{\Delta x_{i+1/2,j}}, \quad (2.50a)$$

$$\nabla_2 = \frac{c_2 - c_1}{\Delta x_{i+1/2,j}}. \quad (2.50b)$$

A non-linear filter is applied to the two consistent gradients. The filter proposed by Stelling & Van Kester (1994) is similar to the well-known MINMOD-limiter. The non-linear filter ∇_m can be written in pseudo code as

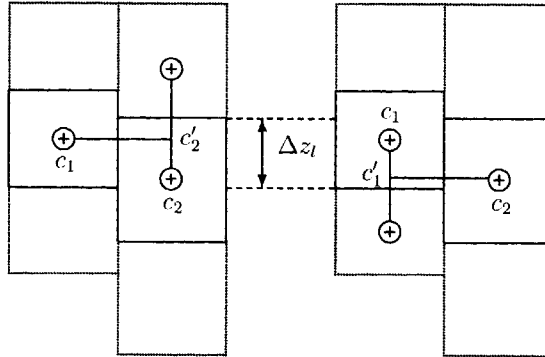


Figure 2.4: Cartesian control volumes, constructed on the basis of the σ -grid, that are used to compute horizontal gradients. The computed gradient acts over a distance Δz_l in the pressure gradient term in the momentum equation and in the horizontal diffusion term in the transport equation. Reproduced from (Stelling & Van Kester, 1994).

```

if  $\nabla_1 * \nabla_2 < 0$  then
   $\nabla_m = 0$ 
else
  if  $\nabla_1 < 0$  then
     $\nabla_m = \max(\nabla_1, \nabla_2)$ 
  else
     $\nabla_m = \min(\nabla_1, \nabla_2)$ 
  endif
endif

```

In the approximation of the horizontal pressure gradient (see section 2.5.4) the use of a non-linear filter is imperative to suppress artificial vertical mixing. If instead of this non-linear filter some linear interpolation formula is applied, wiggles may occur and a small persistent artificial vertical diffusion will be present (except for linear vertical density distribution). Hence, no steady state situation can be reached and an initially stratified water body eventually becomes fully mixed.

In Slørðal (1997) it is stated that the approximation of the baroclinic pressure gradient by the above method produces errors of the same sign which leads to a systematic underestimation of the horizontal pressure gradients. This underestimation can be ascribed to the non-linear filter. This filter selects the minimum pressure gradient of the two gradients under consideration if these have the same sign and is taken equal to zero otherwise. It is shown in Stelling & Van Kester (1994) that taking the minimum of the gradients is a sufficient condition to guarantee positive solutions. Although this positivity is likely to be

of little relevance for the pressure gradient, it is a necessary property for the diffusion term in the transport equation.

The systematic error due to the underestimation of the horizontal gradients can be reduced by extension of the non-linear filter. An additional gradient ∇_3 is introduced which is defined as

$$\nabla_3 = \frac{c_2 - c_1}{\Delta x_{i+1/2,j}}. \quad (2.51)$$

Since ∇_1 and ∇_2 are at least first order consistent approximations of the horizontal pressure gradient (Stelling & Van Kester, 1994), any strictly horizontal gradient ∇ that satisfies

$$\min(\nabla_1, \nabla_2) < \nabla < \max(\nabla_1, \nabla_2), \quad (2.52)$$

also yields a consistent approximation. Therefore it can be argued that the additional gradient ∇_3 is a consistent approximation if it satisfies condition (2.52). Furthermore, ∇_3 possesses point-to-point transfer properties. For a sufficiently small time step Δt this gradient therefore represents a positive scheme. This means that the following limiter is both consistent and positive:

```

if  $\nabla_1 * \nabla_2 < 0$  then
   $\nabla_m = 0$ 
elseif  $\text{abs}(\nabla_4) < \text{abs}(\nabla_3)$  then
   $\nabla_m = \nabla_4$ 
elseif  $\min(\nabla_1, \nabla_2) < \nabla_3 < \max(\nabla_1, \nabla_2)$  then
   $\nabla_m = \nabla_3$ 
else
  if  $\nabla_1 < 0$  then
     $\nabla_m = \max(\nabla_1, \nabla_2)$ 
  else
     $\nabla_m = \min(\nabla_1, \nabla_2)$ 
  endif
endif

```

where ∇_4 can be any consistent gradient. By introduction of ∇_3 in the procedure, the stringent conditions of the minimum operator can be relaxed somewhat which results in an increase of the average computed pressure gradient. Hence, the above mentioned drawback of the Stelling & Van Kester method can be reduced without losing the positive properties of the original method, *i.e.* positivity and finite vertical diffusion. It is noted that the use of other limiter functions is possible.

Although it can be argued that the error related to the underestimation of the pressure gradient error is reduced from a mathematical point of view, it will be shown in Chapter 5 that the application of the extended filter hardly affects computational results for a practical situation.

2.5.4 Discretisation momentum equation

The momentum equations, eq. (2.8), are solved simultaneously with the depth averaged continuity equation, eq. (2.14). An Alternating Direction Implicit (ADI) method (*e.g.* (Leendertse & Liu, 1975; Stelling, 1983)) is used for the time integration. Using this method a full time step Δt is split into two stages. In each stage, variables in one direction are computed implicitly. In order to avoid severe time-step restrictions related to the propagation of free surface waves, the barotropic forcing is computed implicitly. In semi-discrete form this method reads:

stage 1:

$$\begin{aligned} \frac{\zeta^{n+1/2} - \zeta^n}{\frac{1}{2}\Delta t} + \frac{\partial H^n u^{n+1/2}}{\partial x} + \frac{\partial H^{n-1/2} v^n}{\partial y} &= 0, \\ \frac{u^{n+1/2} - u^n}{\Delta t} + g \frac{\partial \zeta^{n-1/2+\theta}}{\partial x} &= \text{RHS}, \\ v^{n+1/2} &= v^n \end{aligned} \quad (2.53)$$

stage 2:

$$\begin{aligned} \frac{\zeta^{n+1} - \zeta^{n+1/2}}{\frac{1}{2}\Delta t} + \frac{\partial H^n u^{n+1/2}}{\partial x} + \frac{\partial H^{n+1/2} v^{n+1}}{\partial y} &= 0, \\ u^{n+1} &= u^{n+1/2} \\ \frac{v^{n+1} - v^{n+1/2}}{\Delta t} + g \frac{\partial \zeta^{n+\theta}}{\partial y} &= \text{RHS}, \end{aligned} \quad (2.54)$$

where $\zeta^{n+\theta} = (1 - \theta)\zeta^n + \theta\zeta^{n+1}$. In the present model θ is chosen equal to 1. The RHS-term contains the remaining terms of eq. (2.8). In the first half time step, u is computed implicitly by inserting the depth-integrated momentum into the continuity equation. In the second half time step v is computed implicitly. The ADI scheme (2.53)-(2.54) is efficient but only first order accurate in time in contrast with the methods proposed by Leendertse & Liu (1975) and Stelling (1983).

An important difference between the σ -model and the z -model is the treatment of the free surface. In the σ -model the numbers of layers is constant and the vertical excursion of the free surface does not impose additional problems. In the z -model on the other hand, the number of grid cells in vertical direction is not fixed, hence the free surface is allowed to travel through the fixed layers in the z -coordinate system. Besides the complex book-keeping which is involved in this process, other pitfalls arise due to this procedure. Consider, for example, the situation depicted in Figure 2.5. At position i, j the free surface has moved from layer k to layer $k+1$ during the time interval $\tau - \tau + \frac{1}{2}\Delta t$. Obviously, the velocity in the flooded grid cell at $t=\tau$ is equal to zero and should therefore be adjusted to get a realistic velocity profile at $t=\tau + \frac{1}{2}\Delta t$. The value is obtained by making use of the

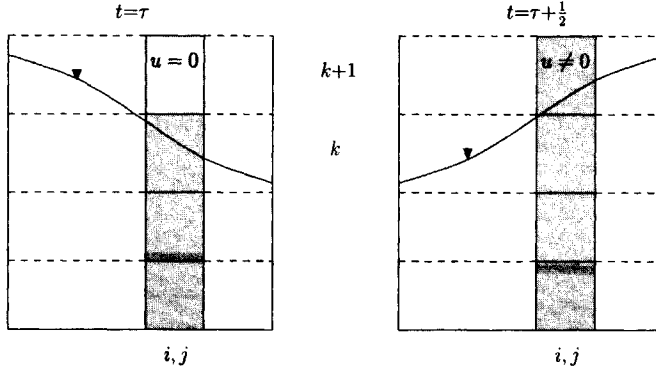


Figure 2.5: Schematic of a flooding grid cell in the z -model at position i, j during time interval $\tau - \tau + \frac{1}{2}\Delta t$ due to variation of the water level.

depth-averaged momentum equation which reads

$$\frac{q_{i+1/2,j,k}^{n+1/2} - q_{i+1/2,j,k}^{n-1/2}}{\frac{1}{2}\Delta t} = -gH_{i+1/2,j}^n \frac{\partial \zeta^{n+1/2}}{\partial x} - \tau_w + \tau_b + \sum_{k=kmin}^{kmax} \text{RHS}_{i+1/2,j,k}^n \Delta z^n, \quad (2.55)$$

where $q_{i+1/2,j,k}^{n+1/2} = \sum_{k=kmin}^{kmax} (u^{n+1/2} \Delta z^n)_{i+1/2,j,k}$ is the depth-integrated discharge per unit width, τ_b is the bottom shear stress, τ_w is the wind shear stress and the right-hand-side contains advection, horizontal diffusion, the baroclinic pressure gradient and the Coriolis term. Note that $kmax$ is not a constant. The new horizontal velocity of the flooded grid cell, $u_{i,j,k+1}^{n+1/2}$, is determined by first setting this velocity equal to the new velocity of the former uppermost grid cell, in this case $u_{i,j,k}^{n+1/2}$. After that, the final velocity of all grid cells at position i, j are corrected by multiplication with a constant factor in order to fulfill eq. (2.55):

$$u_{i+1/2,j,k}^{n+1/2} := \frac{\sum_{k=kmin}^{kmax} (u^{n+1/2} \Delta z^n)_{i+1/2,j,k}}{\sum_{k=kmin}^{kmax} (u^{n+1/2} \Delta z^{n+1/2})_{i+1/2,j,k}} u_{i+1/2,j,k}^{n+1/2}. \quad (2.56)$$

Note that the value of $kmax$ in the numerator and denominator of eq. (2.56) are different in case of flooding and drying cells. A similar procedure must be followed in the case of a drying grid cell. Besides the above, it is important to note that the discharge per unit width $q_{i+1/2,j,k}^{n-1/2}$ in eq. (2.55) is determined on the basis of the water depth H^{n-1} and not on the basis of the water depth $H^{n-1/2}$. The latter is the water depth at the previous ADI stage and is computed simultaneously with the velocity in y -direction, v . If

the former requirements are not met, the z -model exhibits excessive damping. This was clearly demonstrated during the development of the model.

The following sections are focused on the spatial discretisation of the most relevant terms in the momentum equation, the transport equation and the k - ε turbulence model. Discretisation of horizontal derivatives are given in Cartesian coordinates only for the sake of convenience. The full transformed equations can be found in Dunsbergen (1994). We restrict ourselves to the discretisation of the horizontal derivatives in the x -direction since identical discretisations are applied in the y -direction. Unless mentioned otherwise, the discretisation is performed in the z -coordinate system which means that the index k increases in the positive z -direction.

Advection

In order to enhance the efficiency of the numerical model, the horizontal advection is implemented explicitly. By doing so, the implicit coupling of velocity points in the horizontal direction is avoided. This means implicit coupling exists in the vertical direction only (see below) and computational effort to solve the system of equations is reduced significantly. The explicit integration is possible due to the large horizontal grid spacing in shallow-water models. In these models the maximum time step Δt is determined by accuracy rather than by stability in most cases.

A first order upwind method is used that approximates the horizontal advection along a particle's trajectory. In comparison to the standard first order upwind method, the interpolation of variables is performed with much less numerical diffusion than the standard first order upwind method in two-dimensional vertically integrated or three-dimensional applications. For positive u and v , the following is obtained:

$$\begin{aligned}
 u \frac{\partial u}{\partial x} + v \frac{\partial u}{\partial y} \Big|_{i+1/2,j,k} &\approx \frac{u_{i+1/2,j,k}^n}{\Delta x_{i,j}} (u_{i+1/2,j,k}^n - u_{i-1/2,j,k}^n) + \\
 &\quad \frac{\bar{v}}{\Delta y_{i-1/2,j-1/2}} (u_{i-1/2,j,k}^n - u_{i-1/2,j-1,k}^n) \text{ if } \frac{u_{i+1/2,j,k}^n}{\Delta x_{i,j}} > \frac{\bar{v}}{\Delta y_{i-1/2,j-1/2}}, \\
 u \frac{\partial u}{\partial x} + v \frac{\partial u}{\partial y} \Big|_{i+1/2,j,k} &\approx \frac{u_{i+1/2,j,k}^n}{\Delta x_{i,j-1}} (u_{i+1/2,j-1,k}^n - u_{i-1/2,j-1,k}^n) + \\
 &\quad \frac{\bar{v}}{\Delta y_{i+1/2,j-1/2}} (u_{i+1/2,j,k}^n - u_{i+1/2,j-1,k}^n) \text{ if } \frac{u_{i+1/2,j,k}^n}{\Delta x_{i,j-1}} \leq \frac{\bar{v}}{\Delta y_{i+1/2,j-1/2}},
 \end{aligned} \tag{2.57}$$

where $\bar{v} = \frac{1}{4} (v_{i,j+1/2,k}^n + v_{i,j-1/2,k}^n + v_{i+1,j+1/2,k}^n + v_{i+1,j-1/2,k}^n)$. To avoid the creation of an artificial boundary layer in the z -model due to the stair-case representation of the bed, horizontal advection is neglected in the case the flow is directed from the wall (Stelling, 1983). The effect of this measure is demonstrated in section 5.1.4.

In σ -coordinates, the material derivative of the horizontal velocity u becomes

$$\frac{Du}{Dt} = \frac{Du^*}{Dt^*} = \frac{\partial u^*}{\partial t^*} + u^* \frac{\partial u^*}{\partial x^*} + v^* \frac{\partial u^*}{\partial y^*} + \frac{\omega}{H} \frac{\partial u^*}{\partial \sigma}. \quad (2.58)$$

This expression is similar to the Cartesian version, except from the fact that the horizontal derivatives are taken along σ -planes and the vertical velocity w is replaced by the transformed vertical velocity ω . Therefore, in the transformed model the discretisation of the advective terms are comparable to the Cartesian expressions and are therefore not given here.

The vertical transport of horizontal momentum is integrated implicitly to avoid time-step restrictions related to the CFL-stability criterion. Although the vertical velocity is assumed to be small in shallow-water models, locally it may become relatively large due to variations in bathymetry or due to density differences, for example. This is enhanced by using the shallow-water assumption. Under this assumption the vertical velocity is determined by continuity only. Therefore, no work is done by a particle moving in the **vertical direction**, hence vertical excursions are not suppressed by a pressure gradient. Besides this, the grid spacing in the vertical is relatively small and the corresponding CFL-number based on the advective velocity in the vertical direction may therefore be larger than the CFL-number based on the vertical velocity which would require an additional restriction of the time step. For variable vertical grid spacing the central discretisation of vertical transport of horizontal momentum is implemented as

$$w \frac{\partial u}{\partial z} \Big|_{i+1/2,j,k} \approx \bar{w} \left(\frac{\Delta z_-}{\Delta z_+ + \Delta z_-} \frac{u_{i+1/2,j,k+1}^{n+1} - u_{i+1/2,j,k}^{n+1}}{\Delta z_+} + \frac{\Delta z_+}{\Delta z_+ + \Delta z_-} \frac{u_{i+1/2,j,k}^{n+1} - u_{i+1/2,j,k-1}^{n+1}}{\Delta z_-} \right), \quad (2.59)$$

where $\bar{w} = \frac{1}{4}(w_{i,j,k}^n + w_{i+1,j,k}^n + w_{i,j,k-1}^n + w_{i+1,j,k-1}^n)$, $\Delta z_+ = \frac{1}{2}(\Delta z_{i+1/2,j,k+1} + \Delta z_{i+1/2,j,k})$ and $\Delta z_- = \frac{1}{2}(\Delta z_{i+1/2,j,k} + \Delta z_{i+1/2,j,k-1})$. Together with the vertical diffusion term it forms a tridiagonal system which is solved with a double sweep procedure.

Horizontal diffusion

For many applications it is legitimate to assume a constant eddy viscosity because of the relative unimportance of the horizontal viscosity term, see section 2.2. This term then reduces to a Laplace operator with constant coefficient and is given by

$$\nu_t^h \left(\frac{\partial^2 u}{\partial x^2} + \frac{\partial^2 u}{\partial y^2} \right) \Big|_{i+1/2,j,k} \approx \frac{\nu_t^h \Big|_{i+1/2,j,k}}{\Delta x_{i+1/2,j}} \left(\frac{u_{i+1,j,k}^n - u_{i,j,k}^n}{\Delta x_{i+1,j}} - \frac{u_{i,j,k}^n - u_{i-1,j,k}^n}{\Delta x_{i,j}} \right) + \frac{\nu_t^h \Big|_{i+1/2,j,k}}{\Delta y_{i+1/2,j}} \left(\frac{u_{i,j+1,k}^n - u_{i,j,k}^n}{\Delta y_{i+1/2,j+1}} - \frac{u_{i,j,k}^n - u_{i,j-1,k}^n}{\Delta y_{i+1/2,j-1}} \right). \quad (2.60)$$

Note that derivatives in the z -model are strictly horizontal and that derivatives in the σ -model are computed along σ -planes. Similar to the horizontal advection, coupling of velocity points in the horizontal plane is avoided by explicit treatment of the horizontal diffusion term. Again this introduces a stability criterion that has to be fulfilled.

For reasons mentioned in section 2.5.4, vertical diffusion is computed implicitly and central differences are employed for the spatial discretisation:

$$\frac{\partial}{\partial z} \nu_t^v \frac{\partial u}{\partial z} \Big|_{i+1/2,j,k} \approx \frac{\nu_{i+1/2,j,k+1/2}^n}{\Delta z_{i+1/2,j,k}} \frac{u_{i+1/2,j,k+1}^{n+1} - u_{i+1/2,j,k}^{n+1}}{\Delta z_{i+1/2,j,k+1/2}} - \frac{\nu_{i+1/2,j,k-1/2}^n}{\Delta z_{i+1/2,j,k}} \frac{u_{i+1/2,j,k}^{n+1} - u_{i+1/2,j,k-1}^{n+1}}{\Delta z_{i+1/2,j,k-1/2}}. \quad (2.61)$$

The expression for the vertical diffusion term is almost identical to the Cartesian one. Hence, a similar discretisation is implemented in the σ -model and is therefore not repeated here.

Because of the definition of Δz by eq. (2.44), the grid spacing in the z -model may exhibit large variations in the first two cells above the bottom. This can locally give rise to large truncation errors. The effect of this error on the computational results has not been studied in this thesis and no measures were taken to reduce these potential errors in discretising the vertical advection of momentum. However, for the computation of the viscosity term near the bottom, *i.e.* the bottom shear stress, adjustment of the numerical scheme proved to be important as will be discussed in the following section.

Bottom shear stress

The vertical viscosity term at the first computational cell above the bed contains the bottom shear stress boundary condition. Near the bottom the vertical viscosity term reads

$$\nu_t^v \frac{\partial u}{\partial z} \Big|_{z=-d} = \frac{\tau_b}{\rho}. \quad (2.62)$$

The bottom shear stress is defined as

$$\tau_b = \rho u_{*b}^2. \quad (2.63)$$

Assuming a logarithmic velocity profile, the friction velocity near the bottom can be expressed as

$$u_{*b} = u_b \kappa \left(\ln \left(1 + \frac{\frac{1}{2} \Delta z_{kmin}}{z_0} \right) \right)^{-1}. \quad (2.64)$$

Here u_b is the total velocity near the bottom, Δz_{kmin} is the grid spacing near the bottom and z_0 is the roughness height. Hence, the bottom shear stress is computed from

$$\frac{\tau_b}{\rho} = \left(\frac{\kappa}{\ln(z_0^{-1}(z_0 + \frac{1}{2} \Delta z_{kmin}))} \right)^2 \Big| u_{i+1/2,j,kmin}^n \Big| u_{i+1/2,j,kmin}^{n+1}. \quad (2.65)$$

This quadratic expression has been linearised with respect to the time level to make implicit treatment of the bottom friction possible.

Because the vertical grid spacing may vanish in the present z -coordinate model, the bottom shear stress may go to infinity since $z_0^{-1}(z_0 + \frac{1}{2}\Delta z_{kmin}) \rightarrow 1$. These large variations of the bottom shear stress may influence the local flow field and is likely to have a large impact on the sediment transport in morphological studies. To circumvent any problems regarding the bottom shear stress term, several measures can be taken.

The bottom shear stress in the numerical model is based on the assumption of a logarithmic velocity distribution in the vertical direction. Therefore it is in principle possible to compute the bottom shear stress at any height of the water column. Although large deviations from the logarithmic velocity profile may be encountered, it is plausible that the computation of the bottom shear stress between the first and second computational cell above the bottom will hardly damage the results. An alternative measure to bound the variations of the bottom shear stress is to introduce a threshold for the minimum grid spacing near the bottom so that $\Delta z_{kmin} \gg z_0$.

The former adjustment to the computation of the bottom shear stress is applied in the z -model. The variations of the bottom shear stress are suppressed to a large extent by adopting this method. This will be shown in section 5.1.1.

The discretisation of the wind shear stress τ_w is identical to the above and is therefore not repeated. It is noted, however, that no measures need to be taken for computing the wind shear stress since the vertical grid spacing is not involved in computing the wind shear stress τ_w :

$$\tau_w = \rho_{air} C_d U_{10}^2, \quad (2.66)$$

where ρ_{air} is the density of the air, C_d is the drag coefficient and U_{10}^2 is the wind velocity 10 meters above the free surface.

Pressure gradient

The pressure gradient is split into two parts. The barotropic (btr) component related to gradients in the free surface elevation is computed implicitly as shown in eq. (2.53) and (2.54). The baroclinic (bcl) part, related to horizontal density gradients, is computed explicitly.

In the z -model, the discretisation of these terms is straightforward and is given by

$$\frac{\partial p_{btr}}{\partial x} = \rho g \frac{\partial \zeta}{\partial x} \Big|_{i+1/2,j,k} \approx \frac{\rho g}{\Delta x_{i+1/2,j}} (\zeta_{i+1,j}^{n+1} - \zeta_{i,j}^{n+1}), \quad (2.67)$$

$$\frac{\partial p_{bcl}}{\partial x} = g \int_z^\zeta \frac{\partial \rho}{\partial x} dz' \Big|_{i+1/2,j,k} \approx \frac{g}{\Delta x_{i+1/2,j}} \sum_{k'=k}^{kmax} \Delta z_{i+1/2,j,k'} (\rho_{i+1,j,k'}^n - \rho_{i,j,k'}^n). \quad (2.68)$$

In the σ -model on the other hand, extra terms arise due to the transformation. Different expressions can be derived for the horizontal pressure gradient in σ -coordinates, see Appendix B. In the present model the following expression is used

$$\frac{\partial p}{\partial x} = \left(\rho\sigma + \int_{\sigma}^0 \rho d\sigma' \right) g \frac{\partial d}{\partial x} + gH \frac{\partial}{\partial x^*} \int_{\sigma}^0 \rho d\sigma' + \left(\rho(1 + \sigma) + \int_{\sigma}^0 \rho d\sigma' \right) g \frac{\partial \zeta}{\partial x}. \quad (2.69)$$

The barotropic and baroclinic forcing can now be discretised separately:

$$\frac{\partial p_{\text{btr}}}{\partial x} \Big|_{i+1/2,j,k} \approx \frac{g}{\Delta x_{i+1/2,j}} \left(\bar{\rho} + \bar{\rho}\sigma_k + \sum_{k'=1}^k \sigma_{k'} \rho_{k'}^n \Big|_{i+1/2,j,k} \right) \left(\zeta_{i+1,j}^{n+1} - \zeta_{i,j}^{n+1} \right), \quad (2.70)$$

$$\begin{aligned} \frac{\partial p_{\text{bcl}}}{\partial x} \Big|_{i+1/2,j,k} \approx & \frac{g}{\Delta x_{i+1/2,j}} \left[\left(\bar{\rho}\sigma_k + \sum_{k'=1}^k \sigma_{k'} \rho_{k'}^n \Big|_{i+1/2,j,k} \right) (d_{i+1,j} - d_{i,j}) + \right. \\ & \left. H_{i+1/2,j} \left(\sum_{k'=1}^k \sigma_{k'} \rho_{i+1,j,k'}^n - \sum_{k'=1}^k \sigma_{k'} \rho_{i,j,k'}^n \right) \right], \end{aligned} \quad (2.71)$$

where $\bar{\rho} = \frac{1}{2}(\rho_{i+1,j,k}^n + \rho_{i,j,k}^n)$.

As discussed in section 2.5.3, the above discretisation may give rise to large errors in the approximation of the pressure gradient term in regions with steep topography. Therefore the method of Stelling & Van Kester (1994) is implemented in the present code as well, see section 2.5.3. Using this method the pressure gradient may be written as

$$\frac{\partial p}{\partial x} \Big|_{i+1/2,j,k} \approx \frac{\partial p_{\text{bcl}}}{\partial x} \Big|_{i+1/2,j,k-1} + \nabla_m + \rho g \frac{\partial \zeta}{\partial x}, \quad (2.72)$$

where

$$\nabla_m = \max\left(0, \frac{\nabla_1 \cdot \nabla_2}{|\nabla_1 \cdot \nabla_2|}\right) \cdot \min(|\nabla_1|, |\nabla_2|) \cdot \text{sign}(\nabla_1), \quad (2.73)$$

and

$$\nabla_1 = \frac{g}{\Delta x_{i+1/2,j}} \Delta z_i (\rho'_2 - \rho_1), \quad (2.74a)$$

$$\nabla_2 = \frac{g}{\Delta x_{i+1/2,j}} \Delta z_i (\rho_2 - \rho'_1). \quad (2.74b)$$

Here Δz_i is a vertical grid spacing determined by the position of vertical cell faces of the rotated grid cells, see Figure 2.4. This vertical grid spacing is computed by considering an interval

$$\left[\min(-d_i, -d_{i+1}), \max(\zeta_i, \zeta_{i+1}) \right], \quad (2.75)$$

which is divided into $2k_{\max}+1$ subintervals

$$[z_{i+1/2,l}, z_{i+1/2,l+1}], \quad l = 0, \dots, 2k_{\max}, \quad z_0 = \min(-d_i, -d_{i+1}), \quad z_{2k_{\max}+1} = \max(\zeta_i, \zeta_{i+1}). \quad (2.76)$$

For convenience the index j is disregarded in the above equations. This set of points is ordered such that $z_{i+1/2,l+1} > z_{i+1/2,l}$ for $l = 0, \dots, 2k_{\max}+1$. This results from a sort-merge operation of the two sets

$$\zeta_i + \sigma_k H_i | k = 0, \dots, k_{\max}, \quad \zeta_{i+1} + \sigma_k H_{i+1} | k = 0, \dots, k_{\max}, \quad \sigma_{2k_{\max}} = 0, \quad \sigma_0 = -1. \quad (2.77)$$

To each interval $[z_{i+1/2,j}, z_{i+1/2,l+1}]$ one or two adjacent cells are connected with cell-centered concentrations $c_{i,m(l)}$ and $c_{i+1,n(l)}$. Here $m(l)$ and $n(l)$ denote cell numbers. If only one cell is connected to an interval, as might happen near the bottom or the free surface, then the pressure gradient is assumed to be zero.

2.5.5 Discretisation continuity equation

The free surface elevation is computed from the depth integrated continuity equation, eq. (2.12). To avoid severe time step restrictions related to the propagation of long free surface waves the free surface elevation ζ is computed implicitly in both stages of the ADI scheme. By integration of the horizontal momentum equation eq. (2.8) with respect to the depth and inserting the equation thus obtained into the depth-integrated continuity equation, a tridiagonal system is obtained. This system is solved efficiently by using a double sweep algorithm. The discrete continuity equation reads, in absence of sources and sinks, in the first half time step

$$\begin{aligned} \frac{\zeta_{i,j}^{n+1/2} - \zeta_{i,j}^n}{\frac{1}{2}\Delta t} + \frac{\sum_{k=k_{\min}}^{k_{\max}} u_{i+1/2,j,k}^{n+1} \Delta z_{i+1/2,j,k}^n - \sum_{k=k_{\min}}^{k_{\max}} u_{i-1/2,j,k}^{n+1} \Delta z_{i-1/2,j,k}^n}{\Delta x_{i,j}} \\ + \frac{\sum_{k=k_{\min}}^{k_{\max}} v_{i,j+1/2,k}^n \Delta z_{i,j+1/2,k}^n - \sum_{k=k_{\min}}^{k_{\max}} v_{i,j-1/2,k}^n \Delta z_{i,j-1/2,k}^n}{\Delta y_{i,j}} = 0. \end{aligned} \quad (2.78)$$

The discretisation in the second stage is similar to the first stage. The horizontal velocity v is now computed implicitly and u is computed explicitly, see eq. (2.54).

2.5.6 Discretisation transport equation

Accurate treatment of the advection terms and diffusion terms in the transport equation is of major importance for simulating stratified flow. While the momentum equation is mostly dominated by pressure gradients and bottom friction, this is not the case for the transport equation. The accuracy of the computed distribution of scalar quantities is

therefore solely dependent upon the approximation of advective and diffusive processes. Moreover, conservation and positivity are a prerequisite for obtaining physically realistic solutions.

A conservative implementation of these terms is obtained by using a finite volume approach:

$$\frac{(Vc)_{i,j,k}^{n+1/2} - (Vc)_{i,j,k}^n}{\frac{1}{2}\Delta t} = \sum_{l=1}^6 F_l, \quad (2.79)$$

where F_l are the fluxes normal to the cell faces of a grid cell at i, j, k due to advection and diffusion and V is the volume of a grid cell. Although eq. (2.79) is conceptually simple, the implementation of a conservative transport routine for the z -model is much more elaborate than for the σ -model. This is related to the difference of grid definition in both models. The boundary fitted σ -model has a constant number of layers in the vertical. As a consequence the relative positions of the active grid cells with respect to each other do not change in time. Hence, an outgoing flux of a grid cell at i, j, k is discharged into one of its neighbouring grid cells.

In the z -model this is not necessarily the case. Consider the two-dimensional laterally averaged (2DV) situation depicted in Figure 2.6.a. In this figure horizontal gradients in the free surface elevation exist which result in fluxes through the cell face at $x=i$. However, the uppermost grid cell at $x=i$ has no direct neighbouring grid cell. Hence the outgoing flux is discharged in the uppermost cell at $i-1$ and $i+1$. Although the position of the free surface will generally not vary this much within one time-step, this example reveals the potential problems of scalar transport in the z -coordinate model. In order to construct a transport routine for the z -model which is relatively easy to implement and which ensures conservation of matter, the water column is split into a "3D" and a "2D" part. The vertical excursion of the free surface is confined to the 2D part of the water column, see Figure 2.6.b. This region is treated as one grid cell, hence the concentration in this area is assumed to be equal in all grid cells running from $Kmin$ to $Kmax$ and is computed from

$$\sum_{k=Kmin}^{Kmax} (Vc)_{i,j,k}^{n+1/2} - \sum_{k=Kmin}^{Kmax} (Vc)_{i,j,k}^n = \frac{\Delta t}{2} \sum_{k=Kmin}^{Kmax} \sum_{l=1}^6 (F_l)_k, \quad (2.80)$$

where $Kmin = \min(kmax_{i,j}^n, kmax_{i,j}^{n+1})$ and $Kmax = \max(kmax_{i,j}^n, kmax_{i,j}^{n+1})$.

In the 3D part of the water column, which consists of the remainder of the active grid cells at i, j , the concentration is obtained from

$$\frac{(Vc)_{i,j,K}^{n+1/2} - (Vc)_{i,j,K}^n}{\frac{1}{2}\Delta t} = \sum_{l=1}^6 (F_l)_k, \quad k = kmin..Kmin - 1. \quad (2.81)$$

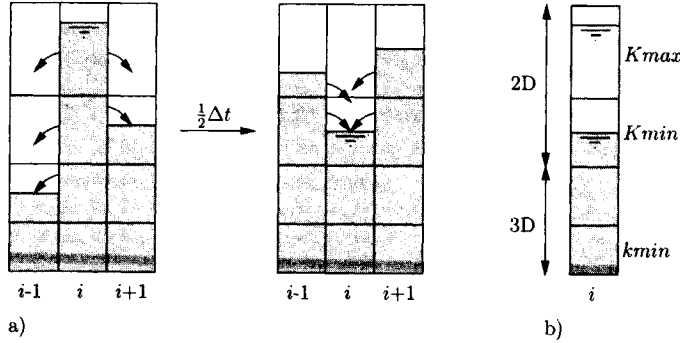


Figure 2.6: Schematic of the transport routine in the z -model. a) Free surface elevation and fluxes at $t=\tau$ and $t=\tau+\frac{1}{2}\Delta t$. b) Division of the water column at position i into a 3D part and a 2D part on the basis of the water level at $t=\tau$ and $t=\tau+\frac{1}{2}\Delta t$.

Advection

Over the last decades, much research has been carried out on the numerical representation of the advection terms arising in the transport equation. Even today approximation of the advective transport is one of the more involved topics in the computational fluid dynamics area. It turns out to be difficult to construct a method that is accurate, monotonic and mass-conserving at the same time. For example the second order central difference scheme exhibits spurious numerical oscillations for a sufficiently large mesh-Péclet number $u\Delta x/\nu_t$, (see *e.g.* (Fletcher, 1991)). These so-called "wiggles" may affect accuracy but also stability. In order to avoid these wiggles, often first order upwind discretisation is used. This method guarantees monotonicity but suffers from severe numerical diffusion.

The use of non-linear advection schemes appears to be necessary to meet the requirements of accuracy and monotonicity, *e.g.* (Hirsch, 1990), (Zijlema, 1996). Among these, the schemes based on the total variation diminishing (TVD) concept (first introduced by (Harten, 1983)) are the most popular. These TVD schemes are obtained by adding a limited anti-diffusive flux, multiplied by the flux limiter, to the first order upwind scheme in such a way as to give non-oscillatory solutions in steep gradient regions without much numerical smearing of sharp gradients. The flux-limiter is a non-linear function of the upwind ratio of consecutive gradients of the solution, assuming $u_{i+1/2} > 0$

$$r_{i+1/2} = \frac{c_i - c_{i-1}}{c_{i+1} - c_i}, \quad (2.82)$$

which leads to the flux-limited scheme

$$c_{i+1/2} = c_i + \frac{1}{2}\Psi(r_{i+1/2})(c_{i+1} - c_i), \quad (2.83)$$

where Ψ is the flux limiting function. For the approximation of the horizontal advective flux the explicit Van Leer II scheme is used. This scheme is found to be TVD, second order accurate (except near extrema) and is easy to implement. Since the advection term in the momentum equations is also integrated explicitly, the explicit treatment of the advective term does not lead to additional time step restrictions. The Van Leer II limiter is given by:

$$\Psi(r_{i+1/2}) = \frac{|r| + r}{1 + r}. \quad (2.84)$$

The resulting flux at the cell face is equal to

$$F_{i+1/2,j,k} = Qc|_{i+1/2,j,k} \approx c_{i+1/2,j,k}^n Q_{i+1/2,j,k}^n, \quad (2.85)$$

where $Q_{i+1/2,j,k} = u_{i+1/2,j,k} \Delta y_{i+1/2,j,k} \Delta z_{i+1/2,j,k}$ is the discharge through the cell-face at $i + 1/2, j, k$. Note that directional splitting is applied in the computation of the advective fluxes in x - and y -direction.

In agreement with the momentum equation, the vertical advection is also computed implicitly in the transport equation. To ensure positive solutions we apply first order upwind discretisation in the vertical direction:

$$\begin{aligned} F_{i,j,k+1/2} &= Qc|_{i,j,k+1/2} \approx Q_{i,j,k+1/2}^{n+1} c_{i,j,k}^{n+1} & \text{if } Q_{i,j,k+1/2}^{n+1} > 0, \\ F_{i,j,k+1/2} &= Qc|_{i,j,k+1/2} \approx Q_{i,j,k+1/2}^{n+1} c_{i,j,k+1}^{n+1} & \text{if } Q_{i,j,k+1/2}^{n+1} \leq 0. \end{aligned} \quad (2.86)$$

Because of the vanishing vertical grid spacing in the σ -model in shallow areas, implicit integration is necessary to avoid severe time-step restrictions. However, in the z -model a lower bound for the vertical grid spacing may be defined which allows us to use an explicit time integration method for the vertical advection terms. Simple implementation of explicit TVD schemes in the vertical is therefore feasible. This is an advantage of the z -model since the performance of a numerical model in stratified environments often depends on the vertical transport schemes adopted in a model. In order to compare results with the σ -model first order discretisation in the z -model is used unless mentioned otherwise.

Diffusion

In correspondence with eq. (2.60), the horizontal diffusion is by default computed along σ -planes in the σ -model. The discretisation of the horizontal diffusion is then similar in the z -model and the σ -model and the diffusive flux through a cell face at $i + 1/2, j, k$ is given by:

$$F_{i+1/2,j,k} = AD_t^h \frac{\partial c}{\partial x} \Big|_{i+1/2,j,k} \approx A_{i+1/2,j,k} D_{i+1/2,j,k}^n \frac{c_{i+1,j,k}^n - c_{i,j,k}^n}{\Delta x_{i+1/2,j}}, \quad (2.87)$$

where $A_{i+1/2,j,k} = \Delta y_{i+1/2,j,k} \Delta z_{i+1/2,j,k}$ is the cell face area. the super- and subscript h and t are omitted for the sake of clarity. In areas with steep bottoms the discretisation along σ -planes leads to artificial vertical upwelling in the σ -model. A method to reduce the related errors is given in 2.5.4 for the pressure gradient and can also be applied to the horizontal diffusion. In (Stelling & Van Kester, 1994) it is noted that this anti-creep approach must be applied to the baroclinic pressure gradient and horizontal diffusion term simultaneously: if the horizontal gradients of the concentration are zero, then there is no contribution of the horizontal density gradients to the driving force in the momentum equation. It is therefore important to have exactly the same mechanism in the numerical approximation. If not, there will always be artificial flow near steep bottom slopes owing to truncation errors. Using the method of Stelling and Van Kester the horizontal diffusive flux at $i + 1/2, j, k$ reads:

$$F_{i+1/2,j,k} = AD_t^h \left. \frac{\partial c}{\partial x} \right|_{i+1/2,j,k} \approx A'_{i+1/2,j,k} \max\left(0, \frac{\nabla_1 \cdot \nabla_2}{|\nabla_1 \cdot \nabla_2|}\right) \cdot \min(|\nabla_1|, |\nabla_2|) \cdot \text{sign}(\nabla_1), \quad (2.88)$$

where ∇_1 and ∇_2 are now defined as

$$\nabla_1 = D_{i+1/2,j,k} \frac{c_2 - c_1}{\Delta x_{i+1/2,j}}, \quad (2.89a)$$

$$\nabla_2 = D_{i+1/2,j,k} \frac{c_2 - c'_1}{\Delta x_{i+1/2,j}}. \quad (2.89b)$$

The cell-face area is now determined by $A'_{i+1/2,j,k} = \Delta y_{i+1/2,j,k} \Delta z_i$, see section 2.5.4. The proposed extension of the limiter given by eq. (2.51) can be applied to the diffusion term in a similar way.

The vertical diffusion is discretised by using an implicit central approximation for the diffusive fluxes:

$$F_{i,j,k+1/2} = AD_t^v \left. \frac{\partial c}{\partial x} \right|_{i,j,k+1/2} \approx A_{i,j,k+1/2} D_{i,j/k+1/2}^n \frac{c_{i,j,k+1}^{n+1} - c_{i,j,k}^{n+1}}{\Delta z_{i,j,k+1/2}}. \quad (2.90)$$

2.5.7 Discretisation standard k - ε turbulence model

The transport equations for k and ε are solved by using a time splitting procedure. First the system of equations is decoupled in the vertical direction by computing the horizontal advection implicitly. This system of equations is solved by a Gauss-Seidel type elimination method. After this, the vertical advection and diffusion are computed implicitly together with the source terms. This leads to a tridiagonal system that is solved by a double sweep method. The semi-discrete equations are given in each step by:

$$\frac{k_{i,j,k+1/2}^* - k_{i,j,k+1/2}^n}{\Delta t} = -u \frac{\partial k^*}{\partial x} - v \frac{\partial k^*}{\partial y}, \quad 1^{\text{st}} \text{ step} \quad (2.91a)$$

$$\frac{k_{i,j,k+1/2}^{n+1} - k_{i,j,k+1/2}^*}{\Delta t} = w \frac{\partial k^{n+1}}{\partial z} + \frac{\partial}{\partial z} D_t^v \frac{\partial k^{n+1}}{\partial z} + P_k + B_k - \varepsilon, \quad 2^{\text{nd}} \text{ step} \quad (2.91b)$$

here k^* is the provisional turbulent kinetic energy. The k - and ε -equation are solved once every full time step Δt .

For the discretisation of the advection terms a non-conservative first order upwind method is used (see section 2.3.3) that guarantees positive solutions, something which is imperative in solving the k - and ε -equations. The variables k and ε are located on the cell face at $i, j, k + 1/2$, see Figure 2.1:

$$\begin{aligned} u \frac{\partial k^*}{\partial x} \Big|_{i,j,k+1/2} &\approx \bar{u} \frac{k_{i,j,k+1/2}^* - k_{i-1,j,k+1/2}^*}{\Delta x_{i,j}} \quad \text{if } \bar{u} > 0, \\ u \frac{\partial k^*}{\partial x} \Big|_{i,j,k+1/2} &\approx \bar{u} \frac{k_{i-1,j,k+1/2}^* - k_{i,j,k+1/2}^*}{\Delta x_{i,j}} \quad \text{if } \bar{u} \leq 0, \end{aligned} \quad (2.92)$$

where $\bar{u} = \frac{1}{4}(u_{i+1/2,j,k}^n + u_{i-1/2,j,k}^n + u_{i+1/2,j,k+1}^n + u_{i-1/2,j,k+1}^n)$, and

$$\begin{aligned} w \frac{\partial k^{n+1}}{\partial z} \Big|_{i,j,k+1/2} &\approx w_{i,j,k+1/2}^n \frac{k_{i,j,k+1/2}^{n+1} - k_{i,j,k-1/2}^{n+1}}{\Delta z_{i,j,k}} \quad \text{if } w_{i,j,k+1/2}^n > 0, \\ w \frac{\partial k^{n+1}}{\partial z} \Big|_{i,j,k+1/2} &\approx w_{i,j,k+1/2}^n \frac{k_{i,j,k+3/2}^{n+1} - k_{i,j,k+1/2}^{n+1}}{\Delta z_{i,j,k+1}} \quad \text{if } w_{i,j,k+1/2}^n \leq 0. \end{aligned} \quad (2.93)$$

The vertical diffusion is discretised by means of second order central differences:

$$\begin{aligned} \frac{\partial}{\partial z} D \frac{\partial k^{n+1}}{\partial z} \Big|_{i,j,k+1/2} &\approx \frac{D_{i,j,k+1}^n}{\Delta z_{i,j,k+1/2}} \frac{k_{i,j,k+3/2}^{n+1} - k_{i,j,k+1/2}^{n+1}}{\Delta z_{i,j,k+1}} - \\ &\quad \frac{D_{i,j,k}^n}{\Delta z_{i,j,k-1/2}} \frac{k_{i,j,k+1/2}^{n+1} - k_{i,j,k-1/2}^{n+1}}{\Delta z_{i,j,k}}. \end{aligned} \quad (2.94)$$

The production term consists of vertical gradients only:

$$\begin{aligned} P_k \Big|_{i,j,k+1/2} &\approx \frac{\nu_t^v}{2} \left[\left(\frac{u_{i+1/2,j,k+1}^{n+1} - u_{i+1/2,j,k}^{n+1}}{\Delta z_{i+1/2,j,k+1/2}} \right)^2 + \left(\frac{u_{i-1/2,j,k+1}^{n+1} - u_{i-1/2,j,k}^{n+1}}{\Delta z_{i-1/2,j,k+1/2}} \right)^2 + \right. \\ &\quad \left. \left(\frac{v_{i,j+1/2,k+1}^{n+1} - v_{i,j+1/2,k}^{n+1}}{\Delta z_{i,j+1/2,k+1/2}} \right)^2 + \left(\frac{v_{i,j-1/2,k+1}^{n+1} - v_{i,j-1/2,k}^{n+1}}{\Delta z_{i,j-1/2,k+1/2}} \right)^2 \right]. \end{aligned} \quad (2.95)$$

The discretisation of the buoyancy term is constructed in such a way that a positive solution is guaranteed:

$$B_k \Big|_{i,j,k+1/2} \approx \frac{\nu_t^v}{\sigma_t} \frac{g}{\rho_{i,j,k}} \frac{\rho_{i,j,k+1}^n - \rho_{i,j,k}^n}{\Delta z_{i,j,k+1/2}}, \quad (2.96a)$$

$$\frac{k_{i,j,k+1/2}^{n+1} - k_{i,j,k+1/2}^*}{\Delta t} + \frac{k_{i,j,k+1/2}^{n+1}}{k_{i,j,k+1/2}^*} \max(0, B_k) + \min(0, B_k) = 0. \quad (2.96b)$$

Note that in eq. (2.96b) only the buoyancy term is taken into consideration. For the discretisation of the dissipation term in the k - and ε -equation, Newton linearisation is applied to ensure positive solutions:

$$\varepsilon \Big|_{i,j,k+1/2} \approx 2 \frac{k_{i,j,k+1/2}^{n+1}}{k_{i,j,k+1/2}^*} \varepsilon_{i,j,k+1/2}^* - \varepsilon_{i,j,k+1/2}^*, \quad (2.97a)$$

$$\frac{\varepsilon^2}{k} \Big|_{i,j,k+1/2} \approx 2c_{2\varepsilon} \frac{\varepsilon_{i,j,k+1/2}^{n+1}}{k_{i,j,k+1/2}^*} \varepsilon_{i,j,k+1/2}^* - c_{2\varepsilon} \frac{(\varepsilon_{i,j,k+1/2}^*)^2}{k_{i,j,k+1/2}^*}. \quad (2.97b)$$

Chapter 3

Two-length-scale k - ε model

In this chapter a new two-length-scale turbulence model is presented that is based on the concept of the standard k - ε turbulence model. This model, which is computationally hardly more expensive than the standard model, takes anisotropy of shallow-water turbulence into account via two separate turbulence models. The small-scale bottom generated turbulence, which is essentially three-dimensional, is modelled by a 3D k - ε model in which the production of turbulent kinetic energy is determined solely by vertical velocity gradients. The larger scale quasi-two-dimensional turbulence is modelled with a depth-averaged k - ε turbulence model in which the turbulent kinetic energy is produced by horizontal velocity gradients only. The direct interaction of the two separate turbulent length scales is neglected, although interaction via the mean flow still exists.

3.1 Introduction

By using a single eddy viscosity for the determination of the Reynolds stresses the turbulence is assumed to be isotropic and dominated by eddies with a single characteristic length scale that contain most of the turbulent energy. Although the use of a single-length-scale turbulence model may be adequate in the majority of the situations encountered in civil engineering (ASCE, 1988), under some conditions the turbulence may become highly anisotropic. In shallow-water, for example, large quasi-2D turbulent structures may exist with length scales that are typically several times the water depth, *e.g.* (Uijttewaai & Booij, 2000). Under these circumstances the single-length-scale turbulence models are likely to fail since this anisotropy leads to the existence of turbulence structures with disparate time scales and length scales that should be accounted for separately. The use of a scalar eddy viscosity then becomes inappropriate.

Although increasing attention has been paid to shallow-water turbulence in the last few years, many questions still remain unanswered. As a consequence the modelling of this quasi-2D turbulence is still in its infancy, despite the fact that the necessity to separately

model the effects of the large scale turbulent structures on the one hand and the small-scale turbulence on the other hand has been recognised for a long time (Leendertse & Liu, 1977). Mostly, the anisotropy is introduced by distinction of the eddy viscosity that is used for the vertical Reynolds stress, related to the small-scale 3D turbulence, and the horizontal Reynolds stress related to the larger eddies, see the following section. For the latter term a so-called horizontal eddy viscosity is used.

Some numerical models use a value for the horizontal eddy viscosity which is constant in time and sometimes even constant in space. This means that the value of this eddy viscosity does not depend on the local flow characteristics, which makes it physically unsound. For large-scale tidal applications, when one is not concerned with the very details of the flow, this crude approximation has proven sufficiently accurate. However, for more detailed calculations a more sophisticated approach needs to be followed.

The simplest turbulence model for the calculation of the horizontal eddy viscosity that takes local flow characteristics into account is the Smagorinsky model (Smagorinsky, 1963). Originally designed as a sub-grid model that uses an eddy viscosity for the energy dissipation in Large Eddy calculations, it is often applied for closure of the Reynolds-averaged equations, mostly in large-scale oceanographic and atmospheric applications (Blumberg & Mellor, 1985; Delft Hydraulics, 1981). In these applications the computed eddy viscosity is used to dissipate energy which accumulates at large wave numbers and its value has no direct physical relevance. The Smagorinsky model uses a mixing-length concept in which the eddy viscosity is assumed to be proportional to the sub-grid characteristic length scale equal to the mesh width and to a characteristic turbulent velocity. The model is based on a local balance between production and dissipation. No history effects are present in this model, which are likely to be important given the long lifetime of the large scale turbulence.

In Babarutsi & Chu (1991) a depth averaged transport equation is derived for the Reynolds stresses that result from the large-scale turbulent structures. From this equation, they derive a depth averaged equation for the turbulent kinetic energy of the large eddies, which contains a loss term due to bottom friction. Together with an equation for the dissipation rate of the turbulent kinetic energy for the large-scale structures, which is identical to the ϵ equation used by Rodi (1985), it forms a depth averaged turbulence model for the large-scale structures.

In section 3.3 a two-length-scale turbulence model is presented that is specifically designed for the three-dimensional modelling of shallow-water turbulence.

3.2 Anisotropic eddy viscosity

The eddy viscosity appearing in eq. (2.26), ν_t , is a scalar, which means that any directional dependence is omitted. However, this is only realistic in a few cases of free turbulent flows and cannot be expected to be correct as a general rule. Typically the Reynolds stress in a given plane may depend on mean-velocity gradients in other planes so that the eddy

viscosity is a fourth order tensor (Hinze, 1975). Owing to its complexity, this tensor is unusable in practice and therefore a scalar is mostly used in engineering practice. However, in the case of highly non-isotropic turbulence, more than one characteristic turbulent length scale may exist. Therefore the use of a single eddy viscosity to model these types of flow appears to be inadequate.

Directional dependence, hence anisotropy, is generally introduced by splitting the eddy viscosity into two parts. The small-scale turbulence generated by bottom friction and other vertical gradients of the flow and the large-scale turbulence, fed by horizontal velocity gradients, are represented by two different viscosities, each being scalar values. Few attempts have been reported to prescribe how the horizontal eddy viscosity is related to the large scale turbulence¹. For relatively simple flow configurations it is possible to estimate a reasonable value for this coefficient, but for more complex non-stationary situations this is a less trivial task. Besides, a constant value for the eddy viscosity gives the model an empirical character.

As mentioned above, anisotropy of the turbulence can be introduced in a model by splitting the eddy viscosity into a part due to "2D turbulence", ν_t^{2D} and a part due to "3D turbulence", ν_t^v (Uittenbogaard *et al.*, 1992):

$$\nu_t^h = \nu_t^{2D} + \nu_t^v. \quad (3.1)$$

If the eddy viscosity ν_t^{2D} is taken equal to zero, an isotropic eddy viscosity is obtained. The horizontal eddy viscosity, which is assumed to be a superposition of the eddy viscosity due to "2D turbulence" and due to "3D turbulence", is used for the calculation of the horizontal Reynolds stresses. Reynolds stresses which transfer momentum in the vertical direction are modelled by using a vertical eddy viscosity ν_t^v :

$$\tau_{xz} = -\rho\nu_t^v \left(\frac{\partial u}{\partial z} \right), \quad \tau_{yz} = -\rho\nu_t^v \left(\frac{\partial v}{\partial z} \right), \quad (3.2a)$$

$$\tau_{xx} = -2\rho\nu_t^h \left(\frac{\partial u}{\partial x} \right), \quad \tau_{yy} = -2\rho\nu_t^h \left(\frac{\partial v}{\partial y} \right), \quad \tau_{xy} = \tau_{yx} = -\rho\nu_t^h \left(\frac{\partial u}{\partial y} + \frac{\partial v}{\partial x} \right). \quad (3.2b)$$

In accordance with the boundary layer approximation, some terms in eq. (3.2) are neglected compared to the full 3D Reynolds stress tensor.

The two-length-scale turbulence model presented in the next section determines the anisotropic eddy viscosity. The model consists of two single-length-scale turbulence models that together form the two-length-scale turbulence model. The 3D $k-\varepsilon$ model presented in the previous chapter is used to compute the 3D eddy viscosity while a depth averaged $k-\varepsilon$ turbulence model is used to determine the horizontal eddy viscosity ν_t^{2D} .

¹The use of the eddy viscosity concept for quasi-2D turbulence is not trivial since the eddy viscosity may become negative in this situation (Kraichnan, 1976).

3.3 Two-length-scale k - ϵ model

3.3.1 Model equations

Before discussing the two-length-scale k - ϵ turbulence model for the Reynolds averaged equations, a splitting procedure is defined that separates 3D small-scale turbulence from the quasi-2D large-scale turbulence. The small-scale turbulence represents fluctuations with wavelengths of the order of the water depth and less, whereas the large-scale turbulence is related to fluctuations with wavelengths larger than the water depth. In analogy with fully 3D turbulence the following splitting is used

$$u^{2D} + u^{3D} = U - \langle u \rangle, \quad (3.3)$$

where u^{2D} is the fluctuating part of the velocity related to the large-scale turbulent structures, u^{3D} is the fluctuating part of the velocity related to the small-scale turbulent structures and $\langle u \rangle$ is ensemble averaged in any point \mathbf{x} . In civil engineering, beds have gradual slopes and three-dimensional turbulence properties change gradually in the horizontal direction. In other words, most 3D turbulence in civil engineering is of a boundary layer type with exceptions such as near sills and gates, for example. Here the 3D turbulence is assumed to vary gradually in the horizontal direction and at scales significantly larger than the water depth H . On the other hand, 3D turbulence depends strongly on the vertical direction for bottom friction, wind and density-stratification.

In order to separate quasi-2D-turbulent motions from 3D turbulence we therefore introduce a splitting operator which is dedicated to 3D boundary layer type of turbulence. This operator averages over a horizontal area $A(\mathbf{x})$ at some depth z

$$\bar{u}^{A(\mathbf{x})} = \frac{1}{A(x, y, z)} \int_{A(\mathbf{x})} U(x', y', z') dx' dy', \quad (3.4)$$

and $A(\mathbf{x}) = \mathcal{O}(H^2)$. This operator removes 3D turbulence because it averages over many mutually independent points on $A(\mathbf{x})$ of 3D turbulence that are assumed to be (sufficiently) homogeneous on $A(\mathbf{x})$ so that the area averaging corresponds to ensemble averaging. This averaging may be performed along σ -planes or z -coordinates. Using the above averaging (3.4), we get

$$u^{2D} = \bar{u}^{A(\mathbf{x})} - \langle u \rangle, \quad (3.5)$$

and hence

$$u^{3D} = U - \bar{u}^{A(\mathbf{x})}. \quad (3.6)$$

The vertical eddy viscosity ν_t^v in eq. (3.1) represents the small-scale bottom generated turbulence, which is essentially three-dimensional and is modelled by a 3D k - ϵ model in

which the production of turbulent kinetic energy is determined solely by vertical velocity gradients. This 3D turbulence model is given in section 2.3.3 and is therefore not repeated here. The larger scale quasi-two-dimensional turbulence, represented by ν_t^{2D} , is modelled with a depth-averaged k - ε turbulence model. In analogy to the 3D k - ε model the horizontal eddy viscosity follows from

$$\nu_t^{2D} = c_\mu \frac{\overline{k}^2}{\overline{\varepsilon}}, \quad (3.7)$$

where the overlined symbols indicate depth-averaged values. Under unstratified conditions these large eddies, with a size larger than the water depth, are quasi-2D by nature. This justifies the use of two-dimensional equations.

The equations for the depth-averaged TKE, \overline{k} , and the dissipation rate $\overline{\varepsilon}$ are given by

$$\frac{D\overline{k}}{Dt} = \frac{\partial}{\partial x} \left(\frac{\nu_t^{2D}}{\sigma_k} \frac{\partial \overline{k}}{\partial x} \right) + \frac{\partial}{\partial y} \left(\frac{\nu_t^{2D}}{\sigma_k} \frac{\partial \overline{k}}{\partial y} \right) + \overline{P}_k - \overline{\varepsilon}, \quad (3.8a)$$

$$\frac{D\overline{\varepsilon}}{Dt} = \frac{\partial}{\partial x} \left(\frac{\nu_t^{2D}}{\sigma_\varepsilon} \frac{\partial \overline{\varepsilon}}{\partial x} \right) + \frac{\partial}{\partial y} \left(\frac{\nu_t^{2D}}{\sigma_\varepsilon} \frac{\partial \overline{\varepsilon}}{\partial y} \right) + \overline{P}_\varepsilon - c_{2\varepsilon} \frac{\overline{\varepsilon}^2}{\overline{k}}, \quad (3.8b)$$

where the overbar indicates depth averaging of the variables. The energy for the large eddies is mainly supplied by horizontal shear (Uijttewaal & Booij, 2000). Therefore, the production terms, \overline{P}_k and \overline{P}_ε , are determined by the horizontal shear only:

$$\overline{P}_k = \nu_t^{2D} \left[\left(\frac{\partial \overline{u}}{\partial y} + \frac{\partial \overline{v}}{\partial x} \right)^2 + 2 \left(\frac{\partial \overline{u}}{\partial x} \right)^2 + 2 \left(\frac{\partial \overline{v}}{\partial y} \right)^2 \right], \quad (3.9a)$$

$$\overline{P}_\varepsilon = c_{1\varepsilon} \frac{\overline{\varepsilon}}{\overline{k}} \overline{P}_k. \quad (3.9b)$$

3.3.2 Model assumptions and limitations

In the previous section a two-length-scale turbulence model for shallow-water turbulence is presented that is based on the eddy viscosity concept. In the case of shallow-water turbulence, reverse flow of energy from small scales to large scales is possible due to the two-dimensional nature of the turbulence. To include this phenomenon in a turbulence model that is based on the eddy viscosity concept would require a negative eddy viscosity, which may lead to numerical difficulties. However, energy transfer between the large-scale and small-scale turbulence is neglected leading to strictly positive eddy viscosities in the numerical model.

The neglect of the energy transfer between different scales is based on the estimate of the production term of the small-scale turbulence and the dissipation of the large-scale turbulence. The latter is an energy source for the small-scale turbulence, since the

dissipation of energy of the large-scale structures is related to the production of small-scale turbulence due to bottom friction and to the vortex stretching mechanism. Since the vortex stretching mechanism is impeded in the case of shallow-water turbulence, the major loss of energy for the large-scale structures, is due to bottom friction. Therefore the energy loss due to vortex stretching is assumed to be negligible. The production of turbulent kinetic energy related the 3D turbulence and produced by the mean flow \bar{u} , can be estimated by

$$P = u_*^2 \frac{\partial u}{\partial z} = c_f u_*^2 \frac{\partial u}{\partial z} \simeq c_f \frac{\bar{u}^3}{H}, \quad (3.10)$$

where u_* is the friction velocity and c_f is a friction coefficient. Assuming that the mean, depth averaged transverse velocity \bar{v} and the large-scale depth-averaged fluctuations u' and v' are much smaller than the longitudinal velocity \bar{u} , the energy loss F of the large-scale turbulence, from which the small-scale turbulence benefits, can be estimated by Babarutsi & Chu (1991)

$$F = \frac{c_f}{2h} \bar{u} (2\overline{u'^2} + \overline{v'^2}). \quad (3.11)$$

Realising that the characteristic turbulent velocities u'_i are at least an order of magnitude smaller than the mean velocities \bar{u}_i , directly shows that this term is small compared to that in eq. (3.10), and therefore can be neglected in the turbulence model.

The neglect of the energy loss of the large-scale structures due to bed friction is underpinned by comparing the energy loss in the k - ε approach to Eq. (3.11). Using the k - ε model, the rate of dissipation is approximated by

$$\varepsilon = c_D \frac{k^{3/2}}{\mathcal{L}}, \quad (3.12)$$

where $c_D \simeq 0.19$ is a model coefficient. Estimating $k \approx 0.01\bar{u}^2$ and $\mathcal{L} \approx H$ directly shows the dominance of this term and hence the friction term need not be included.

Note that the upcascading of energy from small vortices to larger scales is also neglected in this model. Too little knowledge on this physical process is available to be able to estimate the importance of this term. Furthermore, it is likely that the horizontal velocity gradients of the flow are the major source of energy supply in flows where bottom friction is of importance. In the present model, direct interaction between the two turbulence models by means of energy transfer is neglected. Interaction exists via the mean-flow equations only.

The suppression of the energy cascade process in the case of large turbulent structures, is in contradiction with the model assumptions of the k - ε turbulence model. In this k - ε model, a spectral equilibrium is assumed that is closely related to the vortex stretching mechanism. Therefore, the depth-averaged turbulence model for the determination of the horizontal eddy viscosity is used beyond its formal limits of applicability. Furthermore,

the coefficients in both the 3D and 2D model of the two-length-scale turbulence model are taken equal to these in the standard k - ε model. These coefficients were derived for turbulent flow that differs significantly from the ones under consideration and may need to be adjusted. No experimental results are used for tuning these coefficients in the two-length-scale turbulence model.

The application of the model is restricted to unstratified conditions, which means that the buoyancy terms present in eq. (2.32a) and (2.32b) are not included in the two-length-scale turbulence model. The extension of the model to make it suitable for stratified conditions is believed to be possible but complex.

3.3.3 Boundary and initial conditions

The open boundary conditions for the two-length-scale turbulence model were obtained by taking the depth averaged values of the 3D turbulence model at the open boundary. Note that in absence of shear the values for the turbulent quantities at the open boundary are then equal to zero. Homogeneous Neumann conditions are imposed at closed boundaries:

$$\frac{\partial \bar{k}}{\partial n} = 0 \text{ and } \frac{\partial \bar{\varepsilon}}{\partial n} = 0. \quad (3.13)$$

The initial conditions for the two-length-scale turbulence model were chosen such that a realistic value for the turbulent kinetic energy and eddy viscosity are obtained for the problems considered. The values for the turbulent quantities therefore depend on the approximate mean flow velocities and are constant throughout the computational domain.

3.3.4 Discretisation two-length-scale turbulence model

The horizontal eddy viscosity ν_t^{2D} is determined from a depth-averaged k - ε turbulence model. The transport equations for the depth-averaged turbulent quantities \bar{k} and $\bar{\varepsilon}$ are solved explicitly, except from the dissipation term which is integrated using Newton linearisation. Again, we restrict ourselves to the discretisation of the k -equation which reads in semi-discrete form

$$\begin{aligned} \frac{\bar{k}_{i+1/2,j+1/2}^{n+1} - \bar{k}_{i+1/2,j+1/2}^n}{\Delta t} = & -\bar{u} \frac{\partial \bar{k}^n}{\partial x} - \bar{v} \frac{\partial \bar{k}^n}{\partial y} + \\ & \frac{\partial \nu_t^{2D}}{\partial x} \frac{\partial \bar{k}^n}{\partial x} + \frac{\partial \nu_t^{2D}}{\partial y} \frac{\partial \bar{k}^n}{\partial y} + \bar{P}_k^n - \bar{\varepsilon}^{n+1}. \end{aligned} \quad (3.14)$$

Note that the position of k changed from i, j to $i+\frac{1}{2}, j+\frac{1}{2}$. This is done for reasons of accuracy. Within the two-length-scale turbulence model the horizontal eddy viscosity is no longer constant in space. Consequently, the Laplace operator eq. (2.60) should no longer be applied for the horizontal eddy viscosity term. The full Reynolds stress according to eq.

(3.2) and (2.8) is therefore implemented to compute the horizontal eddy viscosity term. In the Reynolds stress term the Reynolds shear stress is the most important part of the tensor in the case of shallow-water turbulence. For this reason accurate approximation of the shear stress term is crucial. To avoid excessive averaging of the horizontal eddy viscosity in computing the horizontal Reynolds shear stress, a new definition of variables on the staggered grid was introduced. In contrast with the original definition of the staggered grid in section 2.5.4, k and ε were shifted from the water level points to the water depth points, see Figure 3.1.

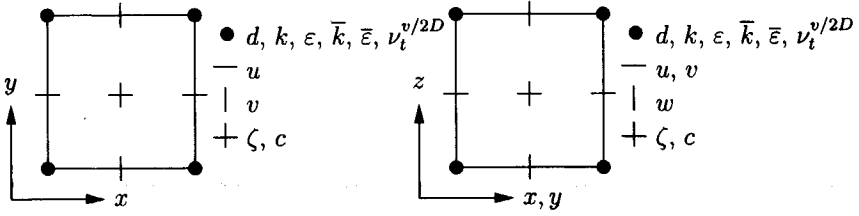


Figure 3.1: Alternative definition of staggered grid. The turbulent quantities are located at a different position compared to Figure 2.1.

Transformation terms, both in horizontal and vertical direction, are omitted in the discretisation of the Reynolds stress. In Cartesian coordinates the new staggered grid yields the following discretisation

$$\tau_{xy}|_{i,j+1/2,k} \approx -\nu_{t,i+1/2,j+1/2}^h \left(\frac{u_{i+1/2,j+1,k}^n - u_{i+1/2,j,k}^n}{\Delta y_{i+1/2,j+1/2}} + \frac{v_{i+1,j+1/2,k}^n - u_{i,j+1/2,k}^n}{\Delta x_{i+1/2,j+1/2}} \right), \quad (3.15)$$

which results for the momentum equation in:

$$\frac{1}{\rho_0} \frac{\partial \tau_{xy}}{\partial y} \Big|_{i+1/2,j,k} \approx \frac{1}{\rho_0} \left(\frac{\tau_{xy,i+1/2,j+1/2,k} - \tau_{xy,i+1/2,j-1/2,k}}{\Delta y_{i+1/2,j}} \right). \quad (3.16)$$

The horizontal normal stress is computed in the water level point

$$\tau_{xx}|_{i,j,k} \approx -2\overline{\nu}_t^h \left(\frac{u_{i+1/2,j,k}^n - u_{i-1/2,j,k}^n}{\Delta x_{i,j}} \right), \quad (3.17)$$

where $\overline{\nu}_t^h = \frac{1}{4}(\nu_{t,i+1/2,j+1/2}^h + \nu_{t,i-1/2,j+1/2}^h + \nu_{t,i+1/2,j-1/2}^h + \nu_{t,i-1/2,j-1/2}^h)$. The horizontal viscosity term is then computed by

$$\frac{1}{\rho_0} \frac{\partial \tau_{xx}}{\partial x} \Big|_{i+1/2,j,k} \approx \frac{1}{\rho_0} \left(\frac{\tau_{xx,i+1/2,j,k} - \tau_{xx,i-1/2,j,k}}{\Delta x_{i+1/2,j}} \right). \quad (3.18)$$

In a similar way the normal stress in y -direction is obtained.

The alternative location of the variables also leads to a more accurate determination of the major production term which is due to velocity shear. The production term in the depth-averaged part of the two-length-scale turbulence model now reads

$$\begin{aligned} \bar{P}_k|_{i+1/2,j+1/2} \approx \nu_t^{2D} \left[\left(\frac{\bar{u}_{i+1/2,j+1}^n - \bar{u}_{i+1/2,j}^n}{\Delta y_{i+1/2,j+1/2}} + \frac{\bar{v}_{i+1,j+1/2}^n - \bar{v}_{i,j+1/2}^n}{\Delta x_{i+1/2,j+1/2}} \right)^2 + \right. \\ \left. \frac{2}{4} \left(\nabla_x \bar{u}_{i,j} + \nabla_x \bar{u}_{i+1,j} + \nabla_x \bar{u}_{i,j+1} + \nabla_x \bar{u}_{i+1,j+1} + \right. \right. \\ \left. \left. \nabla_y \bar{v}_{i,j} + \nabla_y \bar{v}_{i+1,j} + \nabla_y \bar{v}_{i,j+1} + \nabla_y \bar{v}_{i+1,j+1} \right) \right], \end{aligned} \quad (3.19)$$

where an overbar indicates a depth-averaged value, $\nabla_x \bar{u}_{i,j} = (\bar{u}_{i+1/2,j} - \bar{u}_{i-1/2,j})/\Delta x_{i,j}$ and $\nabla_y \bar{v}_{i,j} = (\bar{v}_{i,j+1/2} - \bar{v}_{i,j-1/2})/\Delta y_{i,j}$. Additional transformation terms, both in horizontal and vertical direction, are omitted and the discretisation is therefore performed in Cartesian coordinates. In the above equations averaging in computing the normal Reynolds stresses and in computing the divergence of the velocity in the production term increases, but these terms are of minor importance.

In order to get a sound comparison of the single-length-scale turbulence model and the two-length-scale turbulence model, the displacement of the variables is applied in both models. It is noted that the displacement is applied in the application described in Chapter 4 only. The shift of k and ε to the depth points implies a change in the averaging procedure for the vertical diffusion terms in the momentum equation and the production term in the 3D k - ε model. The discretisation of these terms in section 2.5.4 and 2.5.7 therefore changes slightly. However, this change is only related to the direction of interpolation and is not likely to affect the results significantly.

The spatial derivatives in the equations of both the 3D turbulence model and the 2D turbulence model, are discretised in a non-conservative way. It is plausible that this will hardly hamper the accuracy of the results for the 3D model since production and dissipation of k will dominate the solution of these equations in the major part of the computational domain. In the case of the depth averaged turbulence model, this is less likely to be correct; the large turbulent structures have a long lifetime and therefore history effects are more important. However, due to the selected position of \bar{k} and $\bar{\varepsilon}$ on the staggered grid, the use of a conservative formulation would require extra averaging of variables which might cancel the improvement in computing the Reynolds shear stress by moving the k and ε points. Therefore a non-conservative approach is chosen for the discretisation of the transport equations for the turbulent quantities.

Related to this the advection terms in the depth-averaged equations for \bar{k} and $\bar{\varepsilon}$ are discretised with an upwind method which integrates along streamlines, similar to the advective terms in the momentum equation. In this way, the cross-wind diffusion related to the standard first order upwind method is suppressed when the local velocity vector is not

aligned with the grid. This way a more accurate and positive solution is guaranteed as will be shown in chapter 4. Using this method, for positive u and v , the following is obtained:

$$\begin{aligned} \bar{u} \frac{\partial \bar{k}}{\partial x} + \bar{v} \frac{\partial \bar{k}}{\partial y} \Big|_{i+1/2, j+1/2} &\approx \frac{\tilde{u}}{\Delta x_{i, j+1/2}} (\bar{k}_{i+1/2, j+1/2}^n - \bar{k}_{i-1/2, j+1/2}^n) + \\ &\quad \frac{\tilde{v}}{\Delta y_{i-1/2, j}} (\bar{k}_{i-1/2, j+1/2}^n - \bar{k}_{i-1/2, j-1/2}^n) \quad \text{if } \frac{\tilde{u}}{\Delta x_{i, j+1/2}} > \frac{\tilde{v}}{\Delta y_{i-1/2, j}}, \\ \bar{u} \frac{\partial \bar{k}}{\partial x} + \bar{v} \frac{\partial \bar{k}}{\partial y} \Big|_{i+1/2, j+1/2} &\approx \frac{\tilde{u}}{\Delta x_{i, j-1/2}} (\bar{k}_{i+1/2, j-1/2}^n - \bar{k}_{i-1/2, j-1/2}^n) + \\ &\quad \frac{\tilde{v}}{\Delta y_{i+1/2, j}} (\bar{k}_{i+1/2, j+1/2}^n - \bar{k}_{i+1/2, j-1/2}^n) \quad \text{if } \frac{\tilde{u}}{\Delta x_{i, j-1/2}} \leq \frac{\tilde{v}}{\Delta y_{i+1/2, j}}, \end{aligned} \quad (3.20)$$

where $\tilde{u} = \frac{1}{2}(\bar{u}_{i+1/2, j}^n + \bar{u}_{i+1/2, j+1}^n)$ and $\tilde{v} = \frac{1}{2}(\bar{v}_{i, j+1/2}^n + \bar{v}_{i+1, j+1/2}^n)$. The horizontal diffusion is computed by

$$\begin{aligned} \frac{\partial}{\partial x} \nu_i^{2D} \frac{\partial \bar{k}}{\partial x} \Big|_{i+1/2, j+1/2} &\approx \frac{\bar{\nu}_i^{2D}}{\sigma_t \Delta x_{i+1/2, j+1/2}} \frac{\bar{k}_{i+3/2, j+1/2}^n - \bar{k}_{i+1/2, j+1/2}^n}{\Delta x_{i+1, j+1/2}} - \\ &\quad \frac{\bar{\nu}_i^{2D}}{\sigma_t \Delta x_{i+1/2, j+1/2}} \frac{\bar{k}_{i+1/2, j+1/2}^n - \bar{k}_{i-1/2, j+1/2}^n}{\Delta x_{i, j+1/2}}. \end{aligned} \quad (3.21)$$

For the dissipation the same Newton linearisation procedure is used as in the 3D model and is therefore not repeated here.

Chapter 4

Application of the two-length-scale k - ε model

In this chapter results of simulations using the two-length-scale k - ε model are discussed and compared to measurements¹. Recirculating unstratified flow in two model harbours is studied. In both cases the turbulent flow was driven by a stationary current in an adjacent model river. Two different geometric configurations were studied. Measurements of mean velocities of a driven cavity flow in a square model harbour, carried out by Langendoen (1992), are used for model verification. Furthermore, the performance of the turbulence model is tested for a more realistic situation, *i.e.* a scale model of an existing yacht harbour. In the latter model Laser Doppler measurements revealed the coexistence of two disparate characteristic turbulent length scales in the mixing layer between the river and the harbour, induced by the shallowness of the water.

4.1 Laboratory measurements yacht harbour " 't Steel"

4.1.1 Introduction

Very little data is available on the behaviour of large-scale turbulence in shallow areas. Only recently experiments have been initiated that concern quasi-two-dimensional turbulence (Chu *et al.*, 1991; Dracos *et al.*, 1992; Uijttewaal & Booij, 2000). In order to create a data set for validation of the turbulence model presented in the previous chapter, laboratory measurements were carried out at the Fluid Mechanics Laboratory of the Civil Engineering department of Delft University of Technology. The aim of these experiments was to determine the flow characteristics of a stationary recirculating flow in a harbour. Mean flow quantities as well as turbulent fluctuations of the horizontal velocity components were measured. From the turbulent fluctuations, the horizontal Reynolds shear stress can

¹This chapter is published in adapted form in Bijvelds *et al.* (1998) and Bijvelds *et al.* (1999a)

be computed, which is a good indicator of the quality of the turbulence model in the case of quasi-two-dimensional turbulence.

4.1.2 Experimental set-up

The scale model that is used for the laboratory measurements, is derived from yacht harbour "t Steel" on the river Meuse in the Netherlands (Bijvelds, 1997). The scale of the model is equal to 1:50 in both vertical and horizontal planes. The bathymetry of the scale model is depicted in Figure 4.1. At the inflow boundary of the model which is located at $x=0$, a flow rate of $0.041 \text{ m}^3/\text{s}$ was imposed. This yields a Reynolds number, $Re = \frac{\bar{u}H}{\nu}$, based upon the mean flow velocity in the river, \bar{u} , and the mean water depth in the river, H , of approximately 40000 which means that the flow is turbulent. In the harbour basin itself, velocities are much lower and the corresponding bulk Reynolds number is as low as 2000. The Froude number in the river, $Fr = \frac{\bar{u}}{\sqrt{gH}}$, equals 0.28 which satisfies the conditions that the flow should be sub-critical and that no surface waves are generated.

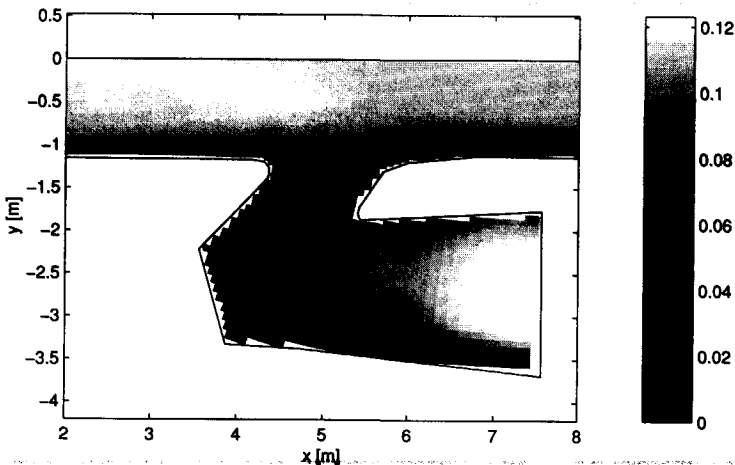


Figure 4.1: Digitised bathymetry of the physical model (depth in m). The actual length of the river is 9 m.

The measurements were carried out using the so-called HILDA, a submersible laser Doppler anemometer (LDA) of Delft Hydraulics. Velocities in a horizontal plane in two orthogonal directions were measured simultaneously, which makes it possible to determine horizontal Reynolds stresses. However, vertical velocities are not measured, leaving the vertical Reynolds stresses and the exact total turbulent kinetic energy per unit mass, $k = \frac{1}{2}(\overline{u'^2} + \overline{v'^2} + \overline{w'^2})$, undetermined.

The sampling rate of the LDA measurements and the sampling period are determined by the accuracy required and by the information to be obtained from the measurements. The measuring time was taken equal to 10 minutes and the frequency was 100 Hz. These figures are based on a 10 % error in the normal Reynolds stresses or TKE and allow for analysis of the turbulence occurring in the scale model down to the viscous subrange, see Appendix A. For more details on the measurements, the reader is referred to (Bijvelds, 1997).

The LDA measurements were performed mainly in the area of interest, *i.e.* in the mixing layer region. In the remainder of the domain, particle tracking velocimetry (PTV) is used to obtain mean-flow information. With this technique a dense vector field of velocity at the free surface is obtained.

4.1.3 Experimental results

Large quasi-2D coherent turbulent structures are induced by transverse shear instabilities. These arise due to velocity differences caused by topographic changes near the harbour entrance. Depending on the ratio of the loss of large-scale kinetic energy due to bottom friction and the production of large-scale turbulent kinetic energy due to transverse velocity gradients, transverse shear instabilities can give rise to the gradual growth of large coherent structures (Ingram & Chu, 1987; Chu *et al.*, 1991). In the case that bottom friction is dominant, the stabilising effect of the bottom friction on the large structures suppresses the growth of the turbulent structures. The turbulence can then be considered as three-dimensional. In the present experiments this is not the case as can be concluded from Figure 4.2. By injecting dissolved KMnO_4 into the water upstream of the mixing layer, turbulent structures can be observed with a typical size of several times the water depth.

Three regions can be discerned in the development of the large structures. In the near-field the shearing flow contains 3D small-scale turbulence with a length scale of typically the water depth. The power spectrum of the turbulent kinetic energy in the near field is similar to power spectra measured in three-dimensional turbulence, showing for sufficiently large Reynolds numbers an inertial subrange with a $-5/3$ wave number dependence. Somewhat further downstream (intermediate-field), there is a strong interaction between the flow and the vertical boundaries, *i.e.* the bottom and the free surface. In this region large structures start to develop. The spectral energy density at small wave numbers increases significantly faster than in the near field and at the same time the peak around the maximum becomes more pronounced. In addition, a range develops in which the energy transfer follows a -3 wave number dependence, which indicates the presence of (quasi-)two-dimensional turbulent structures. Although not as pronounced as reported in some experiments in the literature, this slope can be discerned in Figure 4.3.

Transverse velocity fluctuations (v') were used for the computation of characteristic power spectra. The same sample positions as for the autocorrelation function were used for the power spectra. At low frequencies, the energy can be seen not to go to zero, which

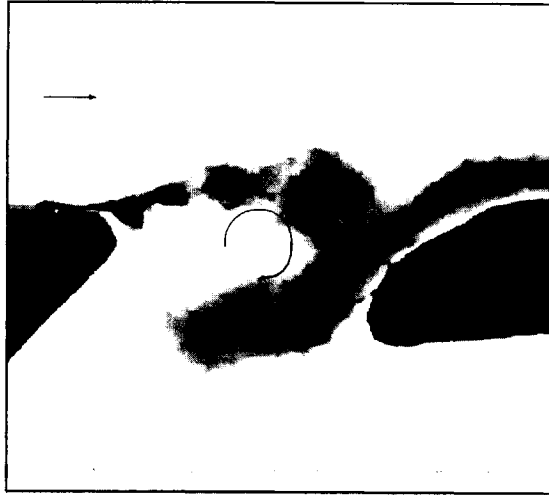


Figure 4.2: Top view of a shallow-water mixing layer in the harbour entrance and the approximate flow pattern. Four (developing) quasi-2D structures and a gyre can be discerned. The width of the harbour entrance is approximately 10 times the average water depth.

is due to the effect of aliasing (Tennekes & Lumley, 1972). Apart from the difference in total amount of turbulent energy, the major difference between the spectrum in the river and the mixing layer occurs at low frequencies. The peak at low frequencies, near 0.3 Hz, occurs in the energy spectrum of the sample point in the mixing layer only and can be ascribed to quasi two-dimensional turbulent structures.

At higher frequencies a $-5/3$ slope can be discerned, which is related to an inertial subrange in three-dimensional turbulence. This reflects the presence of an energy cascade related to the vortex stretching process. The range in which the slope equals $-5/3$ is rather small due to the relatively low Reynolds number, indicating a small separation between the macro- and micro-structure of the turbulence.

In the far-field, the turbulent structures have grown to sizes (significantly) larger than the water depth. Because of the kinematic constraints, these vortical structures have a dominant vertical vorticity component and they may grow in size by pairing. These large-scale structures are hardly affected by the small-scale turbulence. Moreover, since vortex stretching of the large-scale structures is impeded and the large structures are well organised with respect to each other, these large-scale structures have a long lifetime. This is characterised by the quasi-periodic behaviour of the autocorrelation function of the turbulent part of the transverse velocity component, see Figure 4.4. Similar autocorrelation

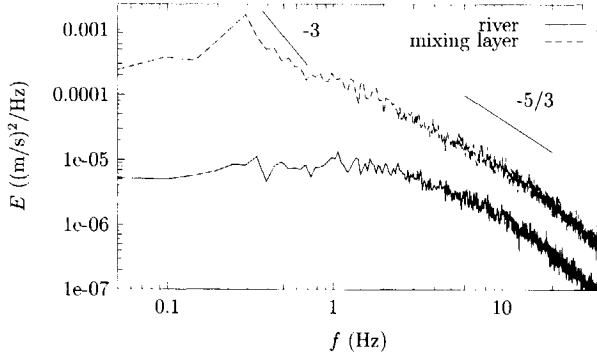


Figure 4.3: One-dimensional power-density spectrum of transverse velocity fluctuations (v') in the river and mixing layer

functions have been reported by (Dracos *et al.*, 1992; Uijtewaal & Tukker, 1998), for example.

The autocorrelation function of velocity can be used to gain insight into the spatial dimensions of the turbulent structures that develop in the mixing layer. Time- or auto correlations are used for determining typical length scales by multiplying the characteristic time-scale by the mean local velocity. This method can only be applied when the average life time of an eddy is large compared to the mean transport time needed to detect it, a requirement which in general is fulfilled. This means that the eddy hardly changes while it is advected along the measuring probe, *i.e.* the turbulence is "frozen" (Taylor hypothesis).

As can be seen from Figure 4.4, the large-scale periodic structures are responsible for large correlation coefficients of varying sign for large time-shifts. Because of this oscillatory behaviour of the autocorrelation function in the case of quasi-2D turbulence, it is impossible to determine the characteristic time scale of the turbulence by $\int_0^\infty \rho(\tau) d\tau$ (Tennekes & Lumley, 1972) where $\rho(\tau)$ is the autocorrelation function and τ is the time shift. Therefore, the computed integral time-scale is related to the quasi-periodic fluctuations present in the measured time signal, as suggested in (Tukker, 1997).

The spatial extension of the turbulent structures is revealed most clearly by considering the transverse velocity component, *i.e.* the velocity in horizontal direction perpendicular to the mean flow. In Figure 4.4, typical autocorrelation functions of the transverse velocity fluctuations in the river and mixing layer at mid-depth are shown.

In the river, the fluctuating velocities are shown to be correlated for a small time-shift τ only, indicating that only small-scale turbulence is present at this position. The spatial dimension of the small-scale turbulence is determined by multiplying the integral

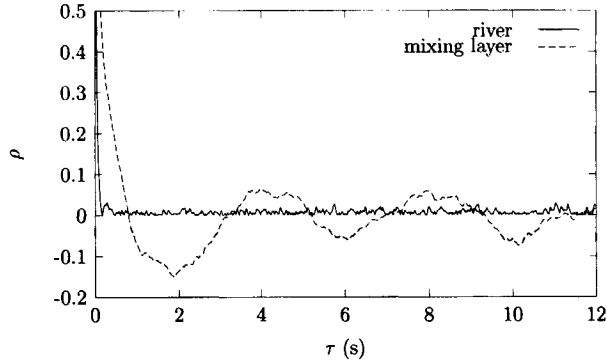


Figure 4.4: Typical autocorrelation function of the transverse velocity fluctuations (v') in the river (R) and mixing layer (M).

time scale, which is about 0.15 s, with the mean velocity at this position. This yields a turbulent length scale of 0.09 m, which is of the order of the water depth. This small-scale turbulence can also be recognised in the autocorrelation function in the mixing layer; near the origin, the autocorrelation function drops suddenly from 1 to about 0.3 (where the slope diminishes) indicating limited coherence of the small-scale motions. The existence of large coherent turbulent structures can easily be discerned from Figure 4.4. The slowly decaying autocorrelation indicates a spatial dimension of the large structures of about 0.9 m, which is much larger than the local water depth.

4.2 Driven cavity flow in a square model harbour

4.2.1 Model description

The first situation to be considered is that of a square harbour, 1×1 m, adjacent to a 18 m long and 1 m wide prismatic channel. The still-water depth equals 0.11 m throughout the entire model and the sidewalls of the model are vertical. At the inflow boundary a flow rate of $0.042 \text{ m}^3/\text{s}$ is imposed yielding a mean flow velocity of 0.37 m/s. At the harbour entrance a mixing layer will develop due to the velocity difference between the river and harbour. Momentum is transferred by turbulence from the river to the harbour, resulting in a recirculating flow (gyre) which covers the whole harbour.

At four different levels, 0.015 m, 0.04 m, 0.06 m and 0.08 m above the bottom, mean velocities have been measured at various positions in a horizontal plane. Besides, more detailed information on the vertical distribution of the horizontal velocity components is

available at one position P near the stagnation point, see Figure 4.5. For hydraulically rough conditions, the measured value of the bed-friction coefficient is equivalent with a roughness height according to Nikuradse, k_N , equal to 4.05×10^{-3} m. These data are used for model verification. For more detailed information on the experiments, the reader is referred to (Langendoen, 1992).

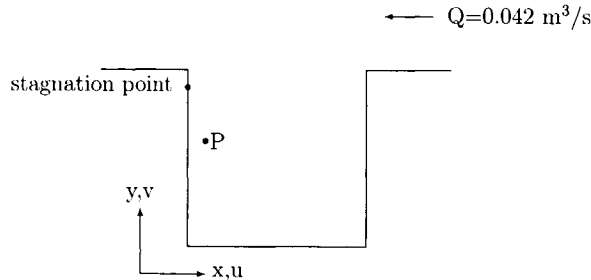


Figure 4.5: Definition sketch of square harbour.

4.2.2 Computational results

The harbour and a section of the river with a length of 5 m were schematised in the numerical model. The open boundaries were situated at 2.5 m from the centre-line of the harbour. At the inflow boundary a flow rate equal to the flow rate in the physical model was imposed and the vertical velocity profiles were assumed to be logarithmic. At the outflow boundary a depth of 0.11 m is imposed.

Computations were carried out on different grids to check the convergence of the solutions. The converged solution was obtained on a grid consisting of 88 x 64 grid points. The grid spacing in the harbour varies between 2 cm near the closed boundaries and mixing layer and 4.3 cm at the centre of the harbour see Figure 4.6. In the vertical direction 10 layers were used, with decreasing vertical grid spacing towards the bottom (15, 15, 14, 14, 12, 10, 8, 6, 4 and 2 per cent of the water depth) in order to represent large gradients near the bottom accurately.

In order to judge the computed results, two graphical presentations of velocities are used. At four different levels above the bottom, velocities along two transects through the centre of the gyre are available. Besides, vertical velocity profiles of both horizontal velocity components at position P near the stagnation point are available for comparison, see Figure 4.5. First of all computed velocities at four different levels in the water column are compared to the measured velocities. The computed results are obtained with three different models. Besides the $k-\varepsilon$ model as presented in section 2.3.3 and the new two-length-scale $k-\varepsilon$ turbulence model, the standard 3D $k-\varepsilon$ model of Launder and Spalding

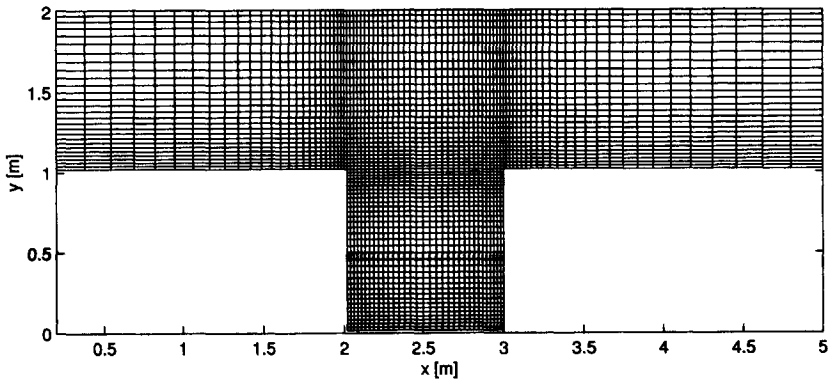


Figure 4.6: Computational grid of the square harbour.

(1972) is used for comparison ². An additional 2D eddy viscosity was added to the DH-model because no production of turbulence due to horizontal shear is included in this model. In an earlier paper this horizontal viscosity was taken equal to $5 \times 10^{-4} \text{ m}^2/\text{s}$, which value was based upon the turbulence generated in the mixing layer (Langendoen & Kranenburg, 1993). This value is also used in the present calculations.

The measured and computed velocities at 0.015 m, 0.04 m, 0.06 m and 0.08 m above the bottom are compared along two transects through the measured centre of the gyre, see Figure 4.7. In the x -direction the u -component of the velocity vector is plotted and in y -direction the v -component. Linear interpolation was used to obtain computed velocities at these heights. It can be concluded from this figure that all models perform equally well at these positions and computed results agree well with the measured data, including the computed centre of the gyre. It must be noted that the success of the DH-model can be ascribed to the correctness of the constant eddy viscosity; two-dimensional calculations of the flow in a square harbour (Booij, 1989) with a depth-averaged k - ε model confirm that the eddy viscosity is almost constant in the harbour. In more complex practical situations where the eddy viscosity varies in time and space, this approach is likely to fail. The computed velocity field in the square harbour is plotted in Figure 4.8.

A major difference between the mixing layer width obtained with the LS-model and the TLS-model is observed. Defining the mixing layer width by

$$B = \frac{\Delta u}{\left(\frac{\partial u}{\partial y}\right)_{\max}} \quad (4.1)$$

²The three turbulence models are indicated by DH, TLS and LS respectively in the remainder of the thesis

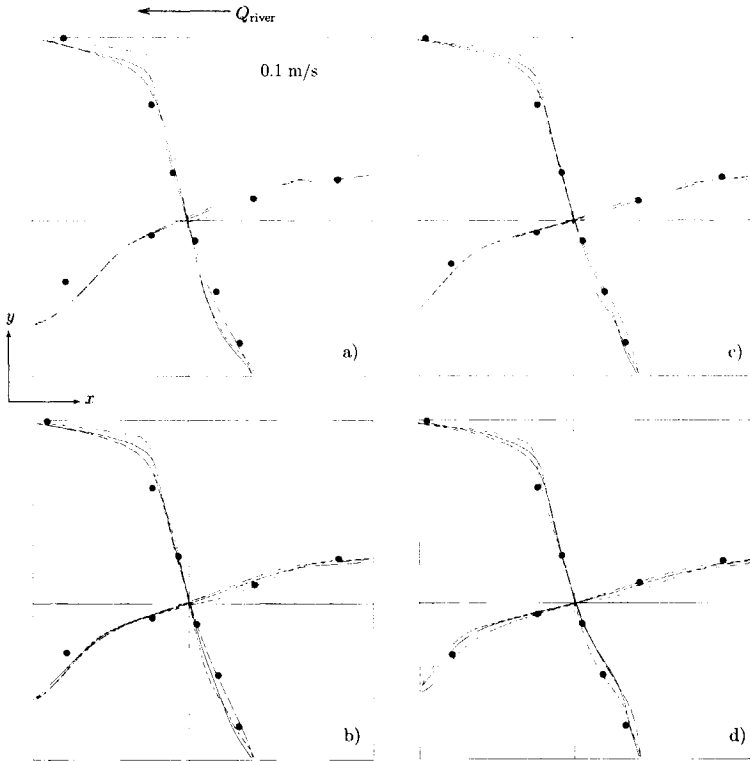


Figure 4.7: Velocity profiles along two transects through the measured centre of the gyre; a) 0.015 b) 0.04 c) 0.06 and d) 0.08 m above the bottom. Measured: black dots, LS-model: small dashes, DH-model with $\nu_t^2 D = 5 \times 10^{-4} \text{ m}^2/\text{s}$: large dashes, TLS-model: solid line.

where Δu is the velocity difference over the mixing layer and the denominator represents the maximum velocity gradient in the mixing layer, the linear growth of the mixing layer in the LS-model equals $B = 0.13x$. Here x is the coordinate in the mean flow direction of the river and has its origin at the separation point. The TLS model, on the other hand, yields a larger growth of the mixing layer that is approximately equal to $B = 0.20x$. The data from Langendoen (1992) are too coarse to draw any definite conclusion about the growth of the mixing layer in the harbour entrance. However, more detailed measurements of velocities at mid-depth in a $1 \times 1 \text{ m}$ square harbour with similar flow conditions are available from Booij (1986). He measured a width of the mixing layer of $B = 0.23x$. It can be concluded that the proposed TLS turbulence model performs better than the standard $k-\varepsilon$ model in

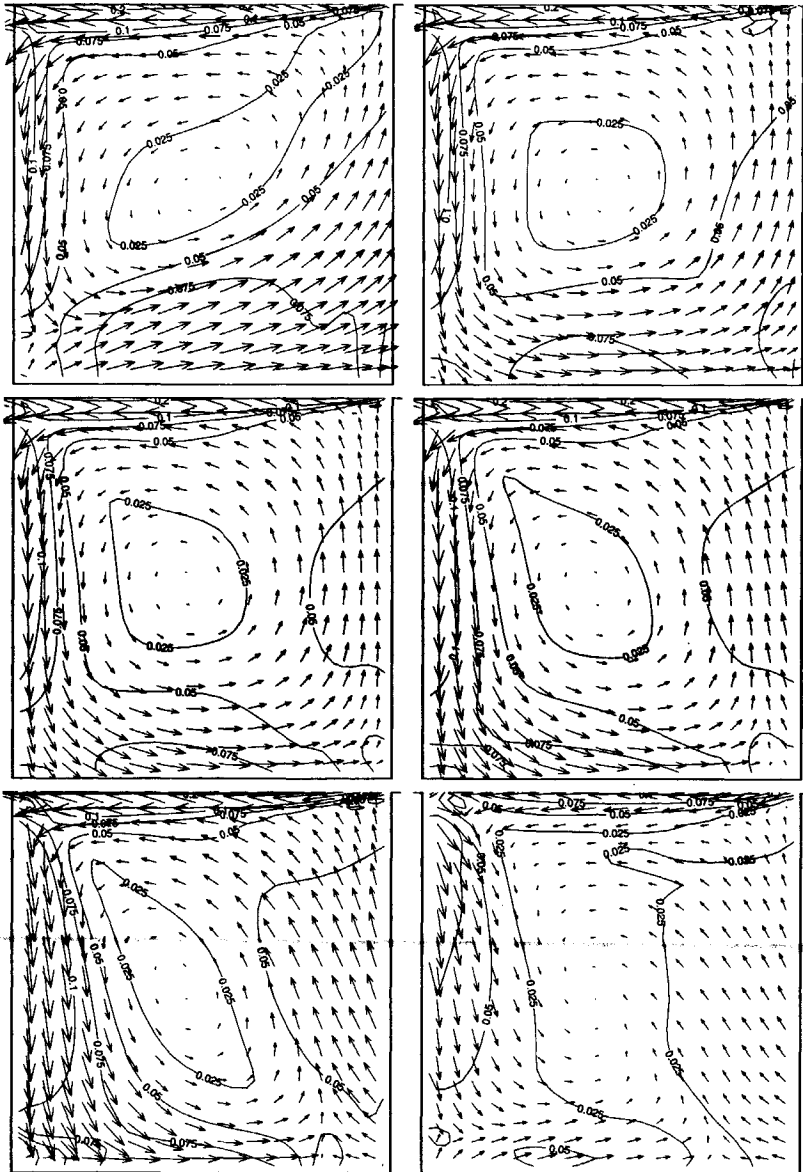


Figure 4.8: Computed vector fields in the square harbour with the TLS model at elevations of 7.5%, 37% (upper), 51%, 64% (middle), 84% and 99% (lower) of the water depth. The isolines indicate the magnitude of the velocity (in m/s). Every second vector is plotted.

the mixing layer region, something that will be supported later in this thesis.

Figure 4.9 shows the distributions of the horizontal velocity components in the vertical at point P, 0.4 m from the transition from harbour to river and 0.1 m from the harbour sidewall. At this position high-momentum fluid in the mixing layer flows from close to the surface towards the bottom in the harbour (Langendoen, 1992). Comparing computed

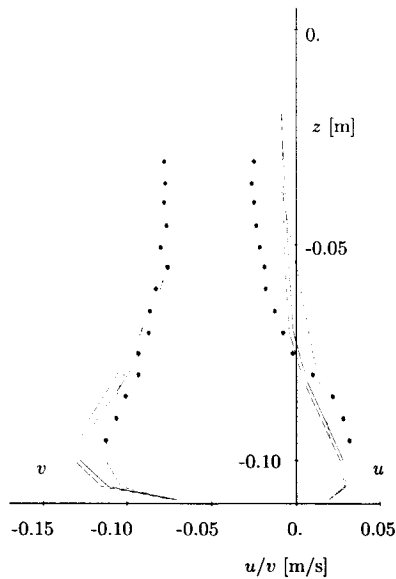


Figure 4.9: Vertical distributions of the horizontal velocity components u and v . Measured: black dots, LS-model: small dashes, DH-model with $\nu_t^{2D}=5 \times 10^{-4} \text{ m}^2/\text{s}$: large dashes, TLS-model: solid line.

velocity distributions with the measured ones, it is observed that the characteristic velocity profiles are predicted better with the DH-model and TLS-model than with the LS-model, both qualitatively and quantitatively. Especially near the surface, where the eddy viscosity vanishes in the case of the standard turbulence model, better agreement with measurements is found. It must be noted that the existence of the bulb which appears in the computed profile near the bottom was found to be strongly dependent upon the turbulence model used; several other turbulence models yielded, in contrast with the measurements, log-like velocity distributions and thus failed to represent this 3D feature of the flow.

The above mentioned conclusions also hold for the secondary motion normal to the wall (which is caused by the recirculating flow in the harbour) although the magnitude of

this current is underpredicted considerably with all turbulence models. In contrast with the TLS-model the LS-model is less capable of predicting the typical shape of the velocity profiles in primary and secondary flow directions.

The boundary conditions imposed at the walls for k and ε may play an important role in predicting the above mentioned bulb and the secondary flow. Near the stagnation point, these boundary conditions are likely to be incorrect since they were derived for a developed flow, which obviously is not present in that area. The wall-friction eliminates part of the pressure build-up near the wall, so that the secondary current is reduced. Besides this, the flow near the stagnation point does not fulfill the restrictions following from the assumed hydrostatic pressure distribution, *i.e.* the flow is locally non-hydrostatic. The vertical accelerations near the solid boundary are not noticeable at monitoring position P, which influences the velocity profile of the secondary current significantly. As a consequence, vertical velocities are concentrated near the sidewall introducing high velocities and velocity gradients.

Isolines of the computed distribution of ν_t^v , ν_t^{2D} , k , \bar{k} , ε , and $\bar{\varepsilon}$ are shown in Figure 4.10. **The transport of the turbulence generated by horizontal shear is seen to die out slowly as mentioned before.** The predicted 2D eddy viscosity is almost constant through the harbour, which explains the similar solutions for the TLS-model and the DH-model with constant eddy viscosity.

To stress that a standard first order scheme for discretising advective terms should not be used in multi-dimensional situations, the distribution of \bar{k} using this method is compared to the more accurate method which discretises advective terms along streamlines in Figure 4.11. This result supports the opposition against usage of standard first-order upwind for advective modelling in multi-dimensional calculations, *e.g.* (Leonard & Drummond, 1995). The artificial cross-wind diffusion related to first order differencing smears out the solution, causing the turbulence to die out rapidly. This numerical side-effect is most distinct in regions where the flow crosses the grid cells under a considerable angle, which is the case near the corners of the harbour. This becomes clear if the lower left corner of the harbour is considered, where turbulence is not "capable" of crossing the corner, whereas it clearly can when derivatives are determined along streamlines. Low values of \bar{k} in a large part of the harbour area results in small horizontal transfer of momentum other than generated by bottom turbulence in this region. Although there is no large difference between the development of the mixing layer in both approximations, the gross underestimation of TKE in the harbour causes too small a horizontal eddy viscosity ν_t^h in a large area. Lack of momentum transfer in horizontal directions yields local maxima, and secondary gyres can be generated leading to physically unrealistic flow patterns. From this point of view it might be important to use a conservative scheme.

In contrast with the TLS-model, the results of the model with constant eddy viscosity do not vary much with changing grid resolution. This is caused by the fact that the eddy viscosity in the TLS model is calculated and strongly depends on local velocity gradients which by definition are calculated more accurately if a small grid spacing is used. In

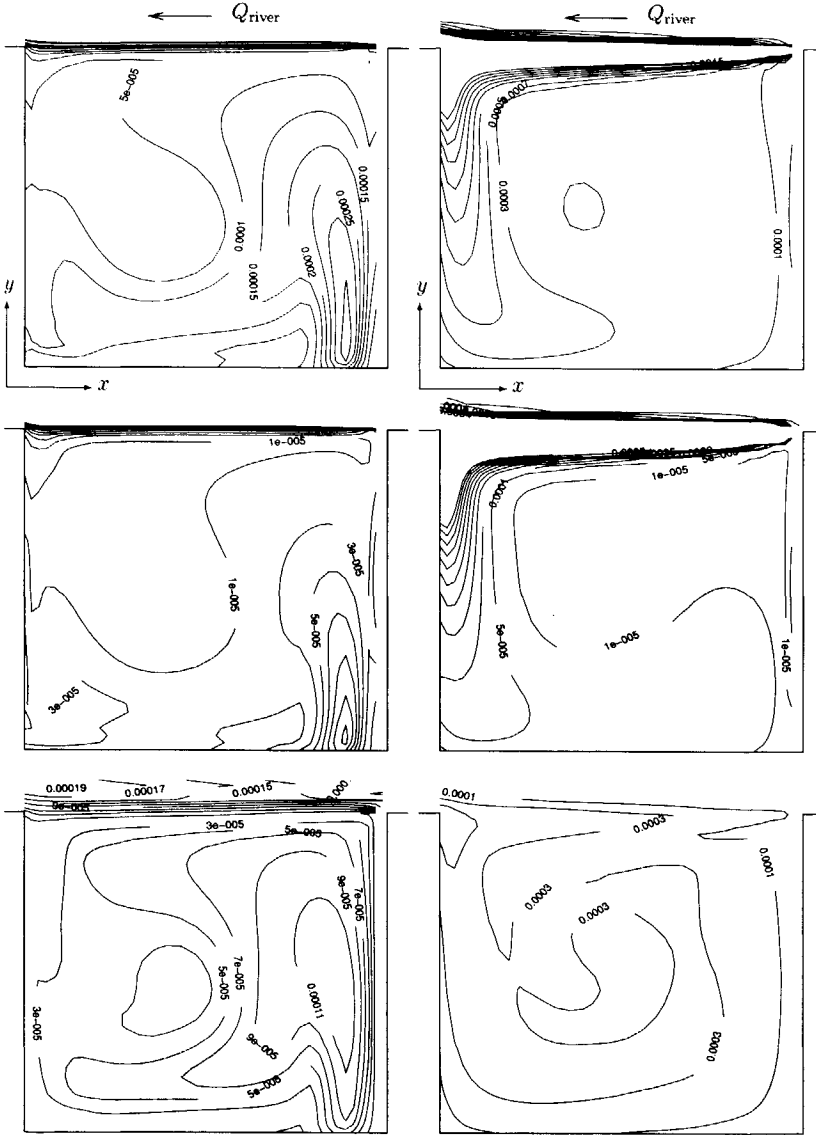


Figure 4.10: Left: isolines of v_i^v (m²/s), k (m²/s²), and ϵ (m²/s³), from top to bottom, in the square harbour at 51% of the water depth. Right: isolines of v_i^{2D} (m²/s), \bar{k} (m²/s²), and $\bar{\epsilon}$ (m²/s³), from top to bottom.

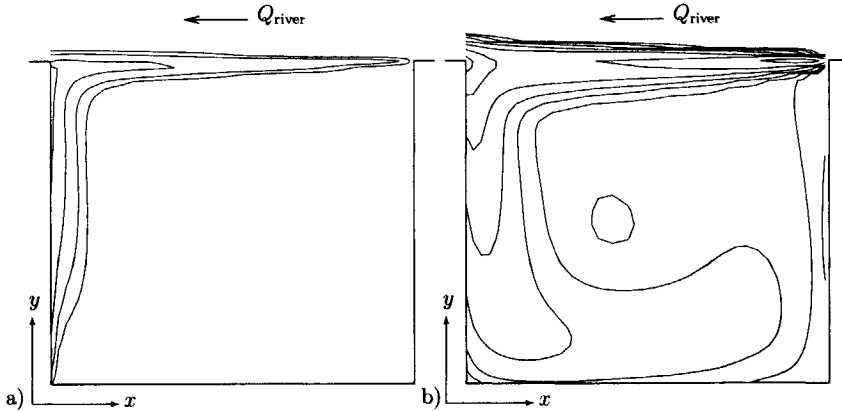


Figure 4.11: Isolines of \bar{k} in harbour for $\bar{k}=0.0001, 0.0002, 0.0004, 0.0008, 0.0016, 0.0032$ and $0.0064 \text{ m}^2/\text{s}^2$: a) standard first order upwind; b) first order upwind along streamlines.

the case of the coarse grid, the mixing layer is modelled by only a few grid cells, hence velocity gradients are not represented correctly. Refining the grid, the two solutions tend to converge as shown above. A major disadvantage of the grid refinement needed for the TLS-model, is the increasing computing costs involved. However, it is believed that grid refinement is only needed in areas of large horizontal velocity gradients, hence a substantial reduction in CPU time can be achieved without losing much accuracy. It is noted that the increase in CPU time needed for the additional depth-averaged turbulence model is negligible compared to the other numerical operations.

4.3 Modelling yacht harbour "t Steel"

The performance of the TLS turbulence model is examined for a more realistic geometry in this section. The absence of vertical walls reduces errors due to the hydrostatic pressure approximation. However, other uncertainties, caused by the complex geometry, are introduced. Despite rather detailed information on the bathymetry, after digitisation the bathymetry in the numerical model deviates from the physical model. This may have a significant influence on computed flow patterns. Furthermore, a curvilinear grid is used in order to represent land boundary as accurately as possible. In some regions occurrence of a so-called stair-case boundary cannot be avoided. It is known that this introduces computational errors. All computations were carried out on a grid consisting of 81×75 grid points, see Figure 4.12, of which about $2/3$ are active. The coordinate system referred to in the following section is also drawn in this figure. The positive x -axis is in the direction

of the flow in the river. In the vertical direction, 10 layers, distributed as in the previous case, were used.

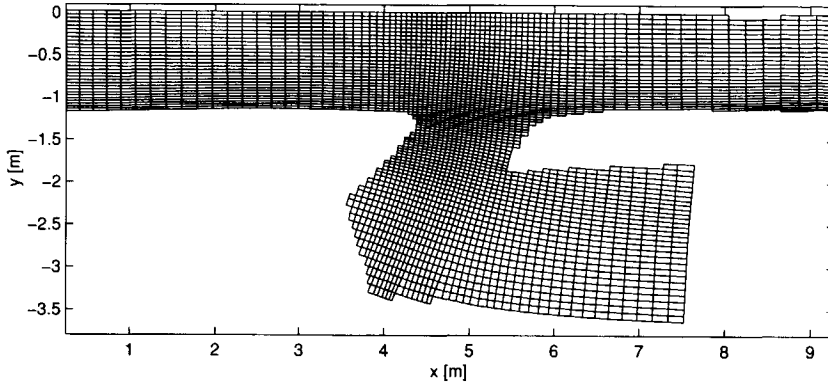


Figure 4.12: Computational grid of yacht harbour "t Steel".

4.3.1 Computational results

Computations for the yacht harbour were carried out with the LS-model and the TLS-model only; the DH-model with the constant horizontal eddy viscosity is left out of consideration.

In Figure 4.13 vector fields in the mixing layer at $\sigma = -0.075$ are compared with PTV data. Every second vector is plotted. Strictly speaking, this comparison is not correct since velocities from measurements are situated at $\sigma=0$. However, velocity gradients in the vertical direction are rather small near the free surface at most places and therefore comparison with PTV data is admissible. In the mixing layer the velocities obtained with the TLS-model and LS-model are quite different. Concluding from the isolines of the magnitude of velocity in Figure 4.13, the velocity gradients $\partial u/\partial y$ are lower in the mixing layer region in the LS-model. In contrast with the LS-model, which underestimates velocities in the mixing layer, the TLS-model predicts both magnitude and direction of the velocities rather accurately.

The better agreement of the computed velocities with the experimental data is related to the value of the computed Reynolds stresses in each of the models. These Reynolds stresses, and the Reynolds shear stresses in particular, account for the transfer of momentum across the mixing layer and are the driving forces responsible for the development of the gyres in the harbour entrance and the harbour itself. The correct representation of the Reynolds stresses is therefore an important criterion to judge the turbulence model by.

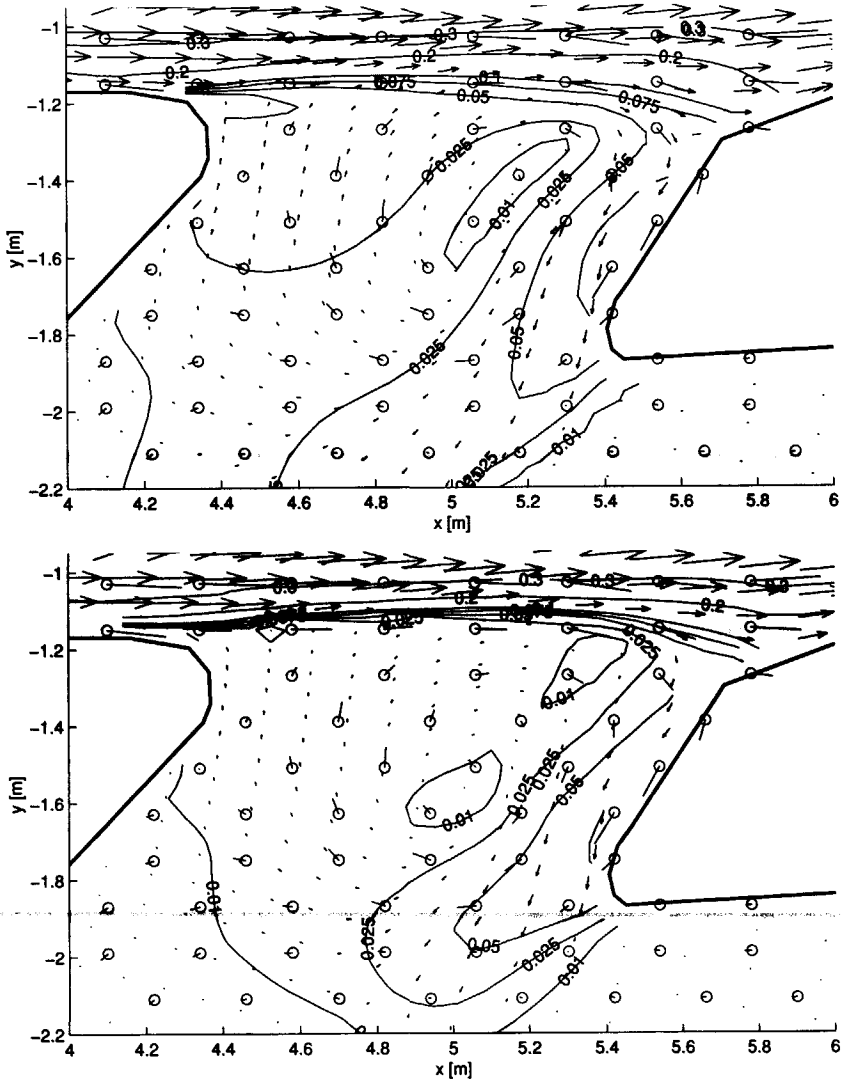


Figure 4.13: Computed velocity vector field (arrows) and measured velocity vector field obtained with PTV technique (circle/line) at the free surface. Isolines indicate the magnitude of the computed velocity vector in [m/s]. Upper figure: TLS-model, lower figure: LS-model.

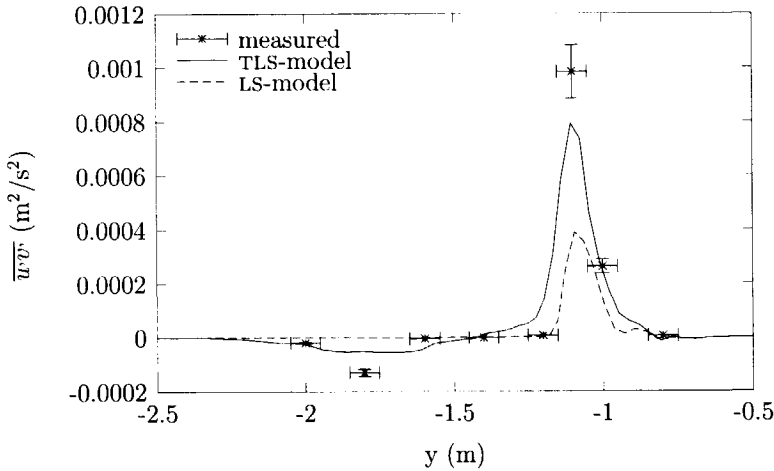


Figure 4.14: Reynolds shear stress per unit mass at $x=4.9$ m and $z=-0.05$ m.

In Figures 4.14-4.16 the computed horizontal Reynolds shear stresses per unit mass, $\overline{u'v'}$, at three transects (at $x = 4.9$ m, 5.15 m and 5.4 m) at a depth of 5 cm below the free water surface, are plotted together with measured Reynolds shear stresses. The "wiggles", for example at the river side of the large peak, are due to post-processing. The horizontal error bars indicate the possible errors involved in mapping the measured data to the computational grid, vertical error bars indicate a relative error in measuring turbulent stresses of 10% as pointed out previously (assuming that the relative error in measuring turbulent shear stresses is the same as in measuring normal stresses). The horizontal Reynolds shear stresses are in better agreement with measurements in the TLS-model than in the LS-model, although the measuring grid is too coarse to draw any definite conclusions about the correctness of the computed Reynolds stresses. The lower Reynolds stresses in the case of the standard model explain the underestimation of the velocities in the mixing layer.

At the transition from the primary gyre in the harbour entrance to the secondary gyre in the harbour basin, a secondary mixing layer develops. The velocity gradients in this mixing layer are much smaller than in the primary mixing layer and no large-scale turbulent structures were observed. Furthermore, the width of the secondary mixing layer is rather small causing the sample points to lie outside the mixing layer at $x = 5.15$ m and $x = 5.4$ m. This seems not to be the case at $x = 4.9$ m, yielding a larger peak value for the Reynolds stress than observed at the other two transects. This makes it difficult to judge the computed Reynolds shear stresses in the secondary mixing layer, although it can be

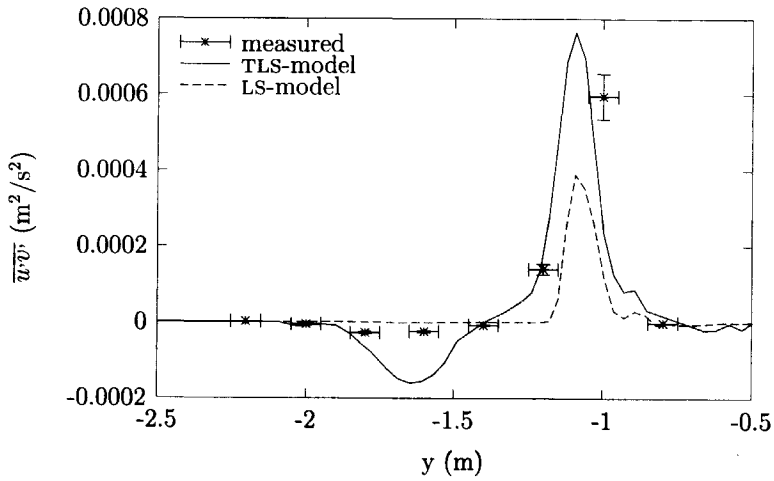


Figure 4.15: Reynolds shear stress per unit mass at $x=5.15$ m and $z=-0.05$ m.

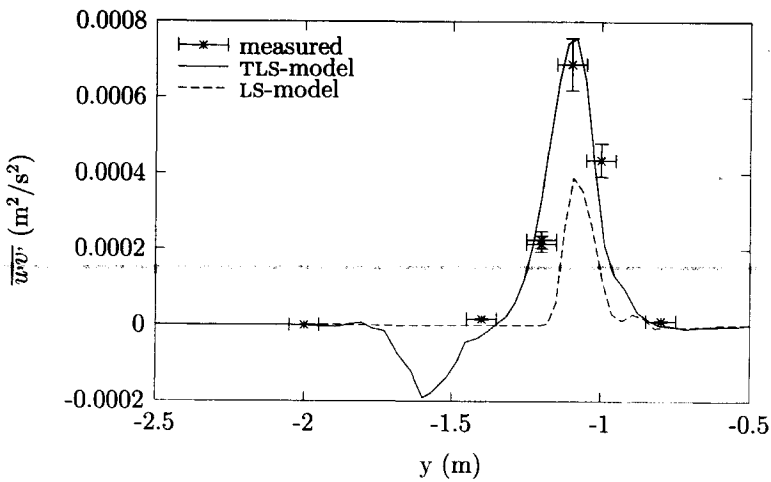


Figure 4.16: Reynolds shear stress per unit mass at $x=5.4$ m and $z=-0.05$ m.

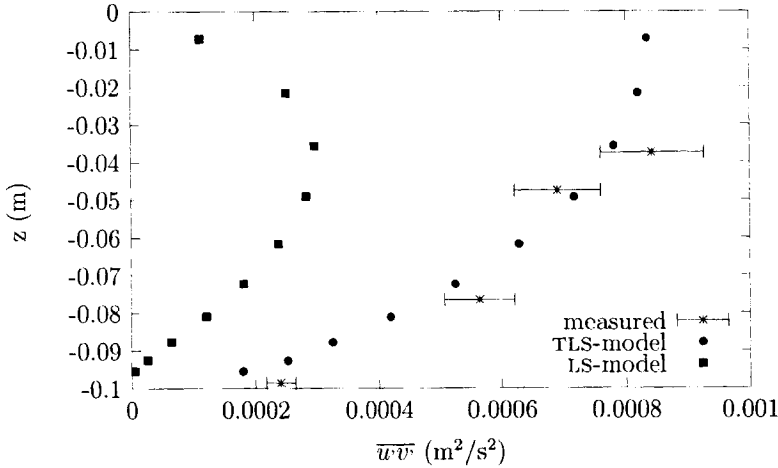


Figure 4.17: Reynolds shear stress per unit mass at $x=5.15$ m and $y=-1.1$ m as a function of depth z .

seen that the maximum stress is underestimated at $x = 4.9$ m.

The pancake-like quasi-two-dimensional turbulent structures that were observed yield horizontal Reynolds shear stresses that remain relatively large near the free surface, something that can also be found in the TLS-model but which is absent in the LS-model, see Figure 4.17. Towards the bottom there is a clear tendency of the stresses to decrease, indicating that the flow is not entirely 2D, as expected, which is also found in the computations.

Despite the good agreement of the TLS-model with measured velocities in the mixing layer, the computed velocities in the harbour entrance downstream of the stagnation point are underestimated significantly by both models. As a consequence, velocities in the secondary mixing layer have the same tendency. The local rather crude representation of the physical boundary line by a stair case grid may be the major cause of the underestimation of the velocities. It is known that such boundaries introduce additional friction and therefore decelerate the flow.

The underprediction of the velocities downstream of the stagnation point gives rise to discrepancies between the computed and measured Reynolds shear stresses in Figure 4.14. Ultimately, this affects the velocity in the remainder of the computational domain which can be seen to be too low. However, velocities have increased about 35% on average by applying the TLS turbulence model compared to the standard $k-\varepsilon$ turbulence model.

Finally, the computed horizontal eddy viscosity is given in Figure 4.18. Visual obser-

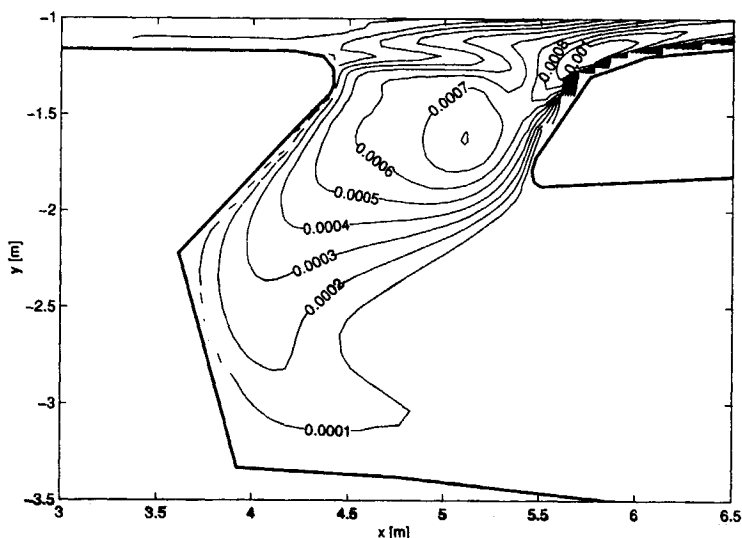


Figure 4.18: Computed horizontal eddy viscosity in $[m^2/s]$ with the TLS-model.

ations revealed that the large-scale turbulence no longer exists in the harbour region; the level of turbulence is very low and the turbulence is of a three-dimensional nature. The related Reynolds numbers are of the order of 1000, hence low-Reynolds turbulence models should be applied in this region. Consequently, the computed values of the eddy viscosity are too high in the harbour.

4.4 Discussion

The two-length-scale turbulence model (TLS), the single-length-scale k - ϵ model (DH) and the standard 3D k - ϵ model of Launder and Spalding (LS) are applied to unstratified shallow-water flows in which the horizontal turbulent transfer of momentum plays an important role.

Summarising the computational results for the square harbour, it can be stated that the flow in this case can be predicted reasonably well with all three turbulence models. However, in order to represent some details of the flow correctly, it is necessary to model the non-isotropic behaviour of the flow, reflected in the turbulence model used. This is the reason why the standard single-length-scale turbulence model fails to represent the shape of the mixing layer and the characteristic bulb in the vertical velocity profile near the stagnation point correctly. Both the constant horizontal eddy viscosity model and the

TLS model seem to be more suitable for predicting this type of flow than the standard $k-\varepsilon$ model. The disadvantage of the constant eddy viscosity to be prescribed by the user, which gives the model an empirical character, can be circumvented by using the TLS turbulence model. This is even more true when transient flows are considered or when choosing an eddy viscosity is a less trivial task. The predictive capabilities of the turbulence model increase by avoiding the empirical eddy viscosity, which is one of the advantages of this turbulence model.

Results from LDA- and PTV-experiments were used for further model testing in a more realistic geometry. It was shown that also in this geometry the standard $k-\varepsilon$ model underestimates the velocities in the mixing layer that develops between the river and harbour. Moreover, horizontal Reynolds shear stresses were predicted more correctly using the TLS turbulence model than with the standard $k-\varepsilon$ model. Especially near the free surface, where the eddy viscosity (and therewith the Reynolds stress) goes to zero in the case of the standard model, the TLS model yields horizontal Reynolds shear stresses that are in much better agreement with the measured quasi-two-dimensional turbulence.

In contrast with the square harbour, errors due to the hydrostatic pressure assumption were reduced in this situation, since the slopes of the model were much more gentle. However the complexity of the grid and bathymetry introduces additional errors, the importance of which is not clear at this moment. In this complex flow it is hard to distinguish those errors from the ones resulting from the imperfection of the turbulence model. In order to obtain more accurate results, it is expected that the grid should be refined in the vicinity of the stagnation point downstream of the primary mixing layer. The coarse representation of the boundary line locally enhances the resistance which locally results in smaller velocities and increasing velocity gradients at the closed boundary. Furthermore, turbulent intensities near the stagnation point that are determined with a $k-\varepsilon$ turbulence model are too high. Since the turbulence is transported into the harbour, the horizontal eddy viscosity in the harbour as computed by the depth-averaged $k-\varepsilon$ model is likely to be overestimated.

The computed flow field and horizontal turbulent shear stresses agree rather well with the measurements in the primary mixing layer, but results for both models are still unsatisfactory in the remaining areas of the computational domain which is partly a result of the above mentioned shortcomings. Qualitatively, the results of the TLS model are quite similar to the observations in the physical model; the position of the gyre and the stagnation points are predicted with sufficient accuracy. However, velocities in the secondary mixing layer, between the harbour entrance and the harbour itself, are underestimated considerably. Moreover, the direction of the flow deviates significantly from those observed in measurements in case of both the TLS and standard $k-\varepsilon$ turbulence model. The additional resistance near the stair-case boundary and the exaggeration of the eddy viscosity are believed to be the major factors. Errors introduced by the latter effect can be reduced by relating the production of turbulent kinetic energy not solely to the strain rate of the velocity field.

From the above it is clear that the TLS model needs further testing for different situations. Testing the model for the square harbour with a non-hydrostatic code can preclude any doubt about the influence of the violation of the hydrostatic pressure assumption, without losing the transparency of a relatively simple flow.

Testing the model for other relatively simple flows before applying it to real-life situations is recommended in order to gain insight into the model's limitations. Extension to stratified flows, in which the density interface can act as an internal boundary and thereby induce two-dimensionality, may also be desirable and is believed to be possible.

Chapter 5

Comparison of the σ - and z -coordinate model

In this chapter the effects of the vertical coordinate system on the computational results are studied ¹. The development of two numerical models that are based on identical numerical techniques and that only differ in the choice of the vertical coordinate system, allows for a sound comparison of numerical models that are based on different coordinate systems. The departures between the numerical results of the z -model and σ -model (which are described in Chapter 2) can therefore be attributed to the vertical coordinate system. Discrepancies due to the discretisation of the equations, the schematisation of the geometry or the turbulence model that is used are thus excluded as much as possible.

The implementation of both models is tested first by means of relatively simple two-dimensional test cases. For flows with uniform depth both models will be shown to yield consistent results. Subsequently, bathymetric variations are introduced to show the differences between the z -model and the σ -model. These test cases demonstrate the importance of the treatment of the bottom friction and horizontal advection in the z -model. Furthermore it is illustrated that the σ -model is preferred for modelling boundary layer flow.

Next, the numerical models are applied to two prototype situations. The Haringvliet estuary simulations show that only small discrepancies between the z -model and σ -model are encountered when applied to regions with relatively smooth topography. The Lake Veere simulations, on the other hand, show a strong dependence of the computational results on the vertical coordinate system employed. From the comparison of the computational results to field measurements it can be concluded that the z -model is more suitable in this specific test case. Finally, the importance of the orientation of the computational grid with respect to the local flow direction is substantiated by means of a schematised two-dimensional Lake Veere simulation.

¹This chapter is published in adapted form in Bijvelds *et al.* (1999b)

5.1 Model assessment using two-dimensional test cases

5.1.1 Steady channel flow

In order to judge the potential discrepancies between the models in complex situations, similarity of the models' results must be assured in the case of horizontal flow with constant depth. In that case the σ -model reduces to the z -model and the results should be identical. Frictionless flow leads to uniform depth but is not adequate for testing the models. Important features of the models, such as the turbulence model for example, cannot be tested in the absence of bottom friction. Therefore a stationary channel flow over a horizontal bottom is considered with a friction coefficient c_f of 3.25×10^{-6} . The related theoretical slope of the free surface can be obtained by reduction of the shallow-water equations. Assuming a steady uniform flow, which is a good approximation for small water surface gradients, the vertical viscosity term balances the barotropic pressure gradient:

$$\frac{\partial}{\partial z} \left(\nu_t \frac{\partial u}{\partial z} \right) = g \frac{\partial \zeta}{\partial x}. \quad (5.1)$$

After integration over the water depth, and using $u_* / \bar{u} = \sqrt{c_f}$ and $\tau_b = \rho u_*^2$, we get:

$$\frac{\partial \zeta}{\partial x} = -c_f \frac{\bar{u} |\bar{u}|}{gH}. \quad (5.2)$$

For the testing a 5000 m long and 10 m deep channel with a depth-mean flow velocity, \bar{u} , of 0.5 m/s is assumed. This yields a slope of about 8.3×10^{-6} or, equivalently, a maximum drop of the water level of 0.04 m.

Because of the small slope of the water surface, differences between the σ -model and the z -model can be expected to be negligible. This is confirmed by the computational results depicted in Figure 5.1, showing identical results for the z -model and σ -model. These results are obtained with a 25-layered model with variable grid spacing. The eddy viscosity is computed with the standard k - ε turbulence model described in section 2.3.3. In **Figure 5.1 no differences between the σ -model and the z -model can be observed** indicating a consistent implementation of the shallow-water equations and k - ε turbulence model in both models. The computed free surface slope agrees well with the theoretical one given by eq. (5.2) and the velocity and turbulent quantities are in agreement with values reported in the literature (Nezu & Nakagawa, 1993).

If instead of a horizontal bottom a (linearly) sloping bottom is assumed, differences between the σ -model and z -model are likely to appear. First of all the vertical grid spacing in the z -model and σ -model no longer coincide. More importantly, the z -model suffers from the stair-case representation of the bottom. This gives rise to a large variation of the vertical grid spacing. At some places the vertical grid spacing vanishes and as a consequence the bottom shear stress goes to infinity, see eq. (2.64). This is clearly shown in Figure 5.2.

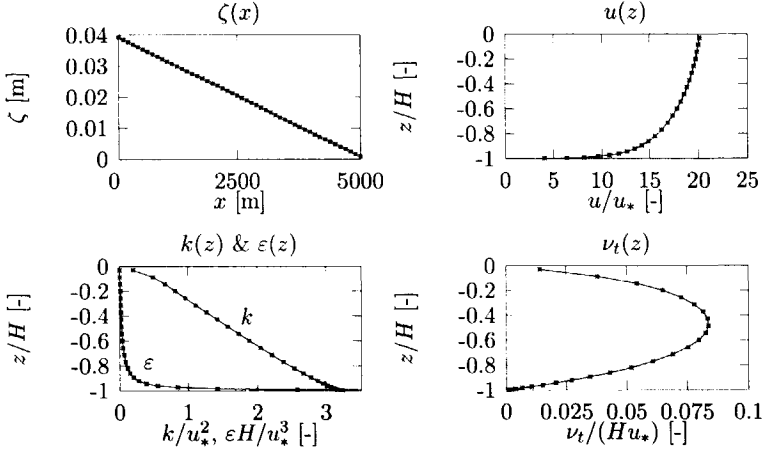


Figure 5.1: Free surface elevation as a function of space x and the non-dimensional velocity, turbulent kinetic energy k , dissipation rate ϵ and eddy viscosity ν_t^p as a function of depth for the z -model (solid lines) and the σ -model (dashed lines).

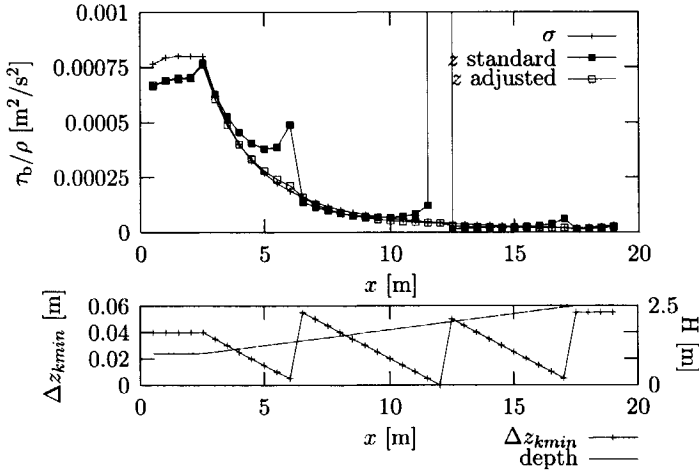


Figure 5.2: Upper panel: Computed bottom friction for the σ -model and the z -model. Lower panel: vertical grid spacing of the first grid cell above the bottom in the z -model as a function of x .

In this figure the bottom shear stress in the z -model is compared to the bed shear stress as computed with the σ -model. At places where the vertical grid spacing vanishes, large deviations between the bottom shear stress in the σ -model and z -model can be observed. These deviations can be reduced significantly by computing the bottom shear stress at $z = \frac{1}{2}(\Delta z_{kmin} + \Delta z_{kmin+1})$ instead of $z = \frac{1}{2}\Delta z_{kmin}$. The effect of this measure is indicated by "z adjusted" in Figure 5.2.

Besides the bottom shear stress, the implementation of the horizontal advection of momentum is very critical in the z -model in the presence of sloping bottoms. This aspect will be touched upon in section 5.1.4.

5.1.2 Standing wave

An important difference between the σ -model and the z -model is the treatment of the free surface. In the σ -model the numbers of layers is constant and the vertical excursion of the free surface does not impose additional problems. In the z -model on the other hand, the number of grid cells in vertical direction is not fixed, hence the free surface is allowed to travel through the fixed layers in the z -coordinate system. The problems related to this have been discussed in section 2.5.4.

The free surface treatment in the z -model is tested by means of a standing wave in a basin with a length of $L=500$ m and $H=10$ m. Inviscid flow is assumed in this test case. In Figure 5.3, the water surface elevation as a function of time and space are plotted. No significant differences between the models can be observed, indicating that the free surface is dealt with in a correct manner in the z -model. The computed period of the oscillation agrees well with the theoretical one, viz. $T = 2L/\sqrt{gH} \approx 100$ s. Note that the numerical models are subject to artificial damping due to the time integration method.

5.1.3 Exchange flow

The implementation of the baroclinic pressure gradient is examined for an exchange flow on a horizontal bed. A closed basin with length $L=500$ m and depth $H=10$ m is considered **which is divided into two areas with different concentrations of salt:**

$$c = \begin{cases} 0 & \text{if } 0 \leq x < \frac{L}{2} \\ 12 \text{ ppt} & \text{if } \frac{L}{2} \leq x \leq L. \end{cases} \quad (5.3)$$

This salinity distribution gives rise to a density difference of $\Delta\rho = \rho_2 - \rho_1 = 9.3 \text{ kg/m}^3$. The inherent baroclinic pressure gradients induce gravity currents at the bottom and the free surface; the heavier water tends to intrude under the less dense fluid resulting in two fronts moving in opposite directions, with the front speed u_f equal to the particle velocity. Besides, an external wave is generated, with very small amplitude compared to the water depth. The speed of the front of the gravity current can be deduced from considering

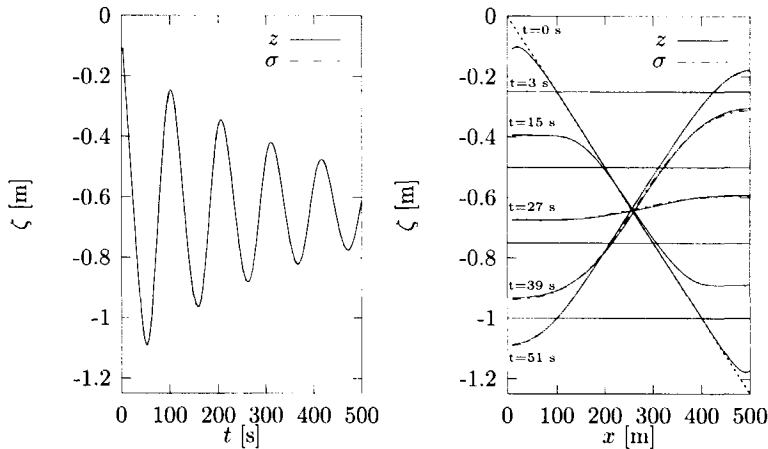


Figure 5.3: Water elevation ζ computed by the z -model and the σ -model as a function of time (left) and space (right). The monitoring station is positioned near $x=0$. Horizontal lines in the right figure indicate the predefined horizontal layers in the z -model.

the energy budget of the system. At $t=0$ the total amount of potential energy per unit volume is equal to $\frac{1}{2}gH(\rho_1 + \rho_2)$. Assuming a frictionless flow, with no mixing between the layers, the system must consist of two layers with different density and of equal thickness (the layer of lighter water (ρ_1), of course, overlays the layer of heavier water (ρ_2)). The potential energy per unit volume of the transient state equals $\frac{3}{4}gH\rho_1 + \frac{1}{4}gH\rho_2$. Because of conservation of energy, the net change in potential energy per unit volume, $\frac{1}{4}gH\Delta\rho$ must be equal to the total kinetic energy per unit volume, $\rho_0 u_f^2$, hence the front speed u_f is given by

$$u_f = \frac{1}{2} \sqrt{\frac{gH\Delta\rho}{\rho_0}}. \quad (5.4)$$

It is shown in (Kranenburg, 1982) that for frictionless exchange flow the celerity of the front is somewhat higher than given by eq. (5.4). According to eq. (5.4) the celerity of the front is equal to 0.48 m/s.

The external wave generated by the intruding current has an amplitude which is much smaller (by a factor $\Delta\rho/\rho_1$) than the amplitude of the internal wave. Therefore the z -model and σ -model should lead to very similar results. In Figure 5.4, velocity profiles and salinity distributions are plotted at four different times at $x=\frac{1}{4}L$. The front arrives at this position at the same time in both models and the "final" distribution (at $t=570$ s) of velocity and

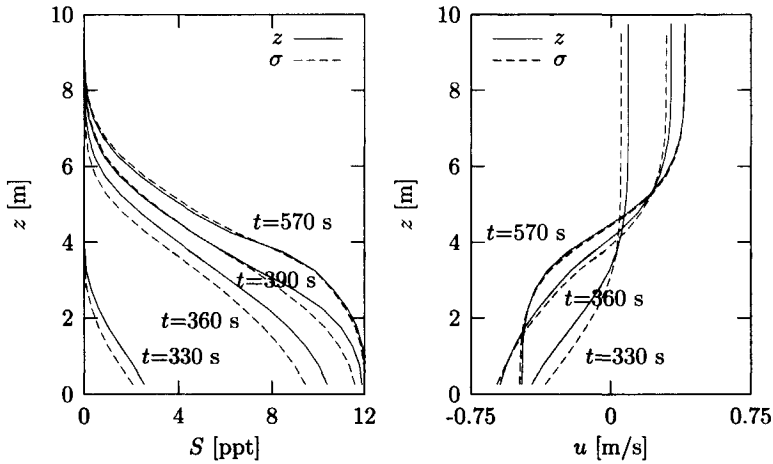


Figure 5.4: Salinity and horizontal velocity as a function of depth at $x = \frac{1}{4}L$ at four different times.

density are almost identical. Small differences can be observed at $t=330$ s, $t=360$ s and $t=390$ s. This may be due to the discretisation of the barotropic pressure gradient in the σ -model, eq. (2.71). In the case of zero depth gradient, this expression is equal to the baroclinic pressure gradient in the z -model and differences between the models vanish. However, near the front of the gravity current, gradients of the free surface elevation occur. The water level gradients are enhanced by assuming a hydrostatic pressure distribution. This may explain the differences observed in Figure 5.4.

The computed speed of the front is approximately 0.35 m/s, significantly lower than the theoretical front speed. This discrepancy can be attributed to the discretisation of the advective terms in the momentum equation. Although the continuous form of the shallow-water equation describes the conservation of momentum, this conservation property no longer holds in discrete form after applying eq. (2.57) for the advective terms. A conservative discretisation for $u\partial u/\partial x|_{i+1/2,j,k}$ for constant grid spacing Δx is given by (Stelling & Busnelli, 2000):

$$u\partial u/\partial x|_{i+1/2,j,k} \approx \max\left(0, \frac{\bar{q}_{i,j,k}}{\Delta z}\right) \frac{u_{i+1/2,j,k} - u_{i-1/2,j,k}}{\Delta x} + \min\left(\frac{\bar{q}_{i+1,j,k}}{\Delta z}\right) \frac{u_{i+3/2,j,k} - u_{i+1/2,j,k}}{\Delta x}, \quad (5.5)$$

where $\bar{q}_{i,j,k} = (u\Delta z)_{i+1/2,j,k} + (u\Delta z)_{i-1/2,j,k}$ and $\bar{\Delta z} = \Delta z_{i+1,j,k} + \Delta z_{i,j,k}$. The vertical advective terms are discretised in a similar way. Results are shown in Figure 5.5. This shows that the conservative approximation of the advection results in a significant increase of the front

speed. The celerity of the gravity current is approximately 0.45 m/s, only slightly lower than the theoretical value of 0.48 m/s. It is noted that retarding behaviour introduced by the non-conservative approximation of the horizontal advection cannot be circumvented by using higher-order upwind schemes.

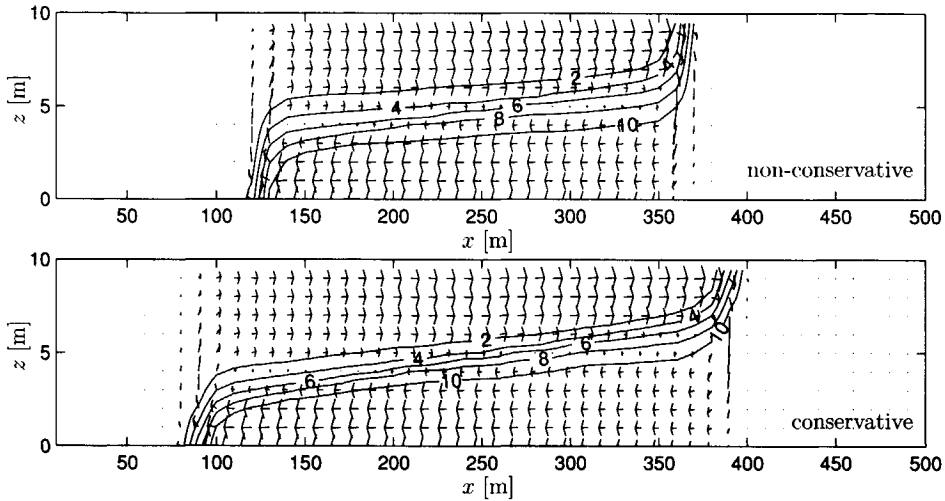


Figure 5.5: Isolines of salinity and velocity vector field at $t=360$ s. Upper panel: non-conservative approximation of advection, lower panel: conservative approximation of advection. The computational grid consists of 50×20 grid cells.

5.1.4 Buoyant plume on a sloping bottom

The section on the model assessment is finalised with a test case that can be looked upon as a simplification of a flow condition that may occur in estuaries. In these areas the topography consists of shallow regions which are crossed by channels and pits. During high tide these channels and pits are filled with saline water. This process of filling can be simplified as a boundary layer flow of negatively buoyant water on a sloping bed, as depicted in Figure 5.6.

First the flow is assumed to be inviscid. This is done to reveal the importance of the grid orientation in relation to the numerical diffusion of matter. After that, bottom friction and turbulent mixing are included in the simulations and results are compared to laboratory experiments.

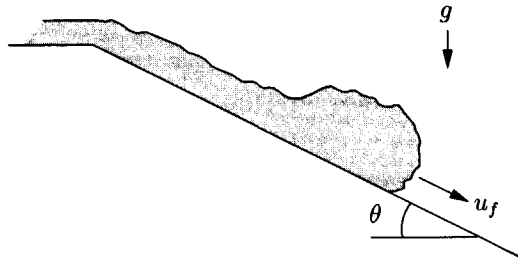


Figure 5.6: Schematic of buoyant plume with front speed u_f on a sloping bottom with angle θ .

In absence of friction the momentum equation reduces to the following expression which describes the acceleration of the front of a salt wedge:

$$\frac{du_f^2 h_f}{dx} = g' h_f \sin \theta, \quad (5.6)$$

where g' is the reduced gravity $\Delta\rho/\rho g$ and h_f is the height of the front of the salt wedge. Although an analytical solution can be constructed for flows with constant layer thickness h_f , it is hard to compare numerical results to the analytical solution. This is due to the assumption of constant layer thickness of the salt wedge which cannot be satisfied in the numerical models. Therefore results are compared to a reference solution obtained with the z -model using a high resolution grid of 320x100 grid points. These results of the z -model are obtained after a small adjustment of the original code, related to the approximation of the horizontal advection terms.

Before proceeding with the presentation of the results the treatment of the horizontal advection near boundaries is addressed first. As mentioned in section 2.5.4, horizontal advection must be neglected near the wall in the case the flow is directed from this wall. The effect of this measure is illustrated in Figure 5.7 which shows the vertical velocity profiles of horizontal velocity at a certain position on the slope. In the absence of bottom friction the largest velocities are expected to occur near the bottom, as predicted by the σ -model. A similar profile is obtained with the z -model after the neglect of the horizontal advection near walls if the flow is directed from the wall. If the standard discretisation of the advection of momentum near the wall is used, a deceleration of the flow and hence a reduction of the front speed is observed. Note that the wiggles are due to the assumption of inviscid flow; addition of some viscosity will suppress these oscillations.

In Figure 5.8 the position of the front of the salt wedge along the slope is plotted as a function of time. The reference solution, obtained with the z -model consisting of 320x100 grid points, is indicated by z -ref. The same front speed is computed with the σ -model using

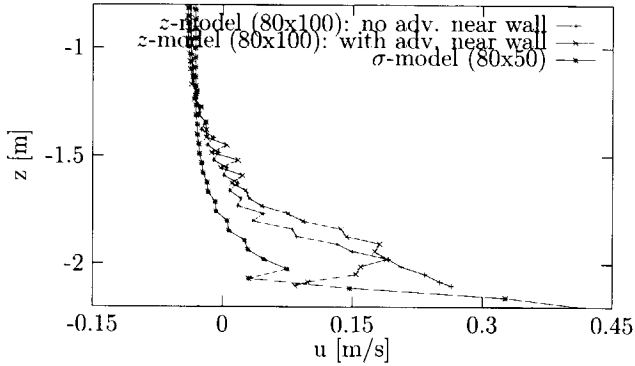


Figure 5.7: Characteristic vertical velocity profiles of a gravity current on a sloping bottom; z -model with inclusion of the horizontal advection near closed boundaries, the z -model without inclusion of the horizontal advection near closed boundaries and the σ -model.

only 80×50 grid points² (σ SVK in Figure 5.8). The reason for this can be attributed to the fact that the σ -model is superior to the z -model in the case of boundary layer flow on sloping bottoms. This is related to the fact that the flow as well as the grid of the σ -model are boundary fitted and have therefore the same orientation. A grid layer in the σ -model can therefore be considered as a stream tube. Consequently, vertical transport is small in this coordinate system and does therefore not add much to the numerical diffusion of matter.

The effect of the treatment of the horizontal pressure gradient in the σ -model is also shown in this figure. The results indicated with standard σ -model are obtained by computing the pressure gradient along σ -planes. The other two solutions are obtained by application of the Stelling and Van Kester procedure for the pressure gradient. Both the original filter (σ SVK) and the extended filter (σ SVK modified) have been applied. Clearly, the approximation of the horizontal pressure gradient introduced by Stelling and Van Kester is in better agreement with the reference solution than the standard σ -model. The extension of the filter seems to have negligible effect on the front speed in this case.

The solution of the z -model is dominated by numerical diffusion if the number of horizontal grid cells is taken equal to 80. The strictly horizontal orientation of the layers in the z -model forces the flow to cross the grid in both the horizontal and the vertical direction. This results in significant numerical diffusion as can be seen from the z -model

²It is stressed again that doubling the number of grid points in vertical direction in the z -model does not necessarily imply a doubling of the computational effort. A large number of grid cells are not active during computation due to the definition of the grid.

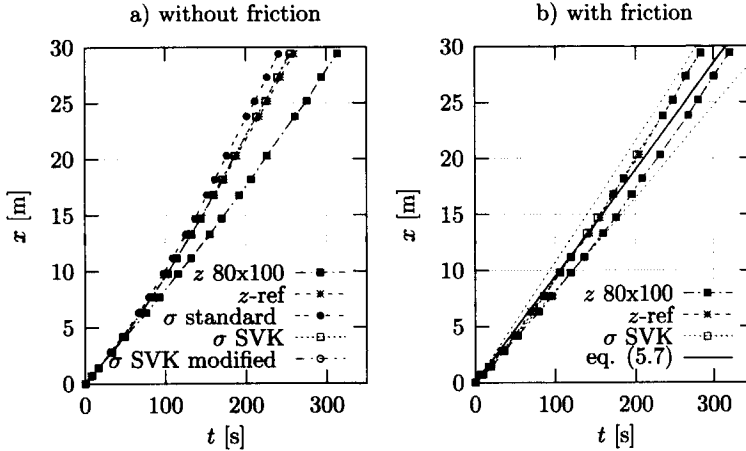


Figure 5.8: Position of the salt wedge front as a function of time. $Re \approx 15000$, $\theta = 5^\circ$.

results on an 80×100 grid. The numerical diffusion causes a reduction of the horizontal density gradients and hence the baroclinic force. This is brought out clearly by the lagging front in Figure 5.8. This conclusion is supported by the vertical velocity profiles depicted in Figure 5.7. The σ -model approach leads to higher velocities near the bottom and exhibits larger velocity gradients in the vertical direction.

Including the effects of bottom friction and turbulent mixing has a retarding effect on the front propagation. Density gradients are diminished by the mixing and thereby the driving force is reduced. From measurements (Britter & Linden, 1980) it was found that the front speed of gravity currents is constant on slopes larger than or equal to 5 degrees, provided that the Reynolds number $Re = (g'q)^{1/3} h_f / \nu$ is sufficiently large (q is the discharge per unit width). Acceleration due to gravity is balanced by bottom friction and entrainment of the ambient fluid. Under these conditions the front speed is given by:

$$\frac{u_f}{(g'q)^{1/3}} = 1.5 \pm 0.2, \quad (5.7)$$

where $(g'q)^{1/3}$ is the buoyancy flux. This relation is plotted in Figure 5.8b together with the numerical results. The upper and lower limits of eq. (5.7) are depicted by the dashed lines.

In the numerical simulations effects of turbulence are accounted for using the 3D k - ϵ turbulence model. As in the inviscid case, the σ -model yields results that are similar to the reference z -model by using only a quarter of the grid points in the horizontal direction. For these models, *i.e.* the σ -model and the reference solution of the z -model, the results

are in reasonably good agreement with the experiments, although some acceleration of the front can be observed which is in contrast with the measurements.

The solution of the coarse z -model (80x100 grid points) is dominated by numerical diffusion. This is deduced from the fact that hardly any difference regarding the front speed can be observed between the viscous and inviscid case.

The importance of the artificial mixing in the z -model is illustrated most clearly in the following simple test case. Consider a hypothetical flow field which is determined by continuity only, *i.e.*

$$u(x) = \bar{u}(x) = \frac{Q}{BH(x)}, \quad (5.8)$$

where Q is the discharge and B is the width of the domain. The bathymetry is drawn in Figure 5.9 a). A constant concentration of a neutrally buoyant constituent is imposed at the inflow boundary over a part of the depth. The concentration of the constituent c_2 is equal to $10/\text{m}^3$, the concentration of the surrounding water is equal to zero.

For this particular case the vertical transformed velocities ω in the σ -model are equal to zero and do not contribute to the transport of the constituent. As expected the σ -model converges to the analytical solution at steady state, see Figure 5.9 a). The z -model on the other hand, exhibits significant numerical diffusion. The vertical velocities, which are due to the deepening of the domain, give rise to vertical transport of matter between the horizontal layers in the z -model. This is accompanied by numerical diffusion which can only be reduced by using higher order transport schemes or by increasing the resolution of the grid.

To demonstrate the effect of using a higher order transport scheme, the first order upwind scheme for vertical transport of matter was replaced by the Van Leer II scheme for this particular test case, see Figure 5.9 a). Although this scheme is not applied in the remainder of the test case in this thesis, it is noted that the use of explicit transport schemes for the vertical advection in the z -model is feasible since the vertical grid spacing does not vanish in shallow areas, provided that a lower bound on the vertical grid spacing near the bottom is applied.

The σ -model may also suffer from this type of artificial diffusion. For example in estuaries, channels and pits may be filled with salt water at low tide while the upper part of the water column is occupied with fresh water due to a river discharge. Due to this stratification the flow in the upper part of the water column may have a (near) horizontal orientation and does not tend to follow the bottom topography. Consequently, the flow will cross lines of constant σ and thereby introduce artificial vertical diffusion. The diffusive effect in the σ -model in the case of strictly horizontal flow in regions with variable depth, can be demonstrated most easily if depth variations are accounted for by means of distortion of the grid, see Figure 5.9 b). In correspondence with the previous example, a uniform flow is imposed at the left boundary and a neutrally buoyant constituent is released in the

model over a part of depth. It is clear that for this situation the z -model is superior to the σ -model.

Although obscured by other phenomena, the diffusive behaviour of the z -model and σ -model can also be observed in practical situations, see section 5.3.

5.1.5 Summary of the model assessment results

Based on the foregoing numerical experiments, optimised configurations of the z -model and σ -model were determined for the 3D practical applications, described in the following section. For clarity the proposed adjustments to either the σ - or z -model are summarised:

- Advection.

The horizontal advection term in the z -model is neglected near solid boundaries if the velocity is directed from the closed boundary. This prevents the generation of an artificial boundary layer (artificial friction) and is necessary for the proper modelling of boundary layer type flow with the z -model. A non-conservative method is applied in the remainder of this thesis for the discretisation of the advective terms.

- Bottom friction.

The bottom shear stress is computed at $k+\frac{1}{2}$ by averaging the vertical grid spacing and horizontal velocity of layer k and $k+1$. This suppresses unphysically large variations of the bottom stress in the z -model.

- Baroclinic pressure gradient and horizontal diffusion.

The baroclinic pressure gradient and horizontal diffusion are based on strictly horizontal gradients by application of the Stelling and Van Kester method. This method guarantees finite vertical diffusion and positivity without being restricted to hydrostatically consistent situations, *i.e.* grids with a large ratio of horizontal and vertical grid spacing. The standard method of Stelling and Van Kester is applied; the extension of the standard filter to prevent systematic underestimation of the horizontal gradients has not shown to alter the results significantly for the example considered.

5.2 Haringvliet estuary

The Haringvliet estuary is situated in the south-west of the Netherlands, see Figure 5.10. Several decades ago a large part was cut off from tidal influence. The construction of a dam and sluices, which forms part of the so-called Delta works, has led to the reduction of the tidal amplitude from 2 meters to approximately 25 centimeter. Obviously, this change in hydrodynamics has had a large impact on the local environment. After the construction of the dam the ecology and the quality of the bottom deteriorated due to deposition of

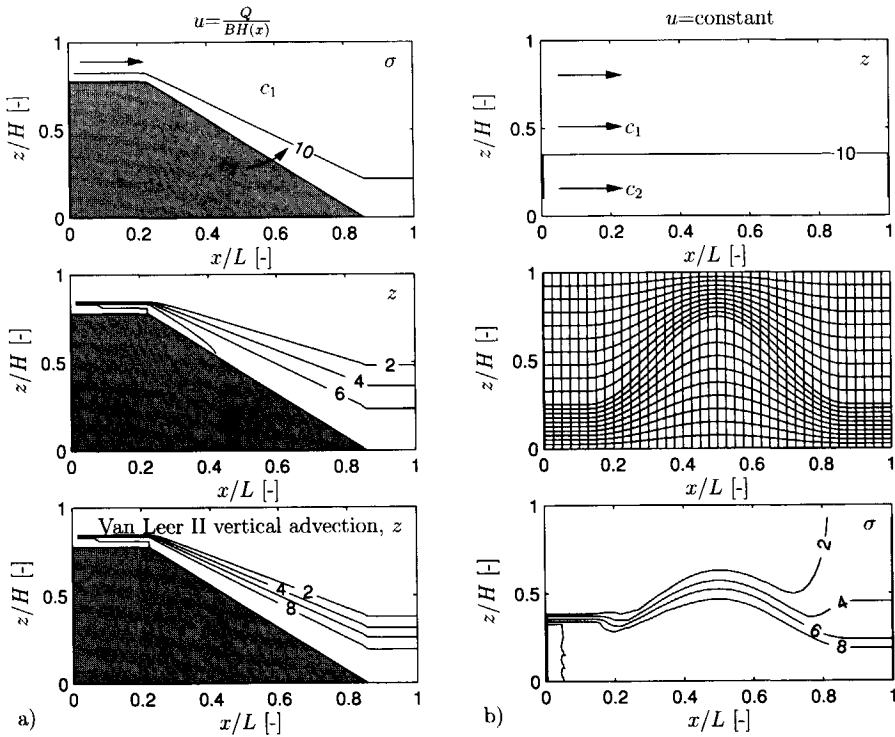


Figure 5.9: a) Isolines of computed concentration at steady state in the σ -model, z -model and modified z -model (Van Leer II instead of first order upwind for vertical advective transport) imposing $u = Q/(BH(x))$. b) Isolines of computed concentration at steady state in the z -model and σ -model in case of strictly horizontal flow in a region with variable depth. The variation of depth is schematised by distortion of the grid in the σ -model.

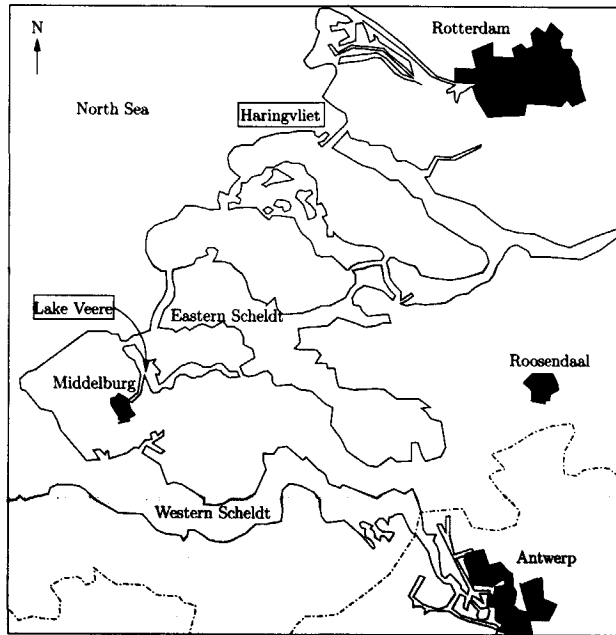


Figure 5.10: Geographic position of the Haringvliet estuary and Lake Veere.

polluted fluvial fine sediment. Induced by a changing view with respect to the environment, plans have risen to partly reopen the dam by changing the opening regime of the sluices.

To assess the effects of the changing sluice regime on the hydrodynamics in the estuary, numerical models may be used. Obviously, the incorporation of the sluices in the numerical models is then imperative. However, the effects of sluices are not implemented in the present models and are therefore disregarded. Since no field measurements are available, the model results are used for intercomparison of both model approaches only. The exclusion of the sluices in the schematisation of the estuary is therefore of minor importance.

5.2.1 Model input

Bathymetry and computational grid

The Haringvliet topography, depicted in Figure 5.11, can be roughly divided into two parts. At the sea-side of the sluices, the estuary is relatively shallow and a part of this region dries during low tide. At the other side of the sluices, the shallow areas are crossed by a system of channels. Moreover, some very deep pits (up to 35 m) occur in this area. It is

the latter region that makes comparison of the models of interest. The bathymetry of the Haringvliet model is shown in Figure 5.11. Note that although the sluices themselves are left out of consideration in the numerical calculations, the sill of the sluices is incorporated in the bathymetry.

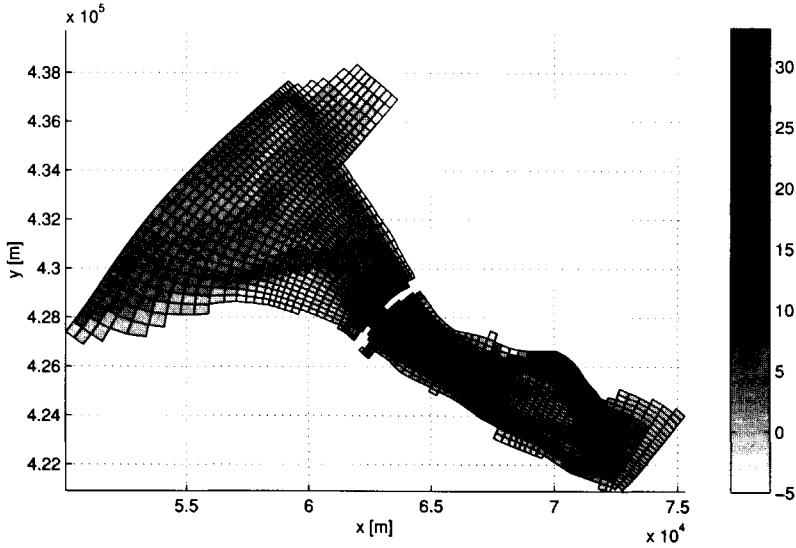


Figure 5.11: Bathymetry and computational grid of the Haringvliet estuary model (depth in m). Every second grid line is plotted.

The horizontal computational grid is equal to the detailed MOHA ("Monding Haringvliet") model of RWS/RIKZ (5.11), which consists of 149×100 grid points. A typical grid spacing $\sqrt{\Delta x \Delta y}$ varies from approximately 250 m near the open boundary at the North Sea to approximately 50 m near the sluices.

The vertical grid for the σ -model consists of 8 equidistant layers. From a convergence study carried out by RWS/RIKZ (Zijlema, 1999), it was concluded that 8 layers in the σ -model was sufficient to obtain a sufficiently accurate solution. A larger number of layers is required in the z -model than in the σ -model in order to have sufficient resolution in shallow areas. This resolution is needed to resolve the vertical salinity profiles due to the gravitational circulation. Using a 16-layered non-equidistant grid, the computational effort only increased slightly compared to the σ -model runs.

Boundary and initial conditions

The open boundary conditions at the sea side of the model consists of Neumann boundary conditions prescribing the free surface elevation and the salinity. At the river side of the model discharge and the salinity are imposed. The time series for these boundary conditions are derived from the "Zeedelta" model of RWS/RIKZ. These boundary conditions are depicted in Figure 5.12 for the time frame which is used for the presentation of the computational results. Near solid walls, no-slip conditions are imposed. Simulations are started assuming a stagnant water body with zero salinity.

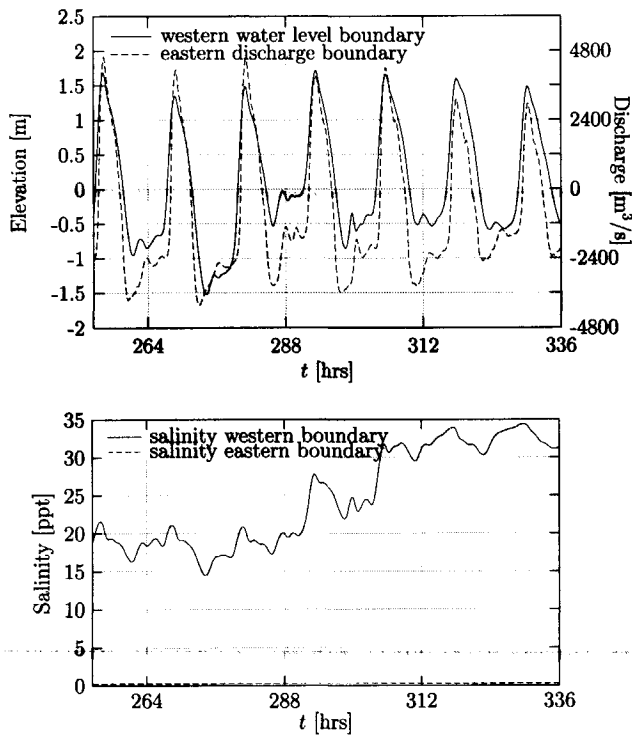


Figure 5.12: Open boundary conditions for the Haringvliet estuary model: Average water level at the western boundary and the total discharge at the eastern boundary (upper panel) and the salinity at the western and eastern boundary (lower panel). Note that the salinity at the eastern boundary is nearly zero.

Numerical and physical parameters

The simulation concerns a period of approximately 10.5 days. The time step is restricted by the stability criterion related to the horizontal advection and is equal to 15 s in the z -model and σ -model. The horizontal eddy viscosity and eddy diffusivity are both set equal to $1 \text{ m}^2/\text{s}$. The vertical eddy viscosity and diffusivity are computed by means of the k - ε turbulence model presented in section 2.3.3. The bottom roughness, expressed by Manning's coefficient, varies from $0.015 \text{ m}^{-1/3}\text{s}$ to $0.02 \text{ m}^{-1/3}\text{s}$ throughout the domain.

5.2.2 Computational results

Since no data from measurements are available for comparison with model results, the latter can only be used for intercomparison of the models. Differences between the models turned out to be minor and results of the Haringvliet simulations are therefore discussed briefly. The presentation of results is restricted to some of the characteristics of the hydrodynamics. A more extensive presentation of computational results can be found in (Bijvelds, 1999).

Since the water level is imposed at one of the model boundaries, it is expected that only small differences arise between the z -model and σ -model concerning the free surface elevation. This is confirmed by Figure 5.13 where the free surface elevation is plotted at a position near the sluices.

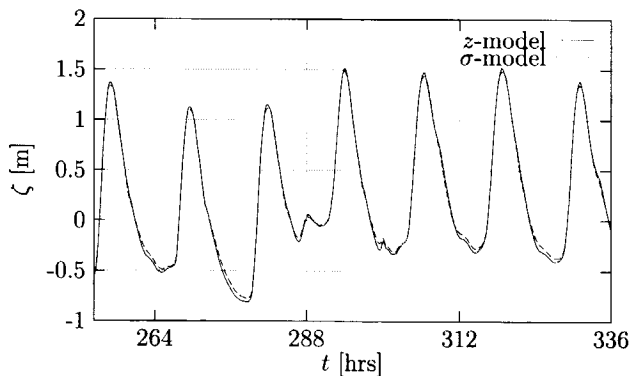


Figure 5.13: Characteristic free surface elevation as a function of time computed with the z -model and σ -model. Monitoring station is situated just seaward of the sluices.

In addition to the free surface elevation, the salinity shows very close agreement between the two models. In Figure 5.14 the horizontal salinity distribution is given around high tide at $t=319$ hrs. To obtain the salinity distribution of the σ -model at a constant z -level, variables are interpolated linearly. It can be seen that the salt wedge hardly travels further

than the sill of the sluices. Some differences between the z -model and σ -model may be observed near the front of the intruding salt wedge.

Seaward of the sluices the water body is fully mixed during almost the entire tidal cycle. Stratified conditions prevail at the river side of the sluices only, see Figure 5.15. This is related to the maximum intrusion length of the salt wedge, which just reaches this position at high tide. Furthermore, Figure 5.15 shows that the departures between the z -model and σ -model are rather small during most periods of the simulation.

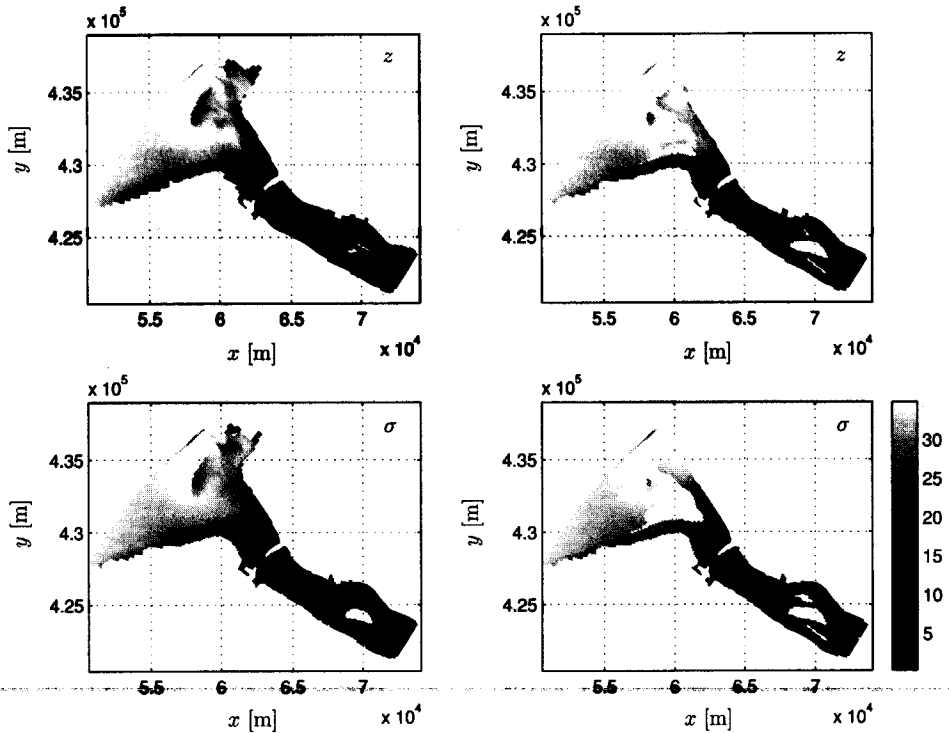


Figure 5.14: Horizontal distribution of salinity (in ppt) around high tide at $t=319$ hrs at $z = -1$ m (left) and $z = -3.5$ m (right). Results are obtained with the z -model (upper panels) and σ -model (lower panels).

It can be concluded that the σ -model and z -model yield results that are very similar for the Haringvliet estuary simulations. The inherent differences between the z -model approach and σ -model approach seem negligible in this particular case, hence they hardly

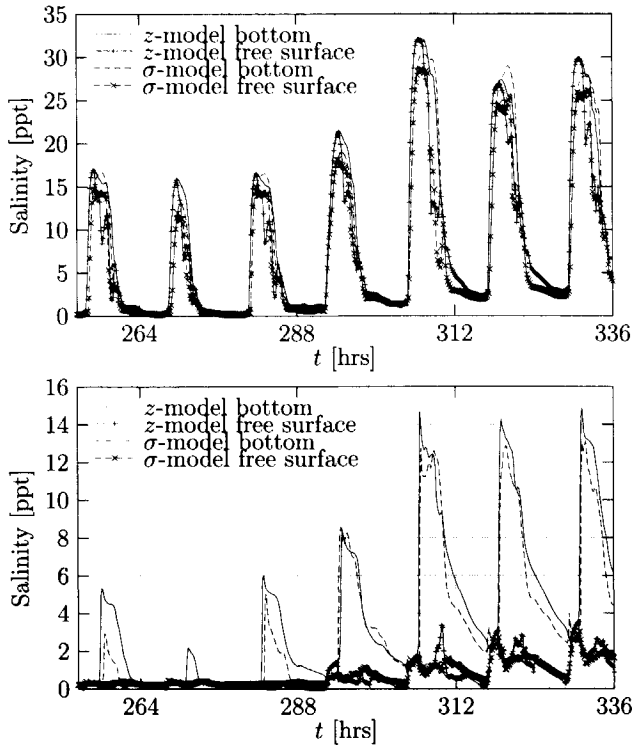


Figure 5.15: Time series of salinity in the Haringvliet estuary near the bottom and the free surface at a position halfway between the western open boundary and the sluices (upper panel) and near the sluices at the river side (lower panel).

affect the computational results. This may be explained by the fact that the salt wedge hardly reaches further than the dam and therefore mainly travels through a region with smooth topography. In these regions both models behave much alike as shown in the section on the model assessment.

5.3 Lake Veere

Lake Veere was formed in the early 60's due to the implementation of the Delta works. This water body lost direct connection with the Eastern Scheldt and the North Sea and has become isolated, see Figure 5.10. Sluices at the eastern side of the lake provide the only

connection with the Eastern Scheldt. Nowadays, the hydrodynamics in the lake is mainly controlled by wind forcing and baroclinic forcing. The latter is due to the discharge of water from the Eastern Scheldt via the sluices into the lake. These discharges consist of fresh water stemming from the surrounding canals, and salt water stemming mainly from the Eastern Scheldt. The difference in salinity and the temperature of the various discharges impose density gradients and thus baroclinic forcing. The related gravity currents are most notable during the period of water level set-up at the end of March. In order to assure sufficient navigable depth during the summer time, salt water from the Eastern Scheldt is let into the lake during a 10-day period to increase the water level, see Figure 5.16.

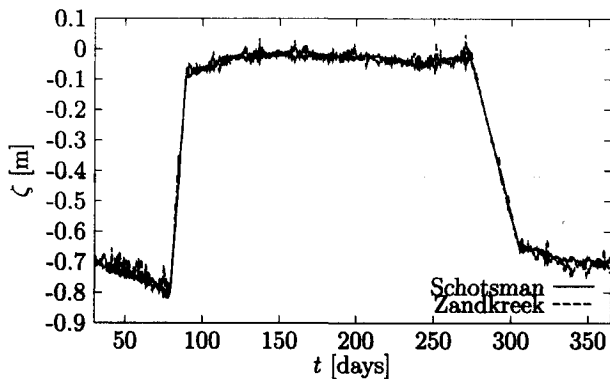


Figure 5.16: Computed free surface elevation in Lake Veere as a function of time at two remote monitoring stations. Results are obtained with the z -model.

Although Lake Veere is not subject to tidal variation and cannot therefore be classified as an estuary, it possesses many features that are subject of study in this thesis. As can be seen from Figure 5.17, the bathymetry of the lake exhibits strong variation of the depth. **The mean depth of the lake varies from 1 meter in the shallow areas up to 20 meters in some of the pits.** In combination with stratification in the lake and due to the absence of tidal forcing, the present test case may bring out discrepancies between the model approaches.

In the following the model input and the results of the simulations with the z -model and the σ -model are discussed and results are compared with field measurements. It is noted that within the σ -model the original anti-creep approach of Stelling and Van Kester (see section 2.5.3) for the computation of the horizontal baroclinic pressure gradient and horizontal diffusion is used.

5.3.1 Model input

Computational grid

The horizontal computational grid of the 3D model of Lake Veere consists of 116×9 grid cells, see Figure 5.17. In the z -model 30 layers are prescribed with decreasing grid spacing towards the free surface. This provides sufficient resolution in shallow areas to resolve vertical profiles of velocity and salinity. In the σ -model 20 equidistant layers are used. Due to the large bathymetric variation only 30 % of the grid points are active in the z -model. This means that less grid cells are involved in the computation than in the σ -model.

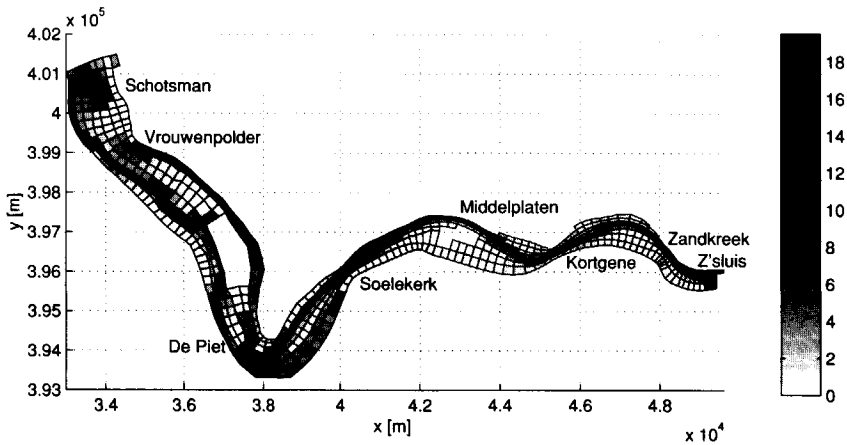


Figure 5.17: Bathymetry and computational grid of Lake Veere (depth in m). Approximate locations of the monitoring stations are indicated by the various names. Measured depth values have been reduced with 15% to represent the correct volume of the lake.

Numerical and physical parameters

The simulation starts at January 30 1995 0.00 hrs. and ends at December 31 1995 0.00 hrs. The time step is restricted by the stability condition imposed by internal wave propagation and is equal to 60 s. The CFL-number related to free surface waves is typically of the order 10.

The 3D eddy viscosity and diffusivity are computed by means of the standard k - ϵ turbulence model of section 2.3.3. The horizontal eddy diffusivity was set equal to $1 \text{ m}^2/\text{s}$. By increasing the horizontal background diffusivity the results appeared to be hardly

sensitive to this parameter. The bottom friction is computed with a Chézy coefficient which is constant in time and space and is equal to $65 \text{ m}^{1/2}/\text{s}$.

Initial conditions

The absence of predominant external forcing causes the initial conditions of the Lake Veere simulation to be of great importance. Therefore the simulations are started at January 30, which is the first date for which measurements of salinity and temperature are available. In Figure 5.18, vertical profiles of salinity are shown at January 30. It can be seen that the initial conditions deviate slightly from the measured salinity profiles at some of the monitoring stations. These departures are hardly of any significance given the uncertainty of the remainder of the model input (see section 5.3.2).

At the beginning of the simulations a stagnant water body is assumed.

Discharges

The discharges in the lake are important with respect to the amount of stratification during the year since it affects the salinity and water temperature. These discharges consist of water sluiced into the lake from surrounding canals, precipitation and exchange of water between the Eastern Scheldt and Lake Veere. The latter is mainly due to the locking of ships and the water level set-up and has a significant contribution in the build-up of salt stratification.

To account for the exchange of water near the sluices, both withdrawal of water and discharge of water must be included in the model. Salt water is discharged near the bottom of the model while the withdrawal takes place at the free surface at the same horizontal position. The proximity of these discharges may give rise to recirculation and can thus influence the total amount of salt entering the lake. During the discussion of the results this will be addressed.

Although some data were available on the salinity of the various discharges, information on the temperature was lacking. Therefore a characteristic distribution of the temperature during the year is assumed for all discharges.

Wind shear stress

The wind velocity was obtained from measurements at four different locations in the vicinity of the lake. To account for the retarding influence of the land on the wind speed, a reduction of 30 % was applied to the actual wind speed data. The drag coefficient is taken constant, equal to 0.00125.

Temperature modelling

The incoming radiation (in W/m^2) is based on measured solar radiation and includes the short wave radiation due to the sun as well as the long wave radiation due to the atmosphere and clouds. The loss terms in eq. (2.10) are computed on the basis of wind speed, air temperature, cloudiness and saturation of the air.

5.3.2 Computational results

In the following computational results are compared to the measured salinity distribution. Although measurements of temperature are available, only vertical profiles of salinity are considered. The simulations indicated that the vertical temperature distribution is mainly determined by solar radiation which is constant throughout the model and therefore hardly contributes to the horizontal density gradients.

In 1995 vertical profiles of salinity have been measured at ten different times during this year. The related monitoring stations and their approximate positions in the lake are indicated in Figure 5.17. Results are presented at three times during the year (January 30, June 20 and December 7) which are believed to be characteristic for the performance of the models. Note that the first date is the starting time of the simulations and indicate the initial conditions. No measurements of turbulent quantities or mean flow quantities are available.

In Figures 5.18-5.19 the vertical profiles of salinity are plotted at the various monitoring stations at the above mentioned dates. Due to wind-induced flow, well-mixed conditions prevail at the majority of the monitoring stations at January 30. Despite this wind action the stratification near the sluice is maintained. This is due to the inflow of salt water from the Eastern Scheldt at the sluices.

The effect of the water-level set-up at the end of March can clearly be discerned from the vertical profiles of salinity at June 20. The salinity near the bottom has increased considerably and most of the monitoring stations exhibit stratification. The low wind velocities during the summer do not provide sufficient energy to sustain fully mixed conditions. Qualitatively, this process is reproduced well by the z -model. It seems, however, that the salt wedge in the z -model lags behind compared to the measurements. Furthermore, the position of the salinity interface deviates from the measurements at most positions. The latter can partly be explained by considering the time series of salt at a certain position. In Figure 5.21, time series are plotted of salinity at various elevations at "Zandkreek". It can be deduced from this figure that large fluctuations of salinity are present between the free surface and $z = 6$ m. This is caused by the fluctuating wind speed and wind direction. A departure from the measurements concerning the position of the salt interface is therefore not surprising.

The poor representation of the near-field processes near the sluices is likely to contribute to the lagging of the salt wedge. These small-scale processes are of great importance for

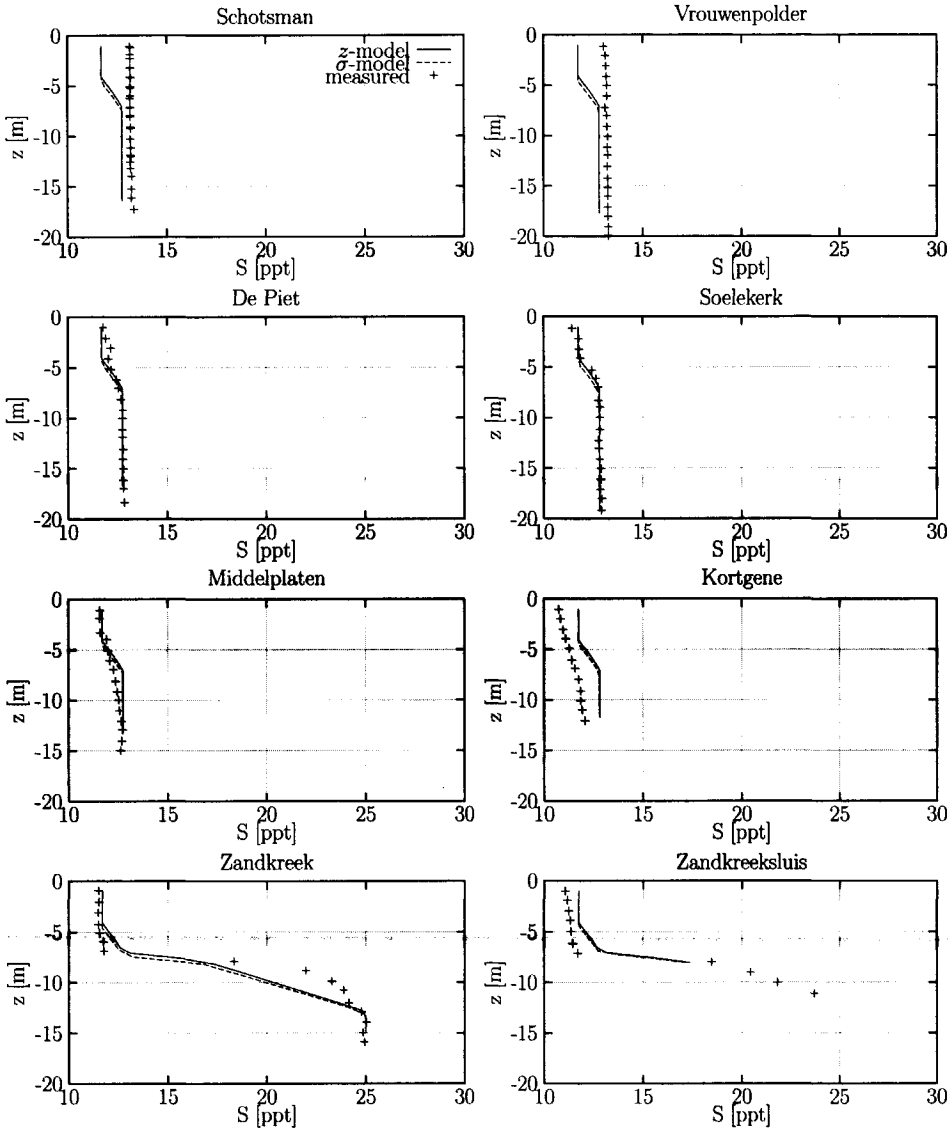


Figure 5.18: Initial conditions in the z -model and σ -model based on the measured salinity at January 30 1995. Solid line: z -model, dashed line: σ -model with anti-creep, +: measurements. For the approximate positions of the monitoring stations see Figure 5.17.

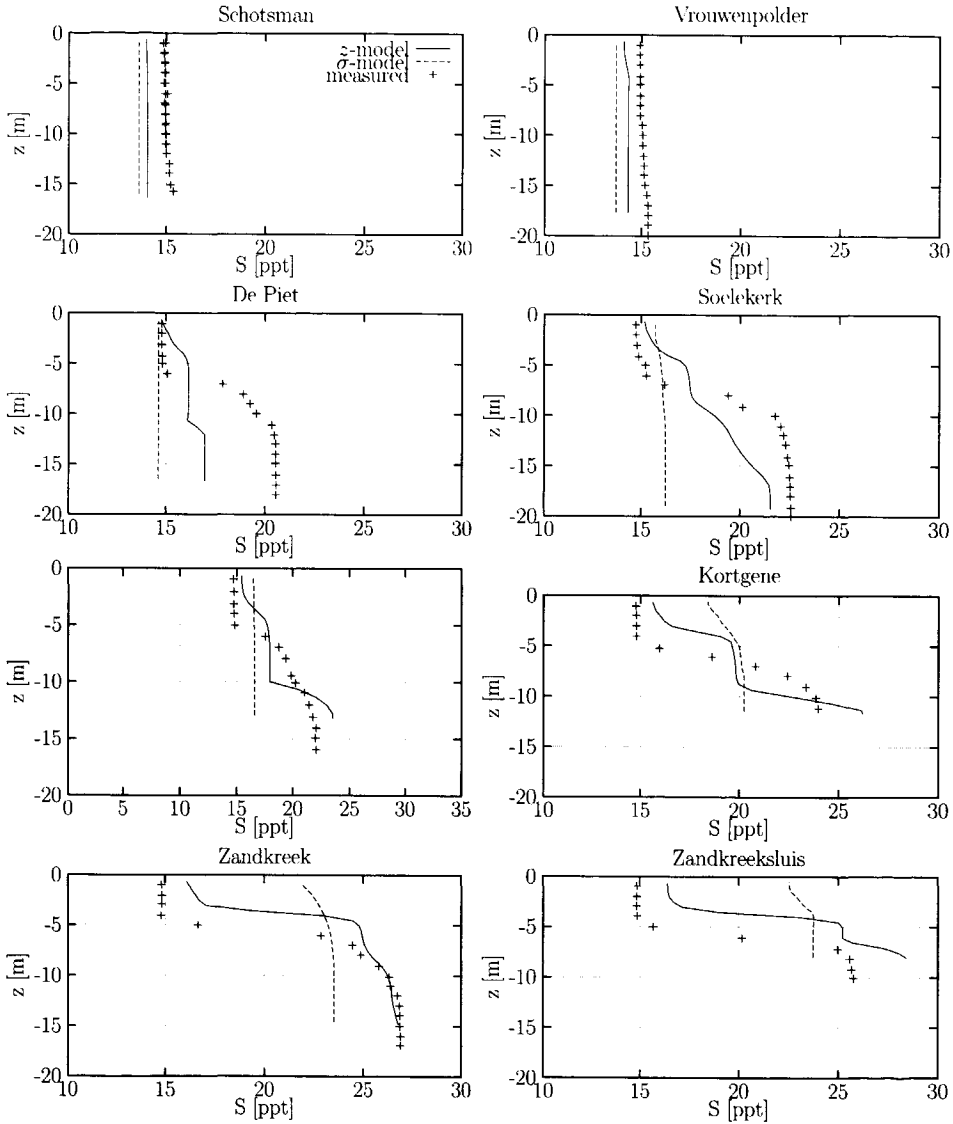


Figure 5.19: Computed and measured vertical distribution of salinity at June 20 1995. Solid line: z -model, dashed line: σ -model with anti-creep, +: measurements. For the approximate positions of the monitoring stations see Figure 5.17.

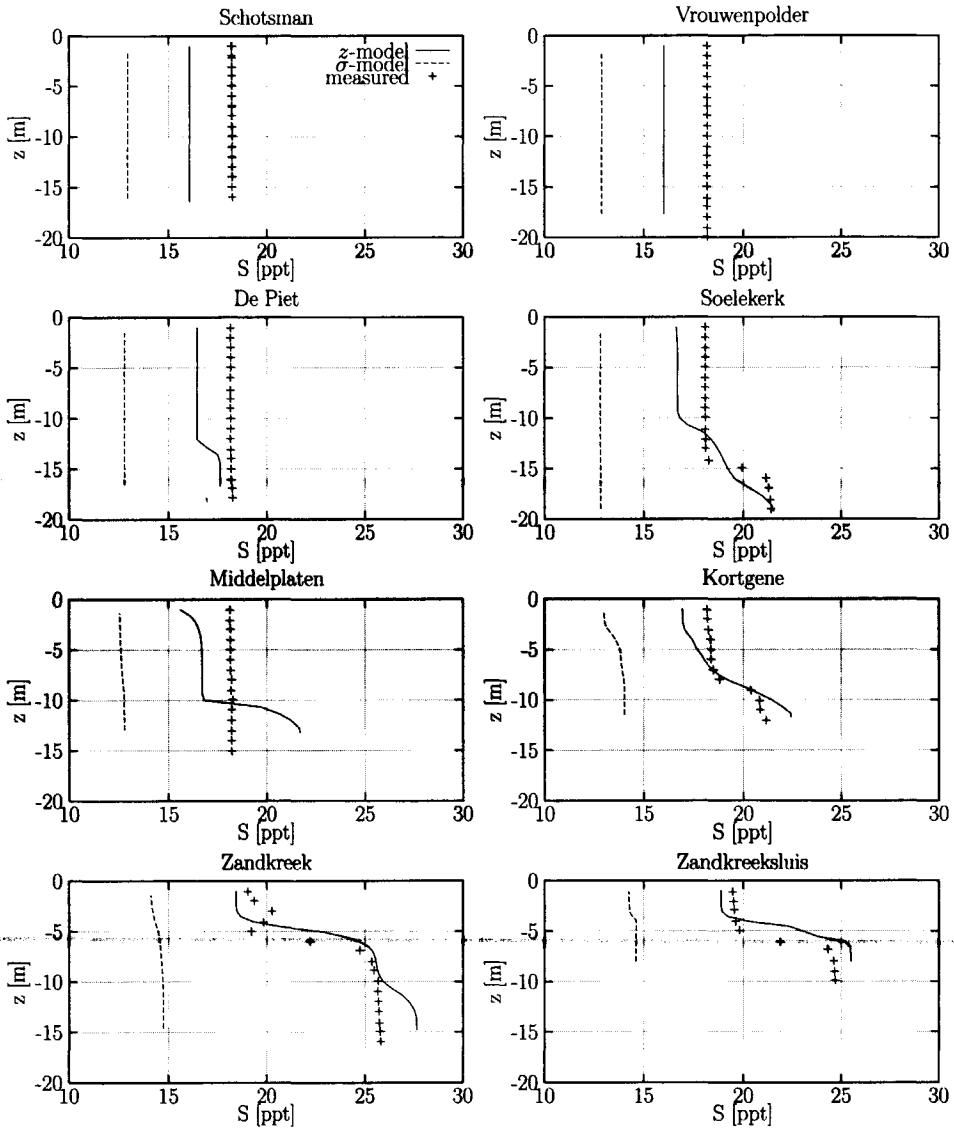


Figure 5.20: Computed and measured vertical distribution of salinity at December 7 1995. Solid line: z -model, dashed line: σ -model with anti-creep., +: measurements. For the approximate positions of the monitoring stations see Figure 5.17.

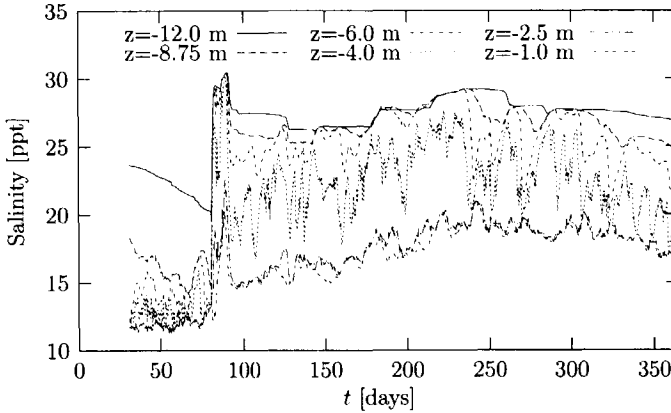


Figure 5.21: Time series of salinity at various heights in the water column at "Zandkreeke".

the local mixing of water. The coarse resolution of grid, the model assumption regarding the hydrostatic pressure and the lack of information on the discharge regime introduce errors in modelling this mixing process. For example, the discharges are imposed as a monthly constant value which obviously is a crude representation of reality. Since water is discharged near the bottom and withdrawn near the free surface in the numerical model, the amount of mixing influences the total amount of salt entering the lake. Besides, the density differences are diminished by the vertical mixing and thereby the baroclinic pressure gradient is reduced. Both phenomena contribute to the reduction of the intrusion length of the salt wedge.

In contrast with the z -model, the σ -model appears to be dominated by (artificial) mixing. Vertical gradients of salinity are hardly resolved by the model. Concluding from the vertical salinity profiles, the mixing is established in the region near the sluices. As mentioned before, this causes large amounts of salt to be sluiced out of the model. This is substantiated by the results obtained with the σ -model at December 7. The total amount of salt in the σ -model appears to be significantly lower than in the z -model. In the absence of open boundaries this can only be caused by the withdrawal of water.

The better results of the z -model is evident by comparing the model results to the measurements at December 7. Especially near the sluice at "Zandkreek" and "Zandkreeksluis" the z -model results can be seen to be very satisfactory. At the remainder of the monitoring positions, the vertical mixing in the z -model appears to be underestimated by the z -model. Physically, this mixing is introduced by the increasing wind speeds at the end of the year causing the stratification to erode. This does not hold for "Schotsman" and "Vrouwenpolder". At these positions stratification was already absent in June.

Summarising the Lake Veere results it may be concluded that with the present resolution the σ -model is unable to represent the stratified flow in the lake satisfactory. The z -model, on the other hand, shows rather good agreement with the measurements. This is especially true if we consider that this model is forced by data which lack resolution in time. In the following section the poor performance of the σ -model is investigated by means of a two-dimensional laterally averaged (2DV) schematisation of Lake Veere.

5.3.3 Two-dimensional schematisation Lake Veere

Due to the interplay of the different physical processes in the Lake Veere simulations, it is hard to draw conclusions about the cause of the large discrepancies between the z -model and σ -model results. In order to understand the behaviour of the z -model and σ -model in the Lake Veere simulations, a two-dimensional vertical (2DV) schematised model of Lake Veere was set up.

The 2DV model has a length L of 7000 m. The bathymetry of the 2DV model consists of two parabolic shaped pits with bottom slopes and depth similar to those in the actual bathymetry. A third deep pit (which has a depth of 500 m and is not shown in the presentation of the results) is situated near the closed boundary at $x = 0$. Potential reflections of the salt wedge at the boundary at $x=0$ are thus prevented as much as possible. The resolution of the horizontal grid in the pits is comparable to the grid spacing in the pits of the original Lake Veere model.

Incorporating all physical aspects makes it hard to trace the cause of the excessive mixing in the σ -model. Therefore effects of wind and temperature on the hydrodynamics of the lake are disregarded in the schematised Lake Veere simulation. Only the effects of a single constant discharge, situated near the closed model boundary at $x = L$, are taken into account. To test the models under both forced and unforced conditions, salt water was discharged into the system for only $\frac{1}{6}$ of the total simulation period T (which is equal to 500 hours). During this period the water level increases linearly in time. The discharge imposed is equal to $7.5 \text{ m}^3/\text{s}$ which gives rise to a total water level rise of approximately 2 m. The salinity of the discharge is equal to 12.5 ppt, yielding a maximal density difference of about $10 \text{ kg}/\text{m}^3$.

A horizontal grid spacing of 100 m is used and the time step is equal to 15 s leading to an average CFL-number for the free surface wave of about 5. The number of layers in the z -model and the σ -model are respectively equal to 30 and 20 with a similar distribution of layers as in the 3D simulations of Lake Veere. The vertical eddy viscosity is again computed by means of the 3D k - ϵ turbulence model. No background viscosity was added to the computed eddy viscosity.

Results

In contrast with the Lake Veere simulations presented in the previous section, the present simulations are also carried out with the σ -model that does not make use of the anti-creep procedure of Stelling and Van Kester. In this model the horizontal pressure gradients and diffusion are computed along σ -planes, see section 2.5.4. Results of three models are therefore presented: the z -model, the σ -model with anti-creep correction and the σ -model without anti-creep correction. The latter is indicated as the standard σ -model.

In Figure 5.22 vertical salinity profiles are plotted for different stages during the computation in the center of the right pit. Initially the σ -models exhibit a stronger stratification than the z -model. During this stage a gravity current travels down the slope of the right pit. As concluded in section 5.1.4, the σ -model is superior to the z -model for this type of boundary layer flow because of the favourable grid orientation. The z -model results are clearly affected by the stair case representation of the bottom introducing numerical diffusion of salt in the pits. The anti-creep procedure of Stelling and Van Kester also tends to yield stronger stratification than the standard σ -model.

Just after $t = \frac{1}{6} T$, the maximum salt concentration is reached in the right pit in all three models. The numerical diffusion in the z -model has led to a stratified system with nearly constant salinity in the pit. Both σ -models give rise to larger salinity gradients in this pit. This is due to the above mentioned mixing in the z -model, which is nicely brought out by the vertical profile of the horizontal velocity in the centre of the right pit at $t = \frac{1}{6} T$ (Figure 5.23). It can be seen from these velocity profiles that the height of the gravity current is significantly larger in the z -model compared to the ones computed by the σ -models. The total circulation pattern is stretched out over the entire depth of the pit in the z -model. In both σ -models on the other hand, the intrusion of salt water near the bottom is restricted to a much smaller area than in the z -model. The suppression of vertical mixing by using the anti-creep procedure in the σ -model is clearly brought out at this stage.

After the discharge has stopped a quiescent stably stratified system should develop in the pit. Internal waves damp during this stage and may lead to some vertical mixing in the pits. Velocities ought to reduce significantly during this period and vanish eventually. This process is depicted in Figure 5.22 from $t = \frac{2}{6} T$ to $t=T$. The vertical profiles of the horizontal velocity and the vector field of velocity at $t=\frac{1}{6}T$ and $t=T$ are given in Figure 5.23. It can be concluded from these figures that the z -model reproduces the development of a quiescent stably stratified system best. Only a small amount of vertical mixing has led to some erosion of the density interface. This mixing can be attributed to internal long waves in the upper part of the water column which are reflected at the closed boundaries, despite the presence of the deep pit. The stratification at $t=T$ is much stronger in the z -model than in both σ -models and velocities have nearly vanished in the pits. Note that the internal wave in the upper part of the water column is not yet entirely damped at $t=T$ and still gives rise to some vertical mixing at the density interface.

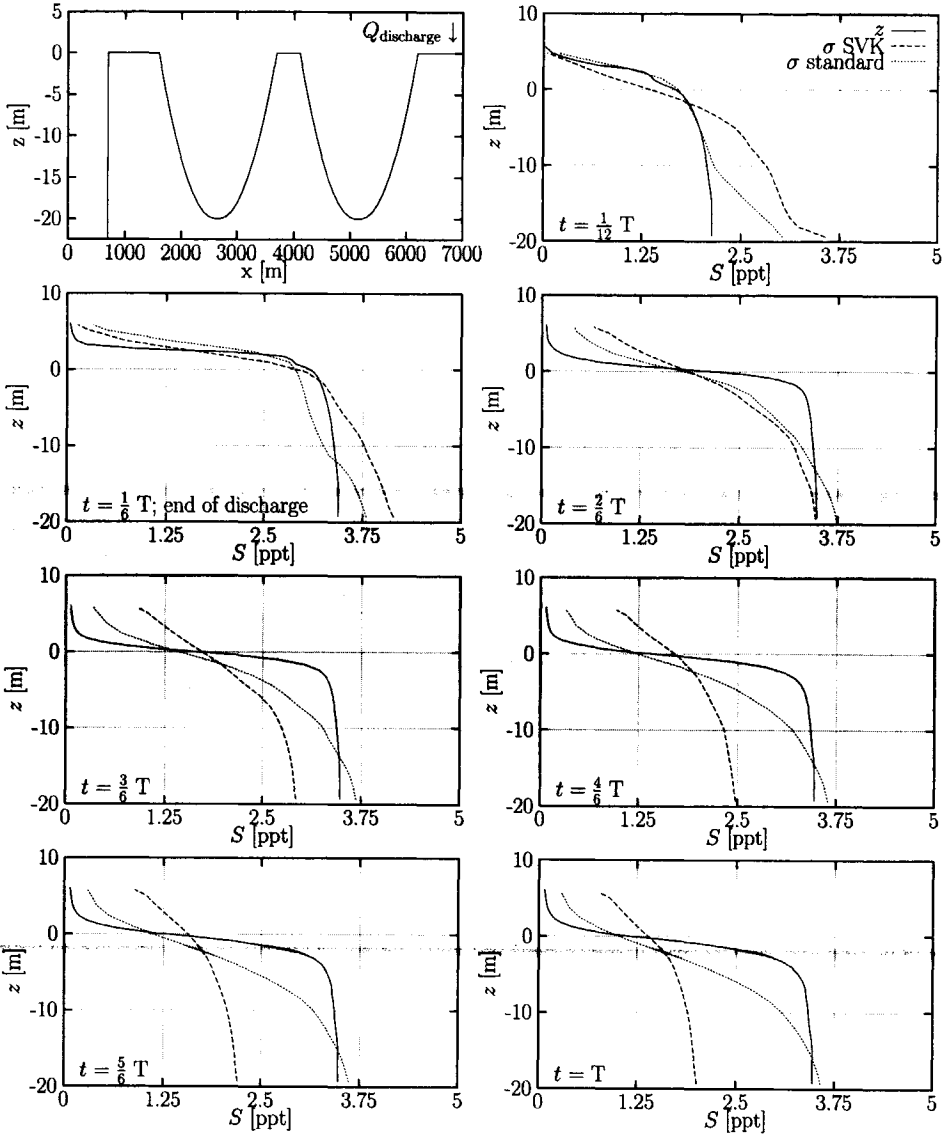


Figure 5.22: Bathymetry of 2DV-model of schematised Lake Veere (top left). Vertical salinity distribution in the centre of the right pit at 7 different stages during the simulation. At $t = \frac{1}{6} T$ the discharge is halted ($T = 500$ hrs.). Solid line: z -model, dashed line: σ -model with anti-creep, dotted line: σ -model without anti-creep.

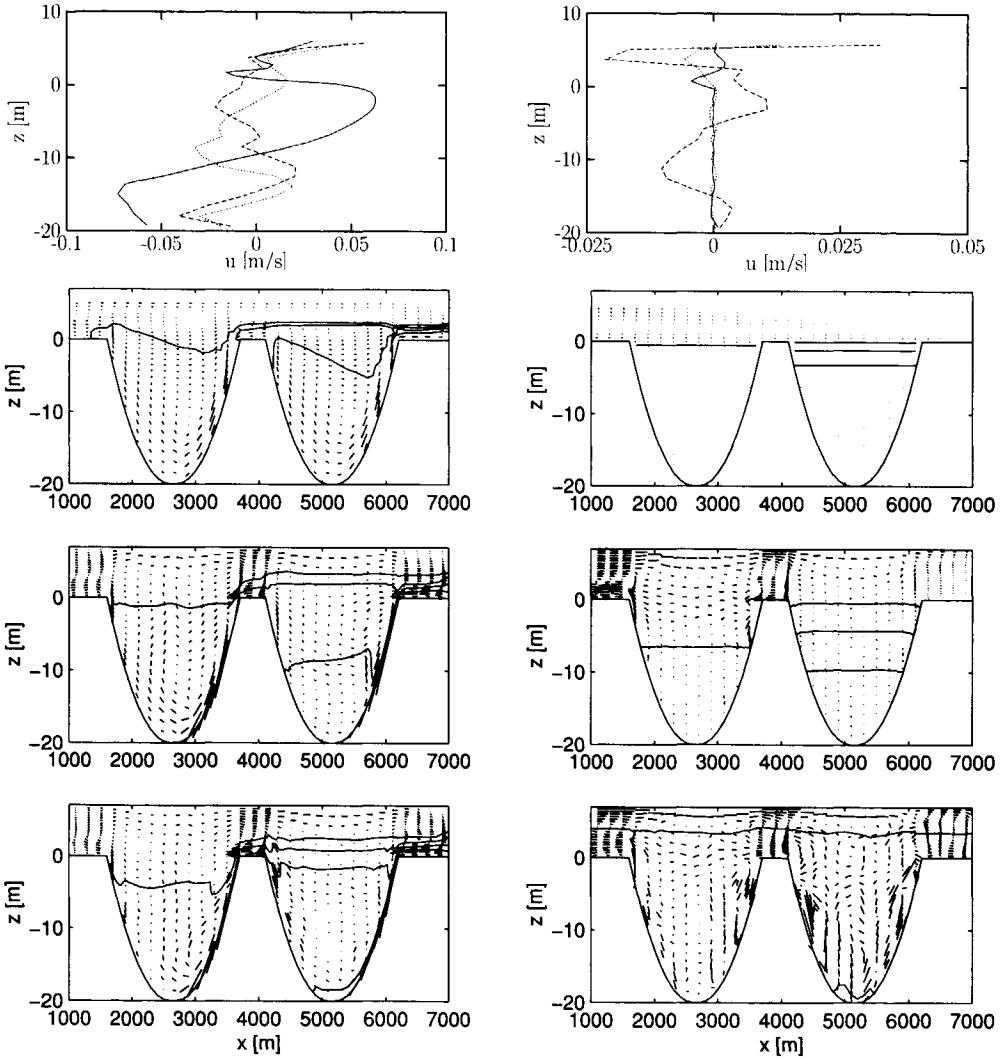


Figure 5.23: Two uppermost panels: vertical distribution of horizontal velocity at $t = \frac{1}{6} T$ (left) and $t=T$ (right) at the centre of the right pit. Note the different scales. See Figure 5.22 for legend. Lower panels: approximate vector field of velocity and isolines of salinity at $t = \frac{1}{6} T$ (left) and $t=T$ (right). Plot interval of the isolines is 1 ppt and every second vectors in the horizontal direction is plotted. From top to bottom: z -model, standard σ -model and σ -model with anti-creep procedure.

The combination of stratification and steep bottom slopes gives rise to artificial mixing in the standard σ -model. The upwelling of salt water leads to a continuous decrease of the amount of salt in the pits. Artificial mixing is expected to continue until density gradients are no longer present in the pit. Hence, the standard σ -model will ultimately lead to a fully mixed quiescent system.

In contrast with the test cases reported in Stelling & Van Kester (1994), the σ -model with the anti-creep procedure is subject to even stronger vertical mixing than the standard σ -model³. At $t=T$ no steady state is reached and the mixing seems to continue until fully mixed conditions prevail. While velocities in the z -model and the standard σ -model are negligible below $z=0$ at the centre of the right pit, the σ -model with the anti-creep procedure gives rise to velocities which are of the same order of magnitude as observed during the discharge period.

Comparing the different terms arising in the momentum equation at different stages of the simulation did not reveal the underlying cause of the spurious flow in the σ -model with the anti-creep procedure. Furthermore, the use of the extended filter showed to be of minor importance and are therefore not presented here. Similarly, reduction of the time step did not improve the results either.

Although a quantitative explanation is not found at present, the excessive vertical mixing may be explained qualitatively by considering the determination of the baroclinic pressure gradients in the standard σ -model and the σ -model with the anti-creep procedure.

The pressure gradient in the standard σ -model is computed at a cell face (with index $i+1/2, k$, for example) between two neighbouring grid cells of the boundary fitted grid. Irrespective of the bottom slopes and the horizontal grid resolution, this results in a baroclinic pressure gradient which only acts on the grid cell under consideration, *i.e.* the grid cell at $i+1/2, k$. Hence, flow is induced by the baroclinic pressure gradient at $i+1/2, k$ only. Consequently, saline water is only transported in horizontal direction from the grid cell at i, k to the grid cell at $i+1, k$. This means that an initially stably stratified system is maintained, providing that the time step is sufficiently small.

Using the method of Stelling & Van Kester, on the other hand, a horizontal density gradient may give rise to a baroclinic pressure gradient higher in the water column, *i.e.* at grid cells with vertical index l , where $l \leq l < k$. This is due to the fact that the baroclinic pressure gradient is determined on the basis of Cartesian control volumes by rotating the σ -grid, see Figure 2.4. The resulting flow field and related transport of salt may locally give rise to unstable stratification and the generation of vertical circulation.

It is stressed that this explanation is tentative and needs to be validated by future simulations.

³It is noted that the test cases reported by Stelling & Van Kester (1994) are essentially different from the present ones. In contrast with the present simulations, Stelling & Van Kester start from a quiescent stably stratified cavity and do not consider the inflow of salt in the cavity at the upper part of the water column.

5.4 Discussion

The implementation of the z -model and the σ -model is validated by means of 2DV test cases showing consistent results for flows with nearly constant depth. As expected, discrepancies between the models arose in case of flow over sloping topography. In order to obtain satisfactory results with the z -model, some modifications of the original model defined in Chapter 2 were required. These adjustments are directly related to the stair-case representation of the bottom in the z -model and concern the bottom friction term and the discretisation of the horizontal advective term near solid boundaries, which are encountered more frequently in the z -model than in the σ -model. The proposed adjustments are therefore less relevant for the latter model. Furthermore, the conservative implementation of the advective terms in the momentum equation was found to be of importance with respect to the celerity of gravity currents. Using a non-conservative discretisation method appears to have a retarding effect on the propagation of the salt wedge. This is, however, only verified in a frictionless situation with predominant baroclinic forcing. In the presence of other external forcing, the corollary is likely to be less apparent. Moreover, the conservative discretisation is more diffusive than the discretisation proposed in section 2.5.4 and has therefore not been employed for the three-dimensional prototype test cases.

Application of the z -model and σ -model for the Haringvliet estuary has shown that both approaches are appropriate for modelling estuarine flow, provided that the inherent disadvantages of the models are minimised. Hardly any discrepancy between the model results could be observed. Therefore it can be argued that both models perform equally well in regions with relatively mild slopes. In this respect it is noted that the notion of steepness is not only related to the topography but is also connected with the horizontal grid resolution, as for example expressed by the hydrostatic consistency condition.

The 3D Lake Veere simulations and the 2DV schematisation have provided much insight in the models' performance in simulating stratified flow over steep topography with relatively coarse grids. It was found that the dynamic process of the initial filling of the pits is modelled best by the σ -coordinate models. This stage is governed by boundary layer flow for which the σ -models are suited better than the z -model. The latter suffers from numerical cross-wind diffusion due to the strict horizontal orientation of the vertical grid in the model. The preferential orientation of the boundary-fitted σ -layers becomes less obvious when the pits are (partially) filled. Due to the development of stratification the flow is no longer attached to the bottom. The horizontal orientation of the grid cells in the z -model then becomes favourable.

Under weakly forced or unforced conditions the dynamic system eventually degenerates into a quiescent stably stratified system. This behaviour was modelled satisfactorily by the z -model only. During this phase both σ -models (with and without anti-creep procedure) were clearly subject to excessive vertical mixing. The artificial vertical mixing and upwelling is a well-known phenomenon in the standard σ -model. However, the bounding of the artificial mixing by applying the anti-creep approach of Stelling & Van Kester does not improve the

results in this case and even results in a stronger mixing. Although the latter is not fully understood yet, this phenomenon may be caused by the generation of unstable stratification leading to strong vertical mixing. Additional research is required to investigate the validity of this hypothesis.

Based on the comparison of the z -model and σ -model for stratified flow in regions with varying bathymetry, it can be concluded that the choice between the z -model and the σ -model approach is not unambiguous and is problem dependent. Only for relatively simple flow conditions (pure boundary layer flow, stably stratified lakes etc.) this choice is evident. For more complex flow knowledge of the anticipated flow field is required. In some cases both model approaches may turn out to produce inaccurate results and a reduction of the horizontal grid spacing is then necessary.

Chapter 6

Conclusions and recommendations

6.1 Vertical coordinate system: σ vs. z

The present work concerns the modelling of estuarine hydrodynamics. In these regions the computational grid is usually strongly anisotropic due to the shallowness of the flow. The use of relatively coarse grids in the horizontal plane causes the numerical results to be dependent on the orientation of the computational grid. The choice of the vertical grid is of particular importance. In regions where stratification and large bathymetric variations occur, the quality of the computational results may to a large extent be determined by the choice of the vertical grid.

In order to study the effects of the vertical coordinate system on the computational results, two numerical models were developed that use identical numerical techniques except for the vertical coordinate system employed. These models are based on the Cartesian z -coordinate system and the boundary fitted σ -coordinate system. The inherent drawbacks of each of the coordinate systems were minimised as much as possible to allow for a sound comparison between both approaches. The performance of the z -model and the σ -model was assessed by comparison of the computational results to laboratory and field measurements.

The development of the numerical models based on the z -coordinate system and the σ -coordinate system and the intercomparison of these models has led to the following conclusions and recommendations:

Conclusions

- Significant differences between the σ -model and the z -model are only observed when modelling regions with steep topography using coarse horizontal grids. For sufficiently high horizontal resolution of the computational grid, the results of both models should converge, irrespective of the slope of the bottom.

- The suitability of a vertical coordinate system depends on the type of flow and is strongly related to the orientation of the computational grid with respect to the flow direction. In order to minimise the numerical cross-wind diffusion, a vertical grid should be used which grid lines coincides with the direction of the anticipated flow field and density gradients as much as possible.
- Accurate transport schemes are imperative when modelling regions with steep topography using coarse horizontal grids.
- In situations that neither the z -model nor the σ -model is capable of resolving the vertical structure of the flow, the horizontal grid size should be reduced in order to obtain a grid spacing which is much smaller than the typical length scale of the bathymetric variations. This requirement may result in a computational grid that is nearly isotropic.
- Computational results obtained with the z -model are strongly dependent on the treatment of the free surface elevation, the bottom shear stress and the approximation of the horizontal advection terms near solid walls. The proposed numerical approximations for these terms were found to be necessary to obtain satisfactory results.
- The simulation of boundary layer flow with the z -coordinate model in regions with steep bottom slopes requires high-resolution grids. This is due to the cross-wind diffusion and may therefore to a large extent be attributed to the lower order approximations of the advective terms in the momentum and transport equation.
- The required number of layers in the z -model is generally larger than in the σ -model in regions with large bathymetric variations. However, it was found that for typical estuarine applications the computational effort hardly increased due to the large number of inactive grid points in these regions.
- The approximation of the horizontal pressure gradient and diffusive fluxes in σ -coordinates as proposed by Stelling & Van Kester (1994), appeared to give rise to excessive artificial mixing under certain conditions. The development of unstably stratified conditions by this method may possibly give rise to this behaviour.
- The time integration method used for the construction of the present z -model and σ -model was shown to be rather dissipative. This may be circumvented by adopting a different value for θ . Furthermore, the spatial discretisation of the horizontal advection in the momentum equation and the vertical advection in the transport equation is only of first order accuracy, which introduces artificial smearing in the numerical model. This may amplify the discrepancies between the z -model and the σ -model results. Related to the above remarks concerning the accuracy of the models, it

may be stated that the present numerical models are only suitable for modelling free surface flow with predominant external forcing.

- The explicit treatment of the horizontal advection terms imposes a time step restriction due to the stability criterion thus introduced, but does not lead to excessively small time step due to the relatively large horizontal grid spacing in shallow-water modelling. Furthermore, the explicit treatment of the advective terms in the momentum equation and the transport equation facilitates the implementation of conservative non-oscillatory transport schemes.
- For frictionless flows that are fully dominated by baroclinic forcing (such as the lock exchange flow) it was found that the front speed of a salt wedge is dependent on the discretisation of the advection terms in the momentum equation. Application of a fully conservative numerical scheme gave rise to a significant increase of the celerity of the front compared to a scheme that is not strictly conservative and was found to be in better agreement with the theoretical value.

Recommendations

- The excessive mixing under unforced stratified conditions due to the application of the method proposed by Stelling & Van Kester (1994) is presently not entirely understood. Although this behaviour is likely to be related to the development of unstably stratified conditions, additional research is required to investigate the validity of this hypothesis.
- The potential time step restrictions due to the explicit treatment of the horizontal advective terms may be circumvented by locally employing a fully implicit integration technique (*e.g.* Carlson method, see (Richtmyer & Morton, 1967)).
- Higher order schemes should be applied to determine the influence of the discretisation errors on the departure between the z -model and σ -model results.
- The large variation of the vertical grid spacing near the bottom in the z -model may give rise to inaccuracies. Presently no measures are taken to prevent this. The introduction of a lower bound for the vertical grid spacing near the bottom is recommended.
- Application of explicit vertical transport schemes is in principle possible in the z -model if a lower bound for the vertical grid spacing is adopted. Hence, accurate and monotonic advection schemes for the advection of momentum and matter in the vertical direction can be implemented with little effort.

- Because of the Cartesian grid definition, the z -model forms a good basis for the development of a non-hydrostatic code. Accounting for the hydrodynamic pressure implies extra work. Furthermore, nearly isotropic grid cells are needed for the accurate computation of the pressure distribution. Although this may lead to an increasing computational effort, the use of non-hydrostatic codes for free surface modelling is likely to increase in the near future due to the increasing computer resources.

6.2 Shallow-water turbulence modelling

A two-length-scale turbulence model was presented that is based on the well-known k - ε turbulence model. This model, which is computationally hardly more expensive than the standard k - ε -model, takes anisotropy of shallow-water turbulence into account via two separate turbulence models. The small-scale bottom generated turbulence, which is essentially three-dimensional, is modelled by a 3D k - ε model in which the production of turbulent kinetic energy is determined solely by vertical velocity gradients. The larger scale quasi-two-dimensional turbulence is modelled with a depth-averaged k - ε turbulence model in which the turbulent kinetic energy is produced by horizontal velocity gradients only. The direct interaction of the two separate turbulent length scales was neglected, although it may play an important role in real-life turbulence. However, interaction via the mean flow still exists. Laboratory measurements were carried out to facilitate the validation of the two-length-scale turbulence model.

The development of the two-length-scale turbulence model and the validation of this model by means of comparison of numerical results to laboratory measurements, has led to the following conclusions and recommendations:

Conclusions

- Results of previous experiments show that shallow-water flow induces anisotropy of turbulence and leads to a disparity of turbulent length scales. Besides the 3D **bottom friction generated turbulence**, **large quasi-2D turbulent structures** may exist with horizontal dimensions that are typically several times the water depth. In the laboratory measurements described in this thesis, similar turbulent structures were observed in a mixing layer.
- To account for the disparity of turbulent length scales in the case of quasi-2D turbulence, a turbulence model is required which yields an eddy viscosity that possesses directional dependency. Hence, multiple length scale turbulence models are required for the modelling of shallow-water turbulence. The standard k - ε turbulence model accounts for bottom friction generated turbulence only, which has a length scale of typically the water depth. The anisotropic nature of the flow is therefore not reflected

in this turbulence model which results in the underestimation of the Reynolds shear stresses and, thereby, the horizontal momentum transfer.

- The horizontal Reynolds shear stress computed with the two-length-scale k - ε turbulence model presented in this thesis shows good agreement with laboratory measurements, both qualitatively and quantitatively. Especially near the free surface, where the eddy viscosity in the standard model goes to zero, the two-length-scale turbulence model yields significant improvements.
- The model coefficients used in the two-length-scale turbulence model are taken equal to those in the original k - ε turbulence model. Although these coefficients have been derived for flows that deviate strongly from the ones described in this thesis, this setting proved to work well for turbulent shallow-water flow on the laboratory scale.
- The two-length-scale turbulence model has been developed for unstratified flows and cannot be directly applied to stratified conditions.
- The disadvantage of a constant horizontal eddy viscosity, which gives the model an empirical character, can be circumvented by application of the two-length-scale turbulence model. This is even more true when non-stationary complex flows are considered for which prescribing an empirical eddy viscosity is not a trivial task. The extra amount of work introduced by addition of two depth-averaged transport equations to the model is minor in 3D applications.

Recommendations

- Due to the rather crude modelling of the quasi-2D turbulence by means of the k - ε -model concept it seems inappropriate to include all details of the physical processes in the model. Only the main features of the turbulence can be accounted for with the present approach. However, adjustments of the model coefficients may prove to be necessary when the turbulence model is applied to prototype situations. Two-dimensional-horizontal Large Eddy Simulations may be used for the determination of the model coefficients under different conditions.
- Although the computational results proved to be hardly sensitive to the type of boundary conditions imposed at solid walls, it is recommended that further research is carried out on this subject. New physical insight may be obtained from these experiments which is imperative for the future development of turbulence models for shallow-water turbulence.
- Related to this, further testing of the two-length-scale turbulence model is proposed to investigate the applicability of the model for various types of flow. Additional experimental data are needed for model validation.

- Inclusion of the effects of stratification in the two-length-scale turbulence model are needed in order to increase the range of the applicability of the model.

6.3 Summary

In three-dimensional numerical modelling of free surface flow in coastal regions the vertical computational grid is usually characterised by a strong anisotropy. Provided that the orientation of the vertical grid coincides with the local flow field and the density gradients this does not impose numerical problems. However this is generally not the case and numerical errors may hamper the accuracy of the results. In practical applications, it often remains unclear to what extent these numerical errors affect the computational results. In order to assess the dependency of the numerical results on the computational grid, two numerical models are developed in this thesis that use identical time integration and spatial discretisation and differ in the choice of the vertical coordinate system only. The testing of both models - which are respectively based on the Cartesian z -coordinate system and the boundary fitted σ -coordinate system - showed that much attention needs to be paid to the very details of both models in order to get a fair agreement between the results for relatively simple test cases. Particular attention was paid to the treatment of the free surface, the bottom shear stress and the horizontal advection near solid walls in the z -model. Furthermore, comparison of the numerical models shows that the numerical errors may affect the accuracy of the computational results significantly in regions with strongly varying bathymetry. It is noted that the lower order approximation of the advection terms may enhance these observations. In this respect the notion of steepness is not only related to the topography itself but is also connected with the horizontal grid resolution. After all, the inherent disadvantages of the σ -model related to the violation of the hydrostatic consistency condition and the problems related to the stair-case representation of the bottom in the z -model ought to be negligible for sufficiently small horizontal grid spacing. Applications for which the optimal choice between the two vertical coordinate systems are not evident, the use of (nearly) isotropic grid spacing may be inevitable to ensure a sufficiently accurate numerical solution.

In certain parts of the estuary it may be desirable to resolve physical processes with a typical length scale of the order of the water depth, which requires high resolution grids as well. For example, the siltation of the harbours that are situated in estuaries and the dispersion of pollutants are to a large extent determined by turbulent exchange processes with a typical length scale of (several times) the water depth. Traditionally, these turbulent processes are accounted for by using the eddy viscosity concept. Most of the turbulence models are based on the assumption that the turbulence is isotropic and therefore the eddy viscosity has no directional dependence. However, in shallow water the coexistence of small-scale three-dimensional turbulence and large-scale quasi-two-dimensional turbulence may give rise to disparity of turbulent length scales. Due to this disparity the turbulent

stresses and fluxes in the horizontal direction are different from the ones in the vertical. Obviously an anisotropic eddy viscosity is then required for the proper modelling of the turbulent exchange processes.

Despite the fact that the importance of large coherent structures has been well recognised in the field of oceanography and meteorology for quite some time, little attention was paid to the quasi-two-dimensional turbulent structures in the civil engineering community until recently. As a consequence few attempts have been reported on the development of a turbulence model for shallow-water turbulence. In this thesis a two-length-scale turbulence model is presented that is based on the concept of the standard k - ε turbulence model. Despite the models' limitations and assumptions, the computed Reynolds shear stresses agreed well with the measured Reynolds shear stresses. This is in contrast with the standard k - ε turbulence model, which yields an underestimation of these turbulent stresses.

It must be noted that the new turbulence model is validated for two laboratory measurements only. For these situations, the standard model coefficients of the k - ε model proved to work well for the two-length-scale turbulence model. These coefficients were derived for flow conditions that differ significantly from the ones described in this thesis. Future testing of the turbulence model may reveal that adjustments of these model coefficients is imperative to make it suitable for different types of flow. Additional research on shallow-water turbulence is therefore desirable to substantiate the model formulation presented in this thesis and to extend the applicability of the two-length-scale turbulence model to stratified conditions.

References

- ASCE. 1988. Task committee on turbulence models in hydraulic computations. Turbulence modeling of surface water flow and transport: part I-V. *J. Hydr. Eng.*, **114**(9), 970–1073.
- BABARUTSI, S., & CHU, V. H. 1991. A two-length-scale model for quasi-two-dimensional turbulent shear flows. *Pages 53-60 of: Refined flows. Modelling*, vol. C. IAHR.
- BALZANO, A. 1998. Evaluation of methods for numerical simulation of wetting and drying in shallow water flow models. *Coast. Eng.*, **34**, 83–107.
- BATCHELOR, G.K. 1969. Computation of the energy spectra in homogeneous two-dimensional turbulence. *Phys. Fluids Suppl II*, 233–239.
- BIJVELDS, M.D.J.P. 1997. *Recirculating steady flow in harbours: comparison of numerical computations to laboratory measurements*. Tech. rept. 1-97. Fac. of Civil Eng., Delft Univ. of Techn.
- BIJVELDS, M.D.J.P. 1999. *3D numerical computations of the Haringvliet estuary using different vertical coordinates*. Tech. rept. 16-99. Fac. of Civil Eng., Delft Univ. of Techn.
- BIJVELDS, M.D.J.P., KRANENBURG, C., & STELLING, G.S. 1998. Turbulent shallow-water flow in a model harbour; experiments and numerical simulations. *In: HOLZ, K.P., BECHTELER, W., WANG, S.S.Y., & KAWAHARA, M. (eds), Proceedings of the 3rd international conference on hydro-science and -engineering (on CD-ROM)*.
- BIJVELDS, M.D.J.P., KRANENBURG, C., & STELLING, G.S. 1999a. 3-D numerical simulation of turbulent shallow-water flow in square harbor. *J. Hydr. Eng.*, **125**(1), 26–31.
- BIJVELDS, M.D.J.P., VAN KESTER, J.A.TH.M., & STELLING, G.S. 1999b. A comparison of two 3D shallow-water models using σ -coordinates and z -coordinates in the vertical direction. *Pages 130-147 of: SPAULDING, M., & BUTLER, L. (eds), Estuarine and coastal modeling 6, proc. conf.*

- BLUMBERG, A.F., & MELLOR, G.L. 1985. A description of a three-dimensional coastal ocean circulation model. In: HEAPS, N. (ed), *Three-dimensional shelf models, coastal and estuarine sciences*. Amer. Geophys. Union.
- BOUIJ, R. 1986. *Measurements of Exchanges between River and Harbour (in Dutch)*. Tech. rept. 9-86. Delft Univ. of Techn.
- BOUIJ, R. 1989. *Depth averaged $k-\epsilon$ -model in ODYSSEE*. Tech. rept. 1-89. Delft Univ. of Techn.
- BOUSSINESQ, T.V. 1877. *Mem. press acad. sci.* 3rd Ed. Page 46.
- BRITTER, R.E., & LINDEN, P.F. 1980. The motion of the front of a gravity current travelling down an incline. *J. Fluid Mech.*, **99**, 531-543.
- BROWN, G.L., & ROSHKO, A. 1974. On density effects and large structure in turbulent mixing layers. *J. of Fluid Mech.*, **64**(4), 775-816.
- BURCHARD, H., & PETERSEN, O. 1997. Hybridization between σ - and z -co-ordinates for improving the internal pressure gradient calculation in marine models with steep bottom slopes. *Int. J. for Num. Meth. in Fluids*, **25**, 1003-1023.
- CAMERON, W.M., & PRITCHARD, D.W. 1963. Estuaries. *Pages 306-324 of: HILL, M.N. (ed), The Sea*, vol. 2. New York: John Wiley and Sons.
- CHENG, R.T., & SMITH, P.E. 1990. A survey of three-dimensional numerical estuarine models. *Pages 1-15 of: SPAULDING, M.L. (ed), Estuarine and coastal modeling, proc. conf.* New York: American Society of Civil Engineers.
- CHU, V.H., WU, J.-H., & KHAYAT, R.E. 1991. Stability of transverse shear flows in shallow open channels. *J. Hydr. Eng.*, **117**(10), 1370-1388.
- DE KOK, J.M. 1994. *Numerical modeling of transport processes in coastal waters*. Ph.D. thesis, Utrecht University.
- DELEERSNIJDER, E., & BECKERS, J.M. 1992. On the use of the σ -coordinate system in regions of large bathymetric variations. *J. Marine Sys.*, **3**, 381-390.
- DELFT HYDRAULICS. 1981. *Aspects of modelling horizontal momentum transfer in shallow flow*. Tech. rept. R 1150. Delft Hydraulics Laboratory.
- DELFT HYDRAULICS. 1999. *Delft3D-flow manual*. Delft Hydraulics. Release 3.05.
- DRACOS, T., GIGER, M., & JIRKA, G.H. 1992. Plane turbulent jets in a bounded fluid layer. *J. Fluid Mech.*, **241**, 587-614.

- DUNSBERGEN, D.W. 1994. *Particle models for transport in three-dimensional shallow water flow*. Ph.D. thesis, Delft Univ. of Techn.
- DYER, K.R. 1997. *Estuaries: a physical introduction*. London: John Wiley and Sons.
- ECKART, C. 1958. Properties of water, Part II. The equation of state of water and sea water at low temperatures and pressures. *Am. J. of Science*, **256**, 225-240.
- FLETCHER, C.A.J. 1991. *Computational techniques for fluid dynamics*. Vol. 1 and 2. Berlin: Springer-Verlag.
- FORTUNATO, A.B., & BAPTISTA, A.M. 1994. Modeling near-bottom advective acceleration in surface water models. *Pages 1045-1052 of: ET AL., PETERS A. (ed), Computational methods in water resources X*. The Netherlands: Kluwer Academic Press.
- GARY, J.M. 1973. Estimate of truncation error in transformed coordinate, primitive equation atmospheric models. *J. Atmos. Sci.*, **30**, 223-233.
- HAIDVOGEL, D.B., & BECKMANN, A. 1999. *Numerical ocean circulation modeling*. London: Imperial College Press.
- HANEY, R.L. 1991. On the pressure gradient force over steep topography in sigma coordinate ocean models. *J. Phys. Oceanography*, **21**, 610-619.
- HARTEN, A. 1983. High resolution schemes for hyperbolic conservation laws. *J. Comp. Phys*, **49**, 357-393.
- HINZE, J. 1975. *Turbulence*. New York: Mc-Graw Hill.
- HIRSCH, C. 1990. *Numerical computation of internal and external flows*. New York: John Wiley & Sons.
- INGRAM, R.G., & CHU, V.H. 1987. Flow around islands in Rupert Bay: An investigation of the bottom friction effect. *J. Geoph. Res.*, **92**(13), 14521-14533.
- JANJIĆ, I.Z. 1977. Pressure gradient force and advection scheme used for forecasting with steep and small scale topography. *Contrib. Atmos. Phys.*, **50**, 186-199.
- JIRKA, G.H. 1998. Large scale flow structures and mixing processes in shallow flows. *In: Second International Symposium on Environmental Hydraulics*.
- JONES, W.P., & LAUNDER, B.E. 1972. The prediction of laminarization with a two-equation model of turbulence. *Int. J. Heat and Mass Transfer*, **15**, 301-314.

- KLIEM, N., & PIETRZAK, J.D. 1999. On the pressure gradient error in sigma coordinate ocean models: A comparison with a laboratory experiment. *J. Geophys. Res.*, **104**(c12), 29,781–29,799.
- KRAICHNAN, R.H. 1967. Inertial ranges in two-dimensional turbulence. *Phys. Fluids*, **10**, 1417–1423.
- KRAICHNAN, R.H. 1976. Eddy viscosity in two and three dimensions. *J. of Atm. Sci.*, **33**, 1521–1536.
- KRANENBURG, C. 1982. Stability conditions for gradient transport models of turbulent density-stratified shear flow. *Geophys. Astrophys. Fluid Dynamics*, **19**, 93–104.
- LANGENDOEN, E.J. 1992. *Flow patterns and transport of dissolved matter in tidal harbours*. Ph.D. thesis, Delft Univ. of Techn.
- LANGENDOEN, E.J., & KRANENBURG, C. 1993. Simulation of unsteady flow in harbors. *Advances in Hydro-Science and -Engineering*, **I**, 1612–1617.
- LAUNDER, B.E., & SPALDING, D. 1972. *Lectures in mathematical models of turbulence*. New York: Academic Press.
- LEENDERTSE, J.J., & LIU, S.K. 1975. *A three-dimensional model for estuaries and coastal seas. II Aspects of computation*. Tech. rept. R-1764-OWRT. Rand Corporation, Santa Monica.
- LEENDERTSE, J.J., & LIU, S.K. 1977. *A three-dimensional model for estuaries and coastal seas. IV turbulent energy computation*. Tech. rept. R-2187-OWRT. Rand Corporation, Santa Monica.
- LEONARD, B. P., & DRUMMOND, J. E. 1995. Why you should not use 'hybrid', 'power-law' or related exponential schemes for convective modelling—there are much better alternatives. *Int. J. for Num. Meth. in Fluids*, **20**, 421–442.
- MCCALPIN, J.D. 1994. A comparison of second-order and fourth-order pressure gradient algorithms in a σ -coordinate ocean model. *Int. J. for Num. Meth. in Fluids*, **18**, 361–383.
- MELLOR, G., & YAMADA, T. 1982. Development of a turbulence closure model for geophysical fluid problems. *Rev. Geophys. and Space Phys.*, **20**(4), 851–875.
- MELLOR, G., HAKKINEN, S., EZER, T., & PATCHEN, R. 1999. A generalization of a sigma coordinate ocean model and an intercomparison of model vertical grids. In: PINARDI, N. (ed), *Ocean forecasting: theory and practice*. Springer-Verlag.

- MELLOR, G.L., & BLUMBERG, A.F. 1985. Modeling vertical and horizontal diffusivities with the sigma coordinate system. *Mon. Weather Rev.*, **113**, 1379-1383.
- MELLOR, G.L., EZER, T., & OEY, L.-Y. 1994. The pressure gradient conundrum of sigma coordinate models. *J. Atmos. Oceanic Techn.*, **11**, 1126-1134.
- MESINGER, F. 1982. On the convergence and error problems of the calculation of the pressure gradient force in sigma coordinate models. *Geophys. Astrophys. Fluid Dyn.*, **19**, 105-117.
- MUNK, W., & ANDERSEN, E. 1948. Notes on the theory of the thermocline. *J. Marine Res.*, **1**.
- NEZU, I., & NAKAGAWA, H. 1993. *Turbulence in Open-Channel Flows*. Delft, The Netherlands: International Association of Hydraulic Research.
- OFFICER, C.B. 1976. *Physical oceanography of estuaries (and associated coastal waters)*. New York: John Wiley and Sons.
- PAUL, J.F. 1994. Observations related to the use of the sigma coordinate transformation for estuarine and coastal modeling studies. *Pages 336-350 of: SPAULDING, M.L., BEDFORD, K., BLUMBERG, A., CHENG, R., & SWANSON, C. (eds), Estuarine and coastal modeling III, proc. conf.* New York: American Society of Civil Engineers.
- PHILLIPS, N.A. 1957. A coordinate system having some special advantages for numerical forecasting. *J. Meteorology*, **14**, 184-185.
- PODBER, D.P., & BEDFORD, K.W. 1994. Tributary loading with a terrain following coordinate system. *Pages 475-488 of: SPAULDING, M.L., BEDFORD, K., BLUMBERG, A., CHENG, R., & SWANSON, C. (eds), Estuarine and coastal modeling III, proc. conf.* New York: American Society of Civil Engineers.
- PRANDTL, L. 1925. Uber die ausgebildete Turbulenz. *ZAMM*, **5**, 136.
- REYNOLDS, O. 1895. On the dynamical theory of incompressible viscous fluids and the determination of the criterion. *Philosophical Transactions of the Royal Society of London*, **186**, 123.
- RICHTMYER, R.D., & MORTON, K.W. 1967. *Difference methods for initial-value problems*. New York-London: Interscience publishers, Wiley.
- RODI, W. 1980. *Turbulence models and their applications in hydraulics - A state of the art review*. Delft, The Netherlands: International Association of Hydraulic Research.

- RODI, W. 1985. Calculation of stably stratified shear-layer flows with a buoyancy-extended $k-\varepsilon$ turbulence model. *Pages 111-140 of: HUNT, J.C.R. (ed), Turbulence and diffusion in stable environments.* Oxford: Clarendon.
- RODI, W. 1987. Examples of calculation methods for flow and mixing in stratified fluids. *J. Geophys. Res.*, **92**, 5305-5328.
- SIMONIN, O., UITTENBOOGAARD, R.E., BARON, F., & VIOLLET, P.L. 1989. Possibilities and limitations to simulate turbulent fluxes of mass and momentum, measured in a steady stratified mixing layer. *In: Proc. 23rd I.A.H.R. congress.*
- SLØRDAL, L.H. 1997. The pressure gradient force in sigma-co-ordinate ocean models. *Int. J. for Num. Meth. in Fluids*, **24**, 987-1017.
- SMAGORINSKY, J. 1963. General circulation model experiments with the primitive equations. *Mon. Weath. Rev.*, **91**(3), 99-164.
- STELLING, G.S. 1983. *On the construction of computational methods for shallow water flow problems.* Ph.D. thesis, Delft Univ. of Techn.
- STELLING, G.S., & BUSNELLI, M.M. 2000. Numerical simulation of the vertical structure of discontinuous flows. *Submitted to: Int. J. for Num. Meth. in Fluids.*
- STELLING, G.S., & VAN KESTER, J.A.TH.M. 1994. On the approximation of horizontal gradients in sigma co-ordinates for bathymetry with steep slopes. *J. for Num. Meth. in Fluids*, **18**, 915-935.
- STELLING, G.S., KERNKAMP, H.W.J., & LAGUZZI, M.M. 1998. Delft Flooding System: A powerful tool for inundation assessment based upon positive flow simulation. *Pages 449-456 of: LARSEN, BABOVIC & (ed), Proceedings of the 3rd international conference on hydroinformatics.*
- TENNEKES, H., & LUMLEY, J.L. 1972. *A first course in turbulence.* Cambridge, Massachusetts: MIT Press.
- TUKKER, J. 1997. *Turbulence structures in shallow free-surface mixing layers.* Ph.D. thesis, Delft Univ. of Techn.
- UIJTTEWAAL, W.S.J., & BOOIJ, R. 2000. Effects of shallowness on the development of free-surface mixing layers. *Phys. Fluids*, **12**(2), 392-402.
- UIJTTEWAAL, W.S.J., & TUKKER, J. 1998. Development of quasi two-dimensional structures in a shallow free-surface mixing layer. *Exp. in Fluids*, **24**, 192-200.

- UITTENBOGAARD, R.E., VAN KESTER, J.A.TH.M., & STELLING, G.S. 1992. *Implementation of three turbulence models in TRISULA for rectangular horizontal grids*. Tech. rept. Z162. Delft Hydraulics Laboratory.
- VAN KESTER, J.A.TH.M. 1994. *Validation of DELFT3D for mixing layer test. Phase 1: improved implementation k- ϵ model (in Dutch)*. Tech. rept. Z810. Delft Hydraulics Laboratory.
- VREUGDENHIL, C.B. 1994. *Numerical methods for shallow-water flow*. Water science and technology library. Kluwer Academic Publishers.
- VREUGDENHIL, C.B., & KOREN, B. (eds). 1993. *Numerical methods for advection-diffusion problems*. Notes on numerical fluid mechanics. Vieweg, Braunschweig, Wiesbaden.
- WALTERS, R.A., & FOREMAN, M.G.G. 1992. A 3D, finite element model for baroclinic circulation on the Vancouver Island continental shelf. *J. Marine Sys.*, **3**.
- WILCOX, D.C. 1993. *Turbulence modeling for CFD*. La Cañada, California: DCW Industries, Inc.
- ZIJLEMA, M. 1996. *Computational modeling of turbulent flow in general coordinates*. Ph.D. thesis, Delft Univ. of Techn.
- ZIJLEMA, M. 1998. *TRIWAQ-three-dimensional shallow water flow model, technical documentation*. Rijkswaterstaat/RIKZ.
- ZIJLEMA, M. 1999. *personal communications*.

Appendix A

Laboratory measurements yacht harbour " 't Steel"

The measurements were carried out using the so-called HILDA, a submersible laser Doppler anemometer (LDA) of Delft Hydraulics, see Figure A.1. The laser beams, radiated by the vertical laser tube are reflected by an opposing mirror and received by two glass fibers. The measuring volume is situated half-way between the tube and mirror, which poses a restriction to the vertical distance over which velocities can be measured. The maximum water depth in the region of interest is about 10 cm and consequently a significant part of the water depth would be excluded from the measurements. A further restriction was imposed by the position of the receiving glass fibers, which are situated well above the laser tube. In order to let the apparatus work properly, these fibers must be positioned under water and thus the effective distance over which velocities can be measured is further reduced. To overcome this drawback, a small bell filled with water by creating under-pressure, was attached to the laser tube. By comparing LDA-measurements with and without the bell at the same position, it was concluded that the disturbing effect of the bell can be neglected as long as it penetrates the water column only a few mm's. Therefore the bell was shifted upward for measurements deeper in the water column.

The LDA measures velocities in a horizontal plane in two orthogonal directions simultaneously, which makes it possible to determine horizontal Reynolds stresses. However, vertical velocities are not measured, leaving the vertical Reynolds stresses and the exact total turbulent kinetic energy, $k = \frac{1}{2}(\overline{u'^2} + \overline{v'^2} + \overline{w'^2})$, undetermined.

The sampling rate of the LDA measurements and the sampling period are determined by the accuracy required and by the information we want to obtain from the measurements. Using the second order statistical moment, defined by

$$\overline{(u'_i)^2} = \frac{1}{N} \sum_{n=1}^N (u'_n)^2 \quad (\text{A.1})$$

we can estimate the error for the normal Reynolds stresses measured or the TKE. Approximating the turbulent velocity fluctuations by a Gaussian or normal distribution function, which is correct in many situations, the statistical error ϵ in estimating the normal Reynolds stresses or TKE becomes (Tukker, 1997)

$$\epsilon = \sqrt{\frac{2}{M}} \quad (\text{A.2})$$

where M is the number of independent measurements. If we accept a relative error of 10 % this requires a number of independent measurements equal to 200. The measuring time depends on M and the time-scales of structures present in the flow. A suitable measure for the maximum time interval during which a three-dimensional turbulent velocity is correlated with itself, and thus represents a characteristic time scale of the large turbulent scales, is the integral time scale \mathcal{T} defined as (Tennekes & Lumley, 1972)

$$\mathcal{T} \equiv \int_0^{\infty} \rho(\tau) d\tau \quad (\text{A.3})$$

where τ is a time shift and $\rho(\tau)$ is the autocorrelation function defined by

$$\rho(\tau) \equiv \frac{\overline{u'_i(t)u'_i(t+\tau)}}{u'_i(t)^2} \quad (\text{A.4})$$

where t is the real time. The ratio of the measuring time and twice the integral time scale, $\frac{T_m}{2\mathcal{T}}$, may be regarded as the number of independent samples M in a record of length T_m (Tennekes & Lumley, 1972). However, in quasi-2D shear flows with 2D structures, such as the shallow water mixing layer in the harbour entrance, for example, these structures show a quasi periodic behaviour (Uijtewaal & Tukker, 1998) and (Tukker, 1997). The large-scale quasi-periodic structures are responsible for large correlation coefficients of varying sign for large time-shifts τ . This makes the definition of M using the time scale \mathcal{T} unusable in these situations. Therefore, it is more practical to consider M equal to the number of periods of the quasi-periodic fluctuations present in the measured time signal, as suggested in (Tukker, 1997). Since there is no *a priori* information of the flow, the integral time scale is estimated by

$$\mathcal{T} = \frac{\mathcal{L}}{\bar{u}} \quad (\text{A.5})$$

The characteristic turbulent length scale \mathcal{L} of the 3D turbulence, is restricted by the water depth of the model. However, 2D-dimensional structures up to several times the water depth can exist. For a shallow water mixing layer, that develops in the harbour entrance of the model, structures with a size three times the mixing layer width can exist (Tukker,

1997). The width of the mixing layer is estimated by the linear growth of a two-dimensional mixing layer (i.e. for infinite depth) (Brown & Roshko, 1974)

$$\frac{\Delta B}{\Delta x} = 0.18 * \frac{(u_r - u_h)}{(u_r + u_h)} \quad (\text{A.6})$$

where $u_r - u_h$ is the velocity difference over the mixing layer and B is the mixing-layer width defined by the velocity profile maximum slope thickness

$$B = \frac{u_r - u_h}{\left(\frac{\partial u}{\partial y}\right)_{max}} \quad (\text{A.7})$$

As a first guess, the velocity of the gyre u_h will be about $0.25u_r$ (Booij, 1986), where u_r is the mean flow velocity in the river, yielding a broadening of the mixing layer equal to $0.1\Delta x$. The maximum expected layer width will therefore be about 10 cm, yielding largest eddies with a size of about 30 cm. If we approximate the advective velocity of the eddies to be equal to half the river velocity (taking the advective velocity equal to the velocity in the centre of the mixing), this leads to a integral time scale of about 2 s and a measuring time of 7 minutes. In the experiments a measuring time of 10 minutes was used.

In order to analyze the spectral distribution of the turbulence down to the viscous subrange, the dimensionless wave number $\mathcal{L}k_{max}$ should be at least 100 (Nezu & Nakagawa, 1993). Since the macro-(or integral) scale of the 3D turbulence scales with the flow depth H , the maximum response frequency can be estimated as follows

$$f_{max} = \frac{k_{max}u}{2\pi} \geq \frac{100u}{2\pi\mathcal{L}} \simeq \frac{50u}{\pi H} \quad (\text{A.8})$$

Accounting for aliasing and taking $u = 0.3$ m/s and $H = 0.1$ m leads to a frequency of 100 Hz.



Figure A.1: Laser Doppler anemometer HILDA with bell attached to it

Appendix B

Expressions for the horizontal pressure gradient in σ -coordinates

In σ -coordinates the horizontal pressure gradient (HPG) is written as

$$\frac{\partial p}{\partial x} = \frac{\partial p}{\partial x^*} + \frac{\partial \sigma}{\partial x} \frac{\partial p}{\partial \sigma} = \frac{\partial p}{\partial x^*} - \frac{1}{H} \left(\frac{\partial \zeta}{\partial x} + \sigma \frac{\partial H}{\partial x} \right) \frac{\partial p}{\partial \sigma} \quad (\text{B.1})$$

and the hydrostatic pressure is given by

$$p = p_{atm} + gH \int_{\sigma}^0 \rho d\sigma' \quad (\text{B.2})$$

Variations of the atmospheric pressure, p_{atm} , will be neglected in the following. Starting from the above equations, different expressions can be derived for the horizontal pressure gradient in σ -coordinates. Mathematical manipulation of eq. (B.1) and eq. (B.2) leads to the following expressions which are used for discretisation respectively in the present model, the Delft3D-FLOW model (Delft Hydraulics, 1999), the Princeton Ocean Model (POM) (Blumberg & Mellor, 1985) and the TRIWAQ model (Zijlema, 1998).

- Present model

Inserting eq. (B.2) into eq. (B.1) and applying the chain rule yields

$$\frac{\partial p}{\partial x} = g \frac{\partial H}{\partial x^*} \int_{\sigma}^0 \rho d\sigma' + gH \frac{\partial}{\partial x^*} \int_{\sigma}^0 \rho d\sigma' + g\rho \left(\frac{\partial \zeta}{\partial x} + \sigma \frac{\partial H}{\partial x} \right) \quad (\text{B.3})$$

By inserting $H = \zeta + d$ into eq. (B.1) we arrive, after rearranging terms, at

$$\frac{\partial p}{\partial x} = \left(\rho\sigma + \int_{\sigma}^0 \rho d\sigma' \right) g \frac{\partial d}{\partial x} + gH \frac{\partial}{\partial x^*} \int_{\sigma}^0 \rho d\sigma' + \left(\rho(1 + \sigma) + \int_{\sigma}^0 \rho d\sigma' \right) g \frac{\partial \zeta}{\partial x} \quad (\text{B.4})$$

The discretisation of this expression is given in Chapter 2.

- Delft3D-FLOW

The horizontal pressure gradient used in the standard Delft3D-FLOW code (Delft Hydraulics, 1999) is simply obtained by inserting the hydrostatic pressure relation eq. (B.2) into the expression for the horizontal pressure gradient in σ -coordinates eq. (B.1)

$$\frac{\partial p}{\partial x} = g \frac{\partial}{\partial x^*} \left(H \int_{\sigma}^0 \rho d\sigma' \right) + g\rho \left(\frac{\partial \zeta}{\partial x} + \sigma \frac{\partial H}{\partial x} \right) \quad (\text{B.5})$$

- POM

The horizontal pressure gradient in the POM (Blumberg & Mellor, 1985) can be derived by applying partial integration to the first term in the right hand side of eq. (B.3)

$$\int_{\sigma}^0 \rho d\sigma' = -\sigma\rho - \int_{\sigma}^0 \sigma' \frac{\partial \rho}{\partial \sigma'} d\sigma' \quad (\text{B.6})$$

Inserting eq. (B.6) in eq. (B.5) yields

$$\frac{\partial p}{\partial x} = -g \frac{\partial H}{\partial x^*} \int_{\sigma}^0 \sigma' \frac{\partial \rho}{\partial \sigma'} d\sigma' + gH \frac{\partial}{\partial x^*} \int_{\sigma}^0 \rho d\sigma' + \rho g \frac{\partial \zeta}{\partial x} \quad (\text{B.7})$$

which can be written as

$$\frac{\partial p}{\partial x} = gH \int_{\sigma}^0 \left(\frac{\partial \rho}{\partial x^*} - \frac{\sigma'}{H} \frac{\partial \rho}{\partial \sigma'} \frac{\partial H}{\partial x} \right) d\sigma' + \rho g \frac{\partial \zeta}{\partial x} \quad (\text{B.8})$$

In this expression, the term containing $\partial \rho / \partial \sigma$ may become indifferentiable near a density interface. This does not hold for the second term in eq. (B.4) and the latter is therefore preferred.

- TRIWAQ

The horizontal pressure gradient in TRIWAQ (Zijlema, 1998) can be derived starting from eq. (B.3) which can be written as:

$$\frac{\partial p}{\partial x} = g \frac{\partial H}{\partial x} \left(\int_{\sigma}^0 \rho d\sigma' + \rho\sigma \right) + gH \frac{\partial}{\partial x^*} \int_{\sigma}^0 \rho d\sigma' + \rho g \frac{\partial \zeta}{\partial x} \quad (\text{B.9})$$

Using

$$\int_{\sigma}^0 \rho(\sigma) d\sigma' = -\rho|_{\sigma} \sigma \quad (\text{B.10})$$

we arrive at

$$\frac{\partial p}{\partial x} = g \int_{\sigma}^0 \left(H \frac{\partial \rho}{\partial x^*} + (\rho - \rho|_{\sigma}) \frac{\partial H}{\partial x} \right) d\sigma' + \rho g \frac{\partial \zeta}{\partial x} \quad (\text{B.11})$$

List of Symbols

Roman symbols

A	area
B	(mixing layer) width
B_k	buoyancy term in the k -equation
B_ε	buoyancy term in the ε -equation
c	concentration, scalar quantity
$c_D, c_\mu, c_\varepsilon, c_k$	model coefficients of the k - ε model
$c_{1\varepsilon}, c_{2\varepsilon}, c_{3\varepsilon}$	model coefficients of the k - ε model
c'_μ	empirical coefficient
c_f	friction coefficient
C_d	drag coefficient
d	water depth with respect to a reference level
D_h	horizontal eddy diffusivity
D_t	eddy diffusivity
D_v	vertical eddy diffusivity
E	local truncation error, power density
f	Coriolis parameter
f_{max}	maximum response frequency
F	energy loss
F_i	volume force per unit mass
F_i^*	Coriolis term
F_I	flux through surface I
Fr	Froude number
g	gravitational acceleration
h_f	height front salt wedge
H	total water depth
k	turbulent kinetic energy (TKE) per unit mass, wave number
k_N	Nikuradse roughness height
l_m	mixing length
L	geometric length scale

\mathcal{L}	characteristic turbulent length scale
M	number of independent measurements
N^2	Brunt-Väisälä frequency
p	pressure
p_{bcl}	baroclinic pressure
p_{btr}	barotropic pressure
P_k	production term in the k -equation
P_ε	production term in the ε -equation
q	discharge per unit width, depth-integrated discharge
Q	discharge
Q_b, Q_c, Q_s, Q_v	heat fluxes
Re	Reynolds number
Ri	Richardson number
s	source term
S_{ij}	deformation tensor
t	time
T	period, temperature
\mathcal{T}	characteristic turbulent time scale
u^{2D}	fluctuating part of the velocity in x -direction due to quasi-2D turbulent structures
u^{3D}	fluctuating part of the velocity in x -direction due to 3D turbulent structures
\bar{u}	depth-averaged velocity in x -direction
$\langle u \rangle$	ensemble averaged velocity in x -direction
\bar{u}	depth averaged velocity in x -direction
u_b	velocity near the bottom
u_{*b}	friction velocity near the bed
u_f	front speed
u_h	velocity in the harbour
u_i	averaged velocity in x_i -direction
u'_i	fluctuating part of the velocity in x_i -direction
u_n	velocity normal to a surface
u_r	velocity in the river
u_{\parallel}	velocity parallel to a surface
u_*	friction velocity
U	characteristic turbulent velocity scale
U_i	instantaneous velocity in x_i -direction
U_{10}	wind speed at 10 meter above the free surface
$\overline{u'_i u'_j}$	horizontal Reynolds shear stress per unit mass
V	volume

x_i	spatial coordinate (x, y, z for $i=1, 2, 3$)
z_k	level of fixed layers
z_0	roughness height

Greek symbols

δ	threshold parameter
δ_{ij}	Kronecker delta
Δt	time step
Δx_i	grid spacing in x_i -direction
Δz_{kmin}	vertical grid spacing near bottom
ϵ	statistical error
ε	rate of dissipation
ε_{ijk}	permutation symbol
ζ	free surface elevation
η	Kolmogorov microscale
θ	bottom slope, time-integration parameter
κ	Von Kármán constant
ν	kinematic viscosity
ν_t	eddy viscosity
ν_t^v	vertical eddy viscosity
ν_t^h	horizontal eddy viscosity
ν_t^{2D}	eddy viscosity related to quasi-2D turbulence
ρ	density, autocorrelation function
ρ_{air}	density air
ρ_0	reference density
σ	transformed vertical coordinate
σ_{ij}	mean deviatoric stress tensor
σ_t	Prandtl/Schmidt number
τ	time, time shift
τ_b	bottom shear stress
τ_w	wind shear stress
τ_{ij}	stress tensor
ϕ	geographic latitude
Ψ	limiter function
ω	vertical transformed velocity
Ω	planetary vorticity
∇	horizontal gradient
∇_m	filter function

Sub- and superscripts

n	discrete time level
*	intermediate time level, variables along σ -planes
i, j, k, l	discrete coordinates in x, y and z -direction

Dankbetuiging

Het uitvoeren van een promotieonderzoek is een solitaire bezigheid. Toch is het welhaast onmogelijk een dergelijk project tot een goed einde te brengen zonder inbreng van anderen. Enkele personen wil ik met name noemen omdat zij bij het tot stand komen van het proefschrift een belangrijke rol hebben gespeeld.

Allereerst wil ik Jurjen Battjes en Guus Stelling bedanken voor het feit dat zij mij de mogelijkheid hebben geboden dit promotieonderzoek uit te voeren. Voor de financiering van het promotieonderzoek ben ik RWS/RIKZ en de Dr ir Cornelis Lelystichting zeer erkentelijk.

Guus Stelling wil ik tevens bedanken voor zijn begeleiding op momenten dat deze nodig was, de waardevolle suggesties met betrekking tot de ontwikkelde numerieke modellen maar vooral ook voor de talrijke anekdotes waarvan hij mij de afgelopen jaren deelgenoot heeft gemaakt. Cees Kranenburg heeft als dagelijks begeleider in de eerste jaren veel ideeën aangedragen en met opbouwende kritiek mij wegwijs gemaakt in het wetenschappelijk onderzoek. Julie Pietrzak's commentaar en suggesties met betrekking tot de inhoud en de structuur van het proefschrift hebben in hoge mate bijgedragen aan de leesbaarheid en de kwaliteit van het proefschrift. Veel dank hiervoor. Dank aan Jurjen Battjes voor het kritische commentaar op het manuscript van het proefschrift.

De discussies met collega's van zowel het Laboratorium van Vloeistofmechanica van de Faculteit der Civiele Techniek van de Technische Universiteit Delft als van het Waterloopkundig Laboratorium zijn voor mij zeer waardevol geweest. Bedankt voor het delen van jullie kennis met mij en voor de getoonde interesse en betrokkenheid. Naast de inhoudelijke kant dient de prima werksfeer in het Laboratorium van Vloeistofmechanica niet onvermeld te blijven.

Verder wil ik de leden van de gebruikerscommissie bedanken voor hun commentaar en suggesties.

Als laatste wil ik diegene in mijn persoonlijke omgeving bedanken die mij gedurende de afgelopen jaren onophoudelijk hebben gesteund en onvoorwaardelijk begrip en geduld hebben opgebracht.

Curriculum Vitae

Marco Bijvelds werd op 27 oktober 1971 geboren te Eindhoven. Het voorbereidend wetenschappelijk onderwijs werd van 1984 tot 1990 doorlopen aan het Norbertuscollege te Roosendaal. Na het behalen van het Atheneum-diploma begon hij in datzelfde jaar met de studie Civiele Techniek aan de Technische Universiteit Delft. Onder leiding van prof. dr ir G.S. Stelling werd deze studie in 1995 afgerond middels een afstudeerstage bij het Waterloopkundig Laboratorium. Hierbij stond de numerieke modellering van gestratificeerde niet-hydrostatische stromingen centraal.

In de periode tussen 1996 tot 2000 heeft hij bij de sectie Vloeistofmechanica van de Faculteit der Civiele Techniek van de Technische Universiteit Delft onderzoek verricht naar de driedimensionale numerieke modellering van gelaagde stromingen in kustgebieden. De resultaten van dit onderzoek zijn in dit proefschrift beschreven.

Daarnaast is hij sinds 1998 als projectingenieur werkzaam bij het Waterloopkundig Laboratorium. Sinds oktober 2000 heeft hij bij het Waterloopkundig Laboratorium in de hoedanigheid van onderzoeker/adviseur een voltijdbetrekking.

